

**Measurement of  $d\sigma/dy$  for Drell-Yan  $e^+e^-$  Pairs in the  $Z$   
Boson Region Produced in  $p\bar{p}$  Collisions at  $\sqrt{s} = 1.8$  TeV**

by

Jinbo Liu

Submitted in Partial Fulfillment

of the

Requirements for the Degree

Doctor of Philosophy

Supervised by

Professor Arie Bodek

Department of Physics and Astronomy

The College

Arts and Sciences

University of Rochester

Rochester, New York

2000

# Acknowledgements

First, I would like to thank all CDF collaborators and Fermilab staffs who each did his/her share in making CDF an excellent experiment. I learned a great deal from these people. Their enthusiasm in high energy physics and their determination for excellence have been the constant inspiration for me.

I would like to thank my advisor, Arie Bodek, for introducing me to the field and providing me constant support throughout all these years. I thank Willis Sakumoto and Howard Budd for many valuable discussions and advice, which were almost daily. This analysis would not have been possible without them. I also thank Howard, Arie and Willis for the patience they had teaching me how to write in English with less mistakes. I thank Yeon Sei Chung for helping me go through 500 8mm tapes for Run 1A data. He made the task much less painful than it sounds.

I thank Andrew Gordon, Qun Fan, and Doug Glenzinski for making and taking care of the Run 1B datasets.

I would like to thank Qun Fan, Mark Lancaster, Larry Nodulman, Steve Kuhlmann, Bob Wagner (Argonne Lab), Mark Kruse, Daniel Cronin-Hennessy, Adam Hardman and James Done for the generous helps in making this analysis a less bumpy ride. I especially thank Mark Lancaster, Larry Nodulman and Steve Kuhlmann for being great godparents for my paper. I would like to thank the computer staffs at CDF and Feynmann center for their endless effort in making the computing easy and reliable.

I would like to thank all members of CDF Run II Plug Upgrade group, especially Michael Albrow, Giorgio Apollinari, Pawel de Barbaro, Arie Bodek, Howard Budd, Yasuo Fukui, Alvin Laasanen, Mike Lindgren, and Willis Sakumoto, for making

my service work at CDF a nice and valuable experience.

I would like to thank the department secretaries, Mrs. Barbara Warren, Mrs. Connie Jones, Mrs. Sue Brightman and Mrs. Judy Mack who have been taking such good care of me the minutes I set my feet in US.

I thank Lucy and Pawel De Barbaro for being such great hosts to those nice dinners.

I thank my best friend and classmate Sergei Avvakumov for sharing laughs with me when we were watching Seinfeld together.

I thank my friends Randy Leiter, Barbara Asman, Ricardo Barbosa, and Ricardo Eusebi for those wonderful time we spent together during the last year of my graduate student life.

I would like to thank my wonderful family who stood by me and encouraged me in both good and bad times. Thanks my grandmothers for the love and blessing you give me. Thanks Mom and Dad for your love, support, and understanding. Thanks my dear brother for not only caring about me but also giving me advice and encouragement as a good friend.

Finally, couple of words to those raccoons hanging outside the CDF trailer offices. Although several times you scared me to death when I ran into you late at night after work, I think I will still miss you as part of my graduate student life.

## Abstract

We report on the first measurement of the rapidity distribution,  $d\sigma/dy$ , over the full kinematic range for  $e^+e^-$  pairs in the  $Z$  boson region of  $66 < M_{ee} < 116 \text{ GeV}/c^2$ . The data sample consists of  $108 \text{ pb}^{-1}$  of  $p\bar{p}$  collisions at  $\sqrt{s} = 1.8 \text{ TeV}$  taken by the Collider Detector at Fermilab during 1992–1995. The total cross section in the  $Z$ -boson region is measured to be  $252 \pm 11 \text{ pb}$ . The total cross section and  $d\sigma/dy$  are compared with Quantum Chromodynamics calculations in leading order, next-to-leading-order (NLO), next-to-next-leading-order, and NLO with gluon resummation.

# Contents

<b>1</b>	<b>Introduction</b>	<b>1</b>
1.1	The Standard Model . . . . .	2
1.2	Proton Antiproton Collisions . . . . .	5
1.2.1	Parton distribution functions . . . . .	7
1.2.2	Kinematics: rapidity . . . . .	9
1.3	$\gamma^*/Z$ Production and Decay at a $p\bar{p}$ Collider . . . . .	12
1.4	Overview of the Analysis . . . . .	15
<b>2</b>	<b>The Experiment</b>	<b>17</b>
2.1	The Fermilab Tevatron . . . . .	17
2.2	The Collider Detector at Fermilab . . . . .	19
2.2.1	Overview of the Detector . . . . .	20
2.2.2	Tracking . . . . .	21
2.2.3	Calorimetry . . . . .	26
2.2.4	Beam-Beam Counters . . . . .	30
2.2.5	Trigger Systems . . . . .	31
<b>3</b>	<b>The Data Sample</b>	<b>34</b>
3.1	Event Selection . . . . .	35
3.1.1	Electron Triggers . . . . .	36

3.1.2	Electron Clustering . . . . .	38
3.1.3	Electron Geometric and Kinematic Cuts . . . . .	39
3.1.4	The Event Primary $z$ Vertex Measurement . . . . .	40
3.1.5	CTC, VTX, and SVX Trackings. . . . .	43
3.1.6	Electron Identification Cuts . . . . .	47
3.2	Backgrounds . . . . .	52
3.2.1	Isolation Energy Extrapolation Method . . . . .	54
3.2.2	Background Estimate with SVX Tracking . . . . .	63
3.2.3	Background $y$ Distribution . . . . .	64
3.3	Signal versus Background . . . . .	65
3.4	Event Selection Efficiency . . . . .	65
3.4.1	Trigger Efficiency . . . . .	68
3.4.2	Offline Selection Efficiency . . . . .	76
3.4.3	Primary $z$ Vertex Correction . . . . .	83
3.4.4	Luminosity . . . . .	85
<b>4</b>	<b>Monte Carlo</b>	<b>86</b>
4.1	The Monte Carlo Program . . . . .	86
4.2	Monte Carlo versus Data . . . . .	89
4.3	Acceptance . . . . .	94
<b>5</b>	<b>Systematic Errors</b>	<b>97</b>
5.1	Systematic uncertainty from the background subtraction . . . . .	98
5.2	Systematic uncertainty from the background in the efficiency sample	99
5.3	Systematic error from modeling the $P_T$ distribution of $Z$ bosons . .	100
5.4	Systematic error from the choice of PDFs . . . . .	101
5.5	Systematic error from the energy resolution of the calorimeter . . .	103

<b>6</b>	<b>The Results</b>	<b>104</b>
6.1	The Differential Cross Section, $d\sigma(\gamma^*/Z)/dy$ . . . . .	104
6.2	The Total Cross Section of $\gamma^*/Z$ Production . . . . .	109
<b>7</b>	<b>The Conclusions</b>	<b>115</b>
	<b>Bibliography</b>	<b>116</b>
<b>A</b>	<b>Monte Carlo Programs in Particle Physics</b>	<b>121</b>
<b>B</b>	<b>Parton Distribution Functions</b>	<b>123</b>
<b>C</b>	<b>Rapidity Distribution in High Mass Region</b>	<b>126</b>

# List of Figures

1.1	The elementary particles. . . . .	3
1.2	A hard scattering between two partons in an energetic $p\bar{p}$ collision. . . . .	7
1.3	Parton momentum fractions as a function of the rapidity of the $Z$ boson for $\sqrt{s} = 1800$ GeV. . . . .	11
1.4	The Feynman diagrams for $\gamma^*/Z$ production in a $p\bar{p}$ collision. The lowest order process is shown in (a). Examples of the first order, $O(\alpha_s)$ , diagrams are shown in (b) a gluon exchanges between the annihilating quarks; (c) a gluon emitted in the process of producing a $\gamma^*/Z$ boson; (d) a gluon interacting with a quark or antiquark to form a $\gamma^*/Z$ boson. . . . .	13
1.5	The rapidity cross section ratio, $R(y) = 1/\sigma \times d\sigma/dy$ measured with the Run 1 dimuon data. Only the statistical and non-luminosity related systematic error are included. The measurement is compared to leading order calculations with a K factor. The theoretical curves are calculated using CTEQ3L (dotted line), MRSA (solid line), CTEQ3M (dashed line) and MRSD' (dot-dashed line) PDFs. . . . .	16
2.1	Schematic of the accelerator complex at Fermilab. . . . .	18
2.2	One-quarter of an elevation view of the CDF detector. . . . .	20
2.3	A schematic diagram of one of the two SVX barrels. . . . .	23



2.4	Transverse view of the CTC endplate illustrating the 9 superlayer geometry. . . . .	25
2.5	A lateral view of one quarter of CDF detector. It shows a clear view of the calorimeter subsystems and their segmentation in pseudorapidity. The position and the size of the forward calorimeter are not to scale. . . . .	27
3.1	$e^+e^-$ pair mass distribution for the PP (upper plot) and PF (lower plot) samples. The un-shaded histograms show the $e^+e^-$ pairs before requiring associated VTX tracks for PEM or FEM showers. The shaded histograms show the $e^+e^-$ pairs which fail the VTX tracking requirement (one or both legs). The un-shaded histogram minus the shaded one gives the $e^+e^-$ pairs passing VTX tracking requirement. The small bumps at the $Z$ mass region on the shaded histograms are due to the VTX tracking inefficiency (4% for the PP sample and 5% for the PF sample). . . . .	45
3.2	$e^+e^-$ pair mass distribution for the PP (upper plot) and PF (lower plot) samples. The electrons shown in this figure are all in SVX fiducial region. The un-shaded histograms show the $e^+e^-$ pairs before requiring associated SVX tracks for PEM showers. The shaded histograms show the $e^+e^-$ pairs which fails the SVX tracking requirement (one or both legs). The un-shaded histogram minus the shaded one gives the distribution for $e^+e^-$ pairs passing SVX tracking requirements. The small bumps on the $Z$ mass region in the shaded histograms are due to the SVX tracking inefficiency (12% for the PP sample, and 6% for the PF sample). . . . .	46

3.3	(a) Upper plot: the VT XOCC of the first plug electron vs the VT XOCC of the other plug electron for PP electron pairs. Both plug legs are required to have associated SVX tracks. (b) Lower plot: the VT XOCC of the plug electron vs the VT XOCC of the forward electron for PF electron pairs. The plug legs are required to have SVX tracks. These plots illustrate that the VT X tracking and the SVX tracking are consistent with each other. . . . .	48
3.4	Eiso distributions of the $\gamma^*/Z$ electrons (signals) and QCD backgrounds from central, plug, and forward calorimeters. They are extracted from the clean $\gamma^*/Z$ event samples and background samples. The unit on Eiso is GeV. . . . .	57
3.5	The Run 1A (left two) and 1B Eiso distribution of the central electron for the CP and CF samples. They are fitted using Eq. 3.6. The dashed curves are the background predictions. The integral under the background curves in the Eiso(c) region of 0-4 GeV gives the estimated number of background events in the final CP or CF sample. . . . .	59
3.6	The Run 1A (left two) and Run 1B (right two) Eiso(p) distribution for the CP, PP, and PF samples. The dashed curves are the background predictions from the fit. . . . .	62
3.7	Background shapes as a function of $y$ . It is extracted from background samples. . . . .	66
3.8	The combined Run 1A and 1B raw $y$ distribution for the $e^+e^-$ pair candidates and for the backgrounds (shadow histogram). The dash-dot curve on the background histogram is the sum of the fit curves in Figure 3.7 normalized to the total number of background in Run 1A and 1B. . . . .	67

3.9	Run 1A L2 trigger (PEM_20*) efficiency as a function of $E_t$ assuming that the $z$ vertex is zero. The unit on $E_t$ is GeV. . . . .	71
3.10	Run 1B L2 trigger (PEM_20*) efficiency as a function of $\phi$ (upper plot) and detector Eta (lower plot). . . . .	72
3.11	Run 1B L2 trigger (PEM_20*) efficiency as a function of $E_t$ assuming that the $z$ vertex is zero. The unit on $E_t$ is GeV. . . . .	73
3.12	Invariant mass distribution of “no second track” events for Run 1A (upper plot) and Run 1B (bottom plot) data. . . . .	80
4.1	Run 1A $E_T$ distribution for the CC, CP, CF, PP, and PF event topologies. The crosses are data, and the histograms are the Monte Carlo with event counts normalized to the data. . . . .	90
4.2	Run 1B $E_T$ distribution for the CC, CP, CF, PP, and PF event topologies. The crosses are data, and the histograms are the Monte Carlo with event counts normalized to the data. . . . .	91
4.3	Run 1A $e^+e^-$ pair invariant mass distribution for the CC, CP, CF, PP, and PF event topologies. The last plot (the bottom right) is the mass distribution for events from all $e^+e^-$ pair topologies. The crosses are data, and the histograms are the Monte Carlo with event counts normalized to the data. . . . .	92
4.4	Run 1B $e^+e^-$ pair invariant mass distribution for the CC, CP, CF, PP, and PF eventtopologies. The last plot (the bottom right) is the mass distribution for events from all $e^+e^-$ pair topologies. The crosses are data, and the histograms are the Monte Carlo with event counts normalized to the data. . . . .	93

4.5	Run 1A $\eta_{det}$ , $Z$ rapidity, $\cos(\theta_{CS})$ and $Z$ $P_T$ distributions. The crosses are the data from all $e^+e^-$ pair topologies, and the histograms are the Monte Carlo with the Monte Carlo weighted by the selection efficiencies. The Monte Carlo event counts are normalized to the data. . . . .	95
4.6	Run 1B $\eta_{det}$ , $Z$ rapidity, $\cos(\theta_{CS})$ and $Z$ $P_T$ distributions. The crosses are the data from all $e^+e^-$ pair topologies. The histograms are Monte Carlo events with the Monte Carlo weighted by the selection efficiencies. The Monte Carlo event counts are normalized to the data. . . . .	96
5.1	The relative systematic error on $\epsilon A$ ( $\frac{ \Delta(\epsilon A) }{\epsilon A}$ ) versus $y$ from difference systematic uncertainty sources. Because there are no data above 2.8, the systematic error estimate is given only up to $ y  = 2.8$ . . . . .	102
6.1	Acceptance times efficiency as a function of dilepton rapidity for the various categories of $e^+e^-$ pairs. By including PP and PF events, the measurement is extended in rapidity up to $y$ of 2.8, with a significant increase in statistics in the $ y  > 1.2$ region. . . . .	106
6.2	$d\sigma(\gamma^*/Z)/dy$ distribution of $e^+e^-$ pairs in the mass range $66 < M_{ee} < 116$ GeV/ $c^2$ . The dots are Run 1A and 1B combined data and the curves are the LO(CTEQ3L), LO(CTEQ5L), NLO(MRST99) and NLO(CTEQ5M-1) calculations, respectively. The total cross section of the theory curves are normalized to the data. They are scaled up to compare to the data by factors of 1.55, 1.51, 1.14, and 1.13 for LO(CTEQ3L), LO(CTEQ5L), NLO(MRST99), and NLO(CTEQ5M-1), respectively. . . . .	110

6.3	$d\sigma(\gamma^*/Z)/dy$ distribution of $e^+e^-$ pairs in the mass range $66 < M_{ee} < 116 \text{ GeV}/c^2$ . The dots are Run 1A and 1B combined data and the curves are the NLO(CTEQ4M), VBP(CTEQ4M), and NLO(CTEQ4M-d) calculations, respectively. The total cross section of the theory curves are normalized to the data. They are scaled up to compare to the data by factors of 1.12, 1.09, and 1.10 for NLO(CTEQ4M), VBP(CTEQ4M), and NLO(CTEQ4M-d), respectively . . . . .	111
6.4	Data/Theory of $d\sigma(\gamma^*/Z)/dy$ of $e^+e^-$ pairs in the mass range $66 < M_{ee} < 116 \text{ GeV}/c^2$ . The data are Run 1A and 1B combined. The total cross section of the calculations for LO(CTEQ3L), LO(CTEQ4L), LO(CTEQ5L), NLO(CTEQ4M), VBP(CTEQ4M), NLO(CTEQ4M-d), NLO(CTEQ5M-1), and NLO(MRST99) are scaled up to compare to the data by factors of 1.55, 1.52, 1.51, 1.12, 1.09, 1.10, 1.13, and 1.14, respectively. . . . .	112
B.1	The kinematic map in the $(x,Q)$ plane of data points used in the CTEQ5 analysis. . . . .	124
C.1	$d\sigma(\gamma^*/Z)/dy$ distribution of $e^+e^-$ pairs in the mass range $M_{ee} > 116 \text{ GeV}/c^2$ . The dots are the combined Run 1A and 1B data. The curves are the leading order and next to leading order theoretical predictions using LO(CTEQ5L), NLO(MRST99) and NLO(CTEQ5M-1) PDFs, respectively. The predictions are normalized to the data using the normalization factors from the $Z$ mass region, i.e. 1.51, 1.14, and 1.13 for LO(CTEQ5L), NLO(MRST99), and NLO(CTEQ5M-1) calculations, respectively. . . . .	129

# List of Tables

1.1	Fermions in the Standard Model. . . . .	4
1.2	The four basic forces and their force-carrying particles. The strength are relative to the strong force at a distance of $10^{-13}$ cm. The graviton is not yet observed and gravity is not incorporated into the Standard Model. . . . .	4
2.1	An overview of CDF calorimeter subsystems. The energy resolutions are for incident electrons, positrons or photons (EM calorimeter) and isolated pions (HAD calorimeter). The position are averages for the calorimeter subsystems. Here $X_0$ is radiation lengths (EM calorimeter) and $\lambda_0$ is interaction or attenuation length (HAD calorimeter). . . . .	28
3.1	The geometric and kinematic acceptance for electron candidates . .	40
3.2	Selection cuts for the CC, CP, CF categories. . . . .	49
3.3	Selection criteria for Plug-Plug and Plug-Forward events. . . . .	50
3.4	The parameter values for the Eiso distribution of central electrons. ( $S_c(x) = e^{-S_{c1}x} + S_{c2} \times e^{-S_{c3}x}$ ) . . . . .	56

- 3.5 The parameter values for the Eiso distribution of QCD background in the central region. ( $B_c(x) = e^{-(x/\sigma_B)^2/2}$ ) It is determined using a background dominated sample. . . . . 58
- 3.6 The parameters which define the Eiso distribution of plug electrons ( $S(x) = x^{s^2}e^{-(x/s^3)}$ ) and Eiso distribution of QCD jets in the plug region ( $B(x) = x^{b^2}e^{-(x/b^3)}$ ). 1A(CP,PP,PF) column is for the plug electron from the CP, PP, and PF samples for Run 1A. 1B(CP) column is for the plug electron from the CP sample for Run 1B. The 1B(PP,PF) column is for the plug electron from the PP and PF samples for Run 1B. . . . . 60
- 3.7 The parameters which define the Eiso distribution of forward electron ( $S(x) = x^{s^2}e^{-(x/s^3)}$ ) and Eiso distribution of QCD jets in forward region ( $B(x) = x^{b^2}e^{-(x/b^3)}$ ). 1A+1B(CF) and 1A+1B(PF) columns are for the forward electron from the CF and PF for combined Run 1A and Run 1B, respectively. . . . . 60
- 3.8 The estimated QCD background fractions using different methods. Here, Eiso<sub>1</sub> refers to the Eiso of one leg, and Eiso<sub>2</sub> refers to the other leg. The second column is the estimate using the Eiso(c) distributions for the CP and CF samples, and Eiso(p) for the PP and PF samples. The third column is the estimate using the Eiso(p) distributions for the CP and PP samples, and Eiso(f) for the CF and PF samples. The fourth column is the estimate from the SVX tracking method. The fifth column is the final background estimates using the combined result from the Eiso<sub>1</sub>, Eiso<sub>2</sub> and SVX techniques. 61
- 3.9 Number of events passing all the event selection cuts ( $N^{candidates}$ ) and background estimates ( $N^{background}$ ). The background fraction  $f^{background} = N^{background}/N^{candidates}$ . . . . . 68

3.10	The mean and RMS of the $E_T(newZvtx)/E_T(oldZvtx)$ and energy correction factors for the electrons from various detector regions. . .	75
3.11	The efficiency of the L3 trigger for different $e^+e^-$ pair categories in Run 1A and Run 1B. The 0.5% inefficiency for the Run 1B CF sample originates from the CTC tracking inefficiency at Level 3. . .	76
3.12	The efficiency for central electrons and for the overall CC sample. The number of same-sign and opposite-sign events is given as $N^{os} - N^{ss}$ . The number of no track events ( $N_{notrk}$ ) is estimated from the fit to the invariant mass distribution of the “no second track” events.	81
3.13	Selection efficiencies for plug and forward elections in the CP and CF samples. Here the first two lines are the cut efficiencies of the plug and forward electrons. The last two lines are the dielectron efficiencies of the CP and CF samples. . . . .	82
3.14	The selection criteria for the samples to measure $\epsilon_{pp}( \Delta(z_{vertex}) )$ and $\epsilon_{pf}( \Delta(z_{vertex}) )$ . . . . .	84
3.15	Summary of the selection efficiencies (for plug and forward electrons) in the PP, PF samples. . . . .	84
4.1	The acceptances for the CC, CP, CF, PP, and PF $e^+e^-$ topologies. The uncertainties of the acceptances shown here are only from Monte Carlo sample statistics. . . . .	94
5.1	The quantity (Eiso <sub>1</sub> -Eiso <sub>2</sub> ) is the difference between the $f^{background}$ using one leg's (Eiso <sub>1</sub> ) and the other leg's (Eiso <sub>2</sub> ) values. The quantity (mean(Eiso <sub>1</sub> , Eiso <sub>2</sub> )) is the mean of the values of Eiso <sub>1</sub> and Eiso <sub>2</sub> . The quantity (SVX-PEM-mean(Eiso <sub>1</sub> , Eiso <sub>2</sub> )) is the difference between the $f^{background}$ from (SVX-PEM) method and the Eiso method. . . . .	99



5.2	The resolution parameters used in the Monte Carlo detector simulation. . . . .	103
6.1	$d\sigma/dy$ distribution of $e^+e^-$ pairs in the mass range $66 < M_{ee} < 116$ GeV/ $c^2$ . The $y$ is the bin center value. C is the bin centering correction. $d\sigma/dy$ is the differential cross section from the Run 1A and Run 1B data. The first error on $d\sigma/dy$ is statistical error, and the second is the systematic error except for the 3.9% integrated luminosity error. . . . .	107
6.2	Various theoretical calculations of the total cross section for $66 < M_{\gamma^*/Z} < 116$ GeV/ $c^2$ . The measurement using CDF Run 1 data is 252.1 pb. Note that except for the CTEQ5M-1, MRST99 and MRST99 $\uparrow$ , MRST99 $\downarrow$ , and MRST <sub>NNLO</sub> , the other PDFs have some mistakes in the QCD evolution to the $Z$ mass. . . . .	114
C.1	Number of events passing selection cuts and background estimates.	127
C.2	The acceptances for the CC, CP, CF, PP, and PF $e^+e^-$ topologies in high mass region. The uncertainties shown here only include the Monte Carlo statistical errors. . . . .	128
C.3	$d\sigma/dy$ distribution of $e^+e^-$ pairs in the mass range $M_{ee} > 116$ GeV/ $c^2$ . Here $y$ is the bin center value, and $d\sigma/dy$ is the differential cross section from the combined Run 1A and Run 1B data. The errors shown for $d\sigma/dy$ include statistical errors only. . . . .	128

# Chapter 1

## Introduction

Elementary particle physics deals with questions first recorded by the philosophers in ancient Greece. What is the basic nature of the material world around us? What are the simplest, the most elementary kinds of matter? What are the basic forces that operate in our material world? Although these are very old questions, it was not until about a century ago that scientists began to make progress in trying to answer them. \* Currently, the theoretical framework that describes the fundamental constituents of matter, which we call the elementary particles, and the basic forces that govern their behavior is a relativistic quantum field theory called the *Standard Model*. The predictions made by the theory are in excellent agreement with experimental measurements. In some cases the theory has been tested to a precision of better than .1%.

---

\*I define the birthday of elementary particle physics to be 1897, when J.J. Thomson discovered the electron [1].

## 1.1 The Standard Model

According to the Standard Model, there are three types of fundamental particles that interact via the four basic forces. The Standard Model successfully describes three of the four forces of nature: the electromagnetic, the weak, and the strong.<sup>†</sup> The fundamental particles are the quarks, leptons, and the force-carrying particles (gauge bosons). All matter is constructed from leptons and quarks, which interact via the exchange of gauge bosons. Figure 1.1 shows a chart of the fundamental particles. The quarks and leptons are classified in three generations (or families), shown as the three columns in Figure 1.1. For each of the particles shown in Figure 1.1, there exists an anti-particle with the same mass and spin, but with opposite values for other properties, such as electric charge.

The leptons and quarks are both spin 1/2 fermions which must obey Fermi-Dirac statistics.<sup>‡</sup> There are six types (or *flavors*) of leptons. Three of them are the electron ( $e$ ), muon ( $\mu$ ), and tau ( $\tau$ ). These leptons carry electric charge of -1 and vary in mass. The other three leptons are the electron neutrino ( $\nu_e$ ), muon neutrino ( $\nu_\mu$ ), and tau neutrino ( $\nu_\tau$ ). These leptons are electrically neutral and have very low mass. The six leptons are paired into three generations. Each generation consists of a charged lepton and a neutrino. Table 1.1 lists leptons grouped in generations.

There are six distinct flavors of quarks. They are the up (u), down (d), charm(c), strange(s), top(t) and bottom(b). They differ in mass and carry electric charge equal to a precise fraction of an electron's charge: the d, s, and b quarks have a charge of -1/3, and the u, c, and t quarks have a charge of +2/3. Table 1.1 lists the quarks grouped in generations. Besides electric charge, each quark has an

---

<sup>†</sup>The fourth basic force, *gravity*, is not incorporated into the Standard Model.

<sup>‡</sup>Fermi-Dirac statistics requires that no two particles within a given system are in the same state, i.e. energy and quantum numbers.

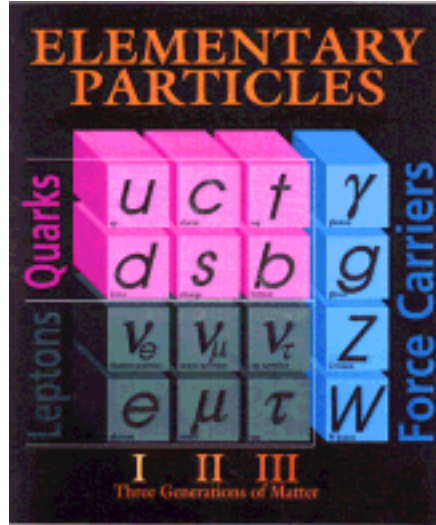


Figure 1.1: The elementary particles.

additional degree of freedom called color. It is labelled as Red(R), Green (G), or Blue(B), and plays the same role in strong interactions as the electric charge does in electromagnetic interactions.

The forces between particles are mediated by the gauge bosons which are the remaining group of fundamental particles. They all have spin 1 and obey Bose-Einstein statistics.<sup>§</sup> Table 1.2 lists the four forces and their mediators. The photon ( $\gamma$ ) mediates the electromagnetic force, and the  $W^+$ ,  $W^-$  and electrically neutral  $Z$  bosons mediate the weak force. The strong force between quarks is transmitted by eight massless bosons called gluons ( $g$ ). The gluon also carries color charge

---

<sup>§</sup>Bosons can be brought together without restriction,i.e. they can occupy the same state.

Generation	Leptons spin=1/2			Quarks spin=1/2		
	Flavors	Charge ( $ e $ )	Mass (MeV/c <sup>2</sup> )	Flavors	Charge ( $ e $ )	Mass (MeV/c <sup>2</sup> )
1	$\nu_e$	0	$< 10^{-3}$	$u$	+2/3	3
	$e$	-1	0.511	$d$	-1/3	6
2	$\nu_\mu$	0	$< 0.17$	$c$	+2/3	1300
	$\mu$	-1	106	$s$	-1/3	100
3	$\nu_\tau$	0	$< 18.2$	$t$	+2/3	173800
	$\tau$	-1	1777	$b$	-1/3	4300

Table 1.1: Fermions in the Standard Model.

Type of Force	Gravity	Electromagnetic	Weak	Strong
Mediated by	Graviton	Photon( $\gamma$ )	$W^\pm, Z$	gluon(g)
Mass (GeV/c <sup>2</sup> )	0	0	$W^\pm = 80.4$ $Z = 91.2$	0
Act on	all	electrically charged	leptons, quarks	quarks
Strength	$10^{-38}$	$10^{-2}$	$10^{-13}$	1
Range	$\infty$	$\infty$	$< 10^{-16}$ cm	$< 10^{-13}$ cm

Table 1.2: The four basic forces and their force-carrying particles. The strength are relative to the strong force at a distance of  $10^{-13}$  cm. The graviton is not yet observed and gravity is not incorporated into the Standard Model.

which is a combination of a color and an anti-color charge. Therefore, the gluons can undergo self-interactions.

All matter around us is built from the first generation of leptons and quarks, i.e. the  $e$ ,  $\nu_e$  and the  $u$  and  $d$  quarks. The protons and neutrons of the atomic nuclei are built from  $u$  and  $d$  quarks, and the atoms are built from a proton or a nucleus surrounded by electrons. The neutrinos interact very weakly and have very little effect in daily life, but they are important in, e.g. nuclear processes where they are needed to explain nuclear beta decays. The other two generations

of particles are not as important in everyday life since all, except the neutrinos, decay very quickly. However, these two generations are very important in particle physics experiments when the Standard Model is tested. So far, all elementary particles have been confirmed experimentally. ¶

The Standard Model consists of the theory of *Quantum Electrodynamics (QED)*, the theory of *Quantum Chromodynamics (QCD)*, and *Electroweak theory*. QED describes the photon-mediated electromagnetic interaction of electrically charged particles. QCD describes the strong interaction of quarks and gluons. Electroweak theory is the unification of the electromagnetic and weak interactions by Sheldon Glashow, Steven Weinberg, and Abdus Salam in the late 1960's [2, 3, 4]. A prediction of Electroweak theory is that the massive particles acquire their masses through interactions with the hypothetical Higgs particle [5], which has not been discovered yet.

Experimental observations are essential in physics. The most common experiments performed in particle physics are collisions of high energy particles. The typical interactions of interest take place within a dimension of  $10^{-15}$  m. Because the spatial resolution is inversely proportional to the momentum transfer in the interaction, therefore to resolve small structures, high energies are needed and for this reason particle physics is also called *high energy physics*.

## 1.2 Proton Antiproton Collisions

Proton antiproton ( $p\bar{p}$ ) collisions are complicated by the fact that the proton and antiproton are not fundamental particles. The internal structure of the proton was discovered in a classical experiment [6] at the Stanford Linear Accelerator Center

---

¶An experiment called Direct Observation of NU Tau - DONUT at Fermilab announced the first direct evidence for the  $\nu_\tau$  on July 21, 2000.

(SLAC) in California. In this experiment, high energy electrons were scattered off protons in a liquid hydrogen target. The cross section was discovered to be larger than what would be expected if the proton was a point-like elementary particle. The proper theoretical interpretation is the following: The proton consists mainly of three quarks,  $uud$ , called *valence* quarks. The antiproton consists mainly of three corresponding antiquarks,  $\bar{u}\bar{u}\bar{d}$ . In addition, there are also gluons and *sea* quarks inside protons and antiprotons. The valence quarks can radiate gluons in a manner similar to the bremsstrahlung process in QED. The gluons are the bosons exchanged to provide the forces that hold the quarks together. They can split into virtual  $q\bar{q}$  pairs, which themselves can radiate other gluons, resulting in a sea of quarks and gluons. Collectively, the quarks and gluons which comprise the proton are called *partons*. One can approximately write

$$p = \overbrace{\underbrace{uud}_{valence} + \underbrace{u\bar{u} + d\bar{d} + \dots}_{sea} + \underbrace{g + g + \dots}_{gluons}}^{partons}$$

This picture of the proton is called the **parton model**.

When a proton collides with an antiproton at high enough energy, the interaction is between the partons in the proton and antiproton.

In most cases, the partons are involved in low energy interactions. In some cases, the partons interact with large momentum transfer, or they annihilate each other. The annihilation creates a burst of energy that can materialize as new particles. The final state consists of fermions and bosons. If quarks or gluons are in the final state, they fragment into a large number of hadrons which are observed experimentally as jets. The direction of a jet is expected to be approximately collinear with the parton that initiated it. If a  $W$  or  $Z$  boson is in the final state, it decays into leptons or into quarks which then fragment. Figure 1.2 shows a hard scattering between two partons in a  $p\bar{p}$  collision.

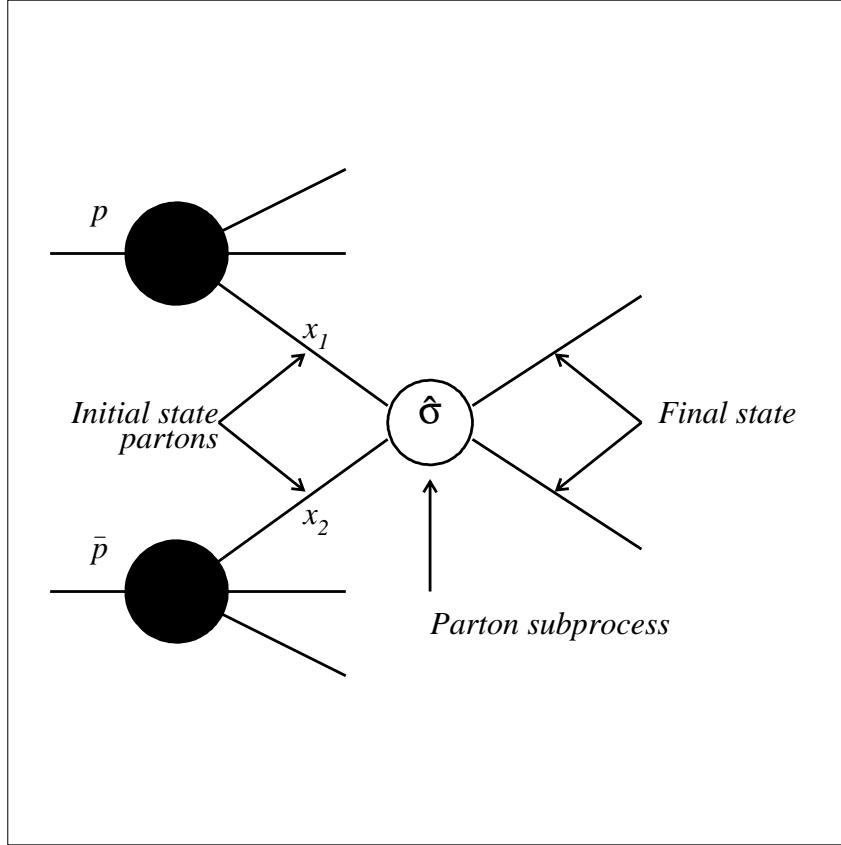


Figure 1.2: A hard scattering between two partons in an energetic  $p\bar{p}$  collision.

### 1.2.1 Parton distribution functions

Hadronic collisions which involve a hard scattering subprocess with high momentum transfer ( $Q^2$ ) can be described by the parton model. Since the fundamental hard interactions involve quarks and gluons, the theoretical description necessarily involves a description of how the partons are distributed in a hadron.



Physicists use parton distribution functions, PDFs, to calculate the cross section of physical processes which have hadrons in the initial state. The PDFs give the density distribution of quarks and gluons as a function of the fraction of the proton's momentum it carries. If the proton (or antiproton) has momentum  $P$  and the parton of interest has momentum  $p$ , we define  $x = p/P$  as the momentum fraction of the parton. The parton distribution is presented as function of  $x$  and  $Q$ , ie.  $f_{a/A}(x, Q^2)$ ; and is customarily interpreted as the probability density for finding a parton  $a$  within a hadron  $A$ , with its momentum fraction between  $x$  and  $x + dx$ , when probed by the momentum transfer  $Q^2$ . The  $Q^2$ -dependence is very successfully described by the DGLAP equations [7] in perturbative QCD. Given the input distributions in  $x$  at a scale  $Q_o^2$  large enough for perturbative QCD to be applicable, one can calculate the distributions at any higher  $Q^2$ .

With the knowledge of PDFs, we can calculate the cross section as:

$$\sigma_{total}(AB \rightarrow C) = \sum_{ij} \int dx_i \int dx_j f(x_j, Q^2) f(x_i, Q^2) \hat{\sigma}(ij \rightarrow C) \quad (1.1)$$

Here  $i$  and  $j$  represent partons. The cross section,  $\hat{\sigma}(ij \rightarrow C)$ , represents the cross section for parton  $i$  with momentum fraction  $x_i$  and parton  $j$  with momentum fraction  $x_j$  to interact and form  $C$ . The sum runs over all possible partons.

The structure of hadrons represented by PDFs is an essential part of our knowledge of the elementary particle world. The interpretation of experimental data in terms of the Standard Model, the precision measurements of Standard Model parameters (for example  $W$  mass), as well as the direct search for signals for physics beyond the Standard Model, all rely heavily on QCD calculations with the PDFs as essential input.

Typically, PDFs are extracted from *deep inelastic scattering* (DIS) data collected at experiments where leptons are scattered on a target containing the par-

ticle to be examined. By measuring the energy and angular distributions of the scattered lepton, the unknown structure of the target particle can be determined. Drell-Yan (DY) [8] lepton pair production at large transverse momenta in  $p\bar{p}$  collisions provide important complementary information on parton distributions. Since any particular experiment covers a limited range of  $x - Q^2$  space, fixed by the center of mass energy, measurements from different experiments are combined into “global QCD fits” that attempts to extract the distributions for all parton species in a particular hadron. The fits are updated as new experimental data becomes available. This continuing effort results in increasing accuracy of the PDFs. Currently, two main groups perform global fits to world data: CTEQ<sup>||</sup> and MRS<sup>\*\*</sup>. In this measurement, we describes a study of PDFs using Drell-Yan dielectrons from  $\gamma^*/Z$  decays in  $p\bar{p}$  collisions at the Tevatron Collider. The measurements are compared to recent PDFs from both the CTEQ and MRS groups.

### 1.2.2 Kinematics: rapidity

In describing  $p\bar{p}$  collisions, it is useful to employ the kinematic variable, *rapidity* ( $y$ ). In the  $p\bar{p}$  center of mass (c.m.) frame with the  $z$  axis along the beam direction, the momenta of the two hadron are equal in magnitudes but opposite in direction. At the parton level, the two partons  $a$  and  $b$  each carry some share of the parent hadron’s momentum. Because these fractions are not necessary equal in magnitudes, the c.m. frame of the two partons is normally not the c.m. frame of the two hadrons. Thus we need to boost along the  $z$  axis in order to get to the c.m. frame of the parton-parton interaction. For this reason, it is useful to use a variable that transforms simply under boosts.

---

<sup>||</sup>CTEQ stands for the Coordinated Theoretical Experimental project on QCD

<sup>\*\*</sup>A.D.Martin, R.G.Robers, W.J.Stirling, and R.S. Thorne.

The rapidity is defined as

$$y \equiv \frac{1}{2} \ln \left( \frac{E + P_z}{E - P_z} \right) \quad (1.2)$$

where  $E$  is the energy of the particle and  $P_z$  is its momentum along  $z$  axis (the proton beam direction). Under a boost in the  $z$  direction to a frame with velocity  $\beta$ ,  $y \rightarrow y - \tanh^{-1} \beta$ . Hence the shape of the rapidity distribution is invariant.

In leading order, the momentum fraction  $x_1$  ( $x_2$ ) carried by the partons from the proton (antiproton) is related to the rapidity ( $y$ ) of the  $Z$  boson via the equation:

$$x_{1,2} = \frac{M_Z}{\sqrt{s}} e^{\pm y} \quad (1.3)$$

where  $s$  is the center of mass energy and  $M_Z$  is the mass of  $Z$  boson. Figure 1.3 shows  $x_1$  ( $x_2$ ) as a function of  $y$ . As can be seen in the plot, at larger rapidity, one of the incoming partons is forced to smaller  $x$ . This means that the  $Z$  rapidity distribution at large rapidity probes the quark distributions at small  $x$  and at large  $x$ . For an example, a  $Z$  boson ( $M_Z=92$  GeV) produced at rapidity  $y = 2.8$  corresponds to the annihilation of quarks with  $x_1 = 0.841$  and  $x_2 = 0.003$ , probed at  $Q^2 = M_Z^2 = 8464$  GeV<sup>2</sup>. Notice that quarks with these  $x$  values are already “measured” in DIS at HERA and in fixed-target experiments respectively, but at much lower  $Q^2$  (about 10–100 GeV<sup>2</sup>).

The parton distributions in the small  $x$  region,  $x < 0.1$ , are of considerable importance both theoretically and phenomenologically. First, the predictions of the rates of various processes which occur at the high energy hadron colliders depend on the precise knowledge of parton densities at small  $x$ . Also, one of the most important predictions of perturbative QCD is that as  $Q^2 \rightarrow \infty$ , the gluon and sea distributions peak more and more near  $x$  of 0.

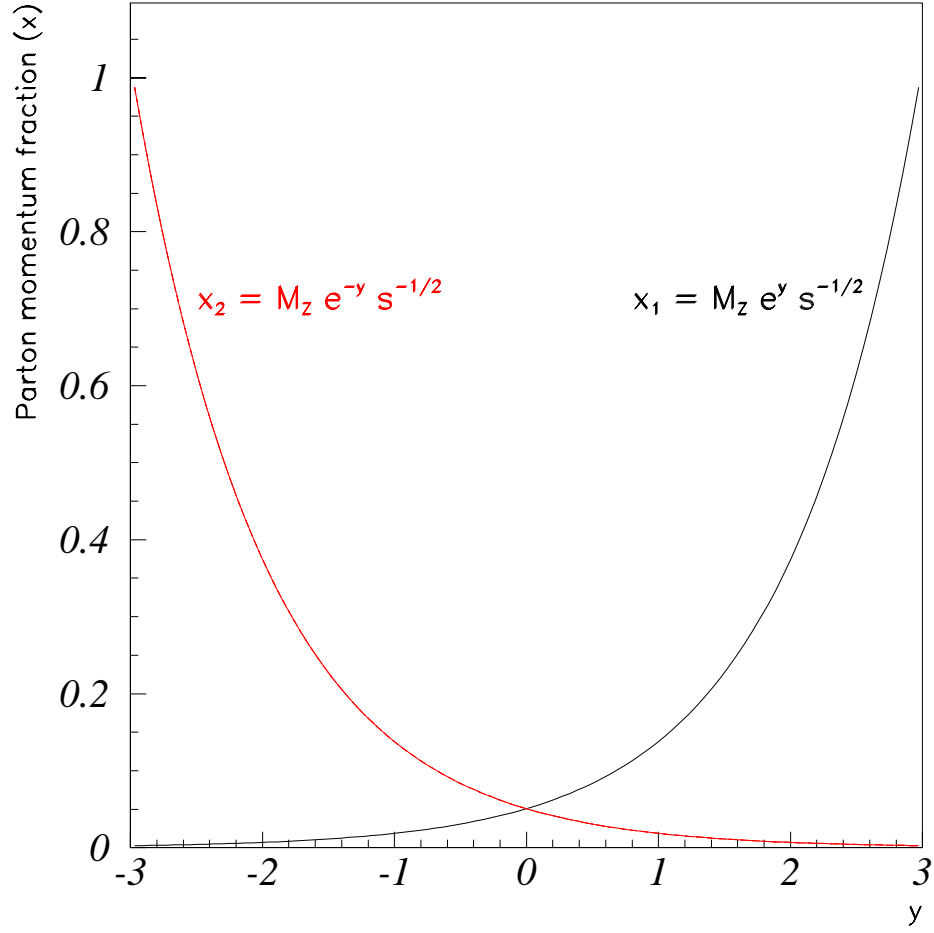


Figure 1.3: Parton momentum fractions as a function of the rapidity of the  $Z$  boson for  $\sqrt{s} = 1800$  GeV.

### 1.3 $\gamma^*/Z$ Production and Decay at a $p\bar{p}$ Collider

According to the electroweak theory, intermediate vector bosons are created in  $p\bar{p}$  collisions when a parton from the proton interacts with a parton from the antiproton. Figure 1.4(a) shows the lowest order Feynman diagram for  $\gamma^*/Z$  boson production in a  $p\bar{p}$  collision. In lowest order, the process is

$$q + \bar{q} \rightarrow \gamma^*/Z. \quad (1.4)$$

This process is from the picture of the naive parton model: a quark from the  $p$  annihilates with the anti-quark from the  $\bar{p}$  to form a virtual  $\gamma^*$  or  $Z$  boson. Two quarks, carrying momentum fractions  $x_1$  and  $x_2$ , participate in the interaction. The intermediate vector bosons  $\gamma^*/Z$  are not stable, they decay to form a variety of other particles, mainly quark-antiquark pairs and lepton-lepton pairs. In this analysis, we study  $\gamma^*/Z$  using its dielectron decay channel.

Figures 1.4 (b), (c) and (d) show  $O(\alpha_s)$  order contributions to the hard scattering cross section: (b) a gluon interacts with both of the annihilating quarks; (c) a gluon is emitted in the process of making the  $\gamma^*/Z$  boson; (d) a gluon interacts with a quark or antiquark to form the  $\gamma^*/Z$  boson. Figure 1.4 (c) and (d) show two examples in which  $\gamma^*/Z$  boson is produced with non-zero transverse momentum.

The differential DY cross section can be written as

$$\frac{d\sigma}{dy} = \sum_{i,j} \hat{\sigma}(ij \rightarrow \gamma^*/Z) \int_{x_1}^1 dx_i \int_{x_2}^1 dx_j f_{i/P}(x_i, Q^2) f_{j/\bar{P}}(x_j, Q^2) \Delta_{ij}(x_i, x_j, x_1, x_2, Q^2) \quad (1.5)$$

Here  $i$  and  $j$  ( $i, j = q, \bar{q}, g$ ) stand for the incoming partons.  $\hat{\sigma}$  is the pointlike DY cross section which describe the process  $q_1 + \bar{q}_2 \rightarrow \gamma^*/Z \rightarrow l_1 + l_2$ . The PDFs  $f_{i/P}(x_i, Q^2)dx_i$  represents the probability to find parton  $i$  in proton with

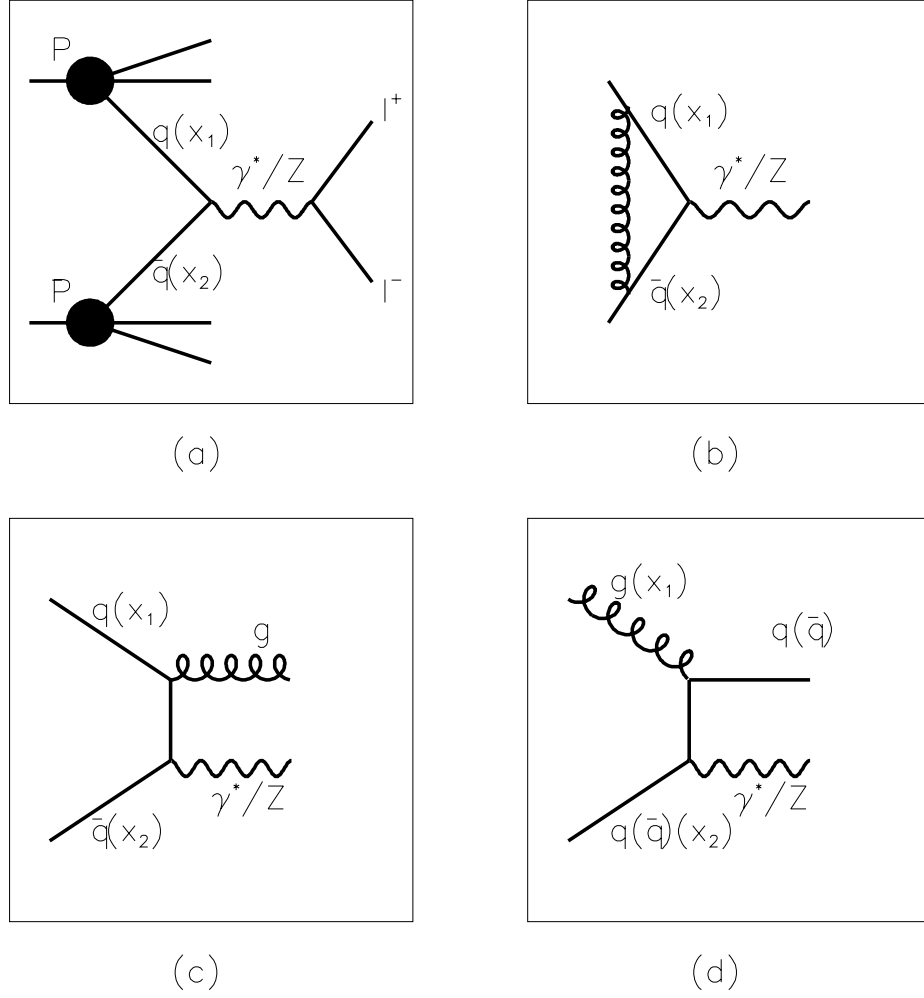


Figure 1.4: The Feynman diagrams for  $\gamma^*/Z$  production in a  $p\bar{p}$  collision. The lowest order process is shown in (a). Examples of the first order,  $O(\alpha_s)$ , diagrams are shown in (b) a gluon exchanges between the annihilating quarks; (c) a gluon emitted in the process of producing a  $\gamma^*/Z$  boson; (d) a gluon interacting with a quark or antiquark to form a  $\gamma^*/Z$  boson.

parton momentum fraction between  $x_i$  and  $x_i + dx_i$ ;  $f_{j/\bar{P}}(x_j, Q^2)dx_j$  represents the probability to find parton  $j$  in antiproton with parton momentum fraction between  $x_j$  and  $x_j + dx_j$ ; Here  $Q^2 = m^2$ , where  $m$  is the lepton pair invariant mass. Finally  $\Delta_{ij}$  denotes the DY coefficient function which is determined by the partonic subprocess  $i + j \rightarrow \gamma^*/Z + X$  where  $X$  represents any multi partonic final state. The coefficient function  $\Delta_{ij}$  can be expanded as a power series in the running coupling constant  $\alpha_s(M^2)$  as follows:

$$\Delta_{ij} = \sum_{n=0}^{\infty} \left( \frac{\alpha_s(M^2)}{4\pi} \right)^n \Delta_{ij}^{(n)} \quad (1.6)$$

The integrations over parton momentum fractions have limits  $x_1$  and  $x_2$ , which are given by Equation 1.3.

In lowest order the coefficient function of the differential cross section in Equation 1.5 is determined by the process shown in Equation 1.4 and is given by

$$\Delta_{q\bar{q}}^{(0)} = \delta(x_i - x_1)\delta(x_j - x_2) \quad (1.7)$$

High order QCD contributions to the differential cross section are the result of quark-gluon interactions. The order  $\alpha_s$  corrections ( $\Delta_{q\bar{q}}^{(1)}$ ) to the process shown in Equation 1.4 are given by the one-loop contributions presented as follows:

$$q + \bar{q} \rightarrow \gamma^*/Z + g \quad (1.8)$$

$$q(\bar{q}) + g \rightarrow \gamma^*/Z + q(\bar{q}). \quad (1.9)$$

The reactions given in Equation 1.8 and 1.9 contribute to  $\Delta_{q\bar{q}}^{(1)}$  and  $\Delta_{gq}^{(1)}$ , respectively. Both contributions  $\Delta_{q\bar{q}}^{(1)}$  and  $\Delta_{gq}^{(1)}$  have been calculated within the DIS-scheme in references [9, 10, 11] and in the  $\overline{MS}$ -scheme in reference [12].

The lifetime of the  $Z$  boson is very short and it decays into quarks or leptons. The decay branching fraction of a  $Z$  into a quark and an antiquark is about 70%. The branching fraction into each lepton pair channel ( $e^+e^-$ ,  $\mu^+\mu^-$ , and  $\tau^+\tau^-$ ) is about 3.4%.

## 1.4 Overview of the Analysis

The  $\gamma^*/Z$  are identified experimentally by its decay products. The rapidity distribution of the  $\gamma^*/Z$  boson has been measured in the  $\mu^+\mu^-$  channel at CDF in a previous analysis [13]. Figure 1.5 shows the measured cross section ratio,  $R(y) = 1/\sigma \times d\sigma/dy$ , as a function of the  $Z$  boson rapidity, compared to theoretical predictions from various PDFs. The disadvantage of the  $\mu^+\mu^-$  channel is the limited coverage of the muon detector at CDF. Therefore, as can be seen in Figure 1.5, the rapidity distribution has been measured up to  $|y| = \pm 1$ . In this measurement, the  $d\sigma/dy$  distribution are measured using  $e^+e^-$  from  $\gamma^*/Z$  decays. This channel has the advantage of high acceptance over the entire kinematic region.

To measure  $d\sigma/dy$ , a sample of  $e^+e^-$  events from the low as well as the high rapidity region of the detector must be identified. Chapter 2 gives a brief description of the apparatus with which the  $e^+e^-$  sample was collected. Chapter 3 describes how the  $e^+e^-$  events from  $\gamma^*/Z$  decays are identified. It includes a study of the event identification efficiencies. In addition, potential sources of background and methods of estimating backgrounds in the  $e^+e^-$  sample are discussed. The background events refers to real electrons from sources other than  $\gamma^*/Z$  decays or jets which mimic electron signals. They need to be subtracted from the selected  $\gamma^*/Z$  candidate events. Chapter 4 describes the acceptance calculation using a sample of simulated events from a Monte Carlo program. The acceptance together with the selection efficiency are important for the normalization of the



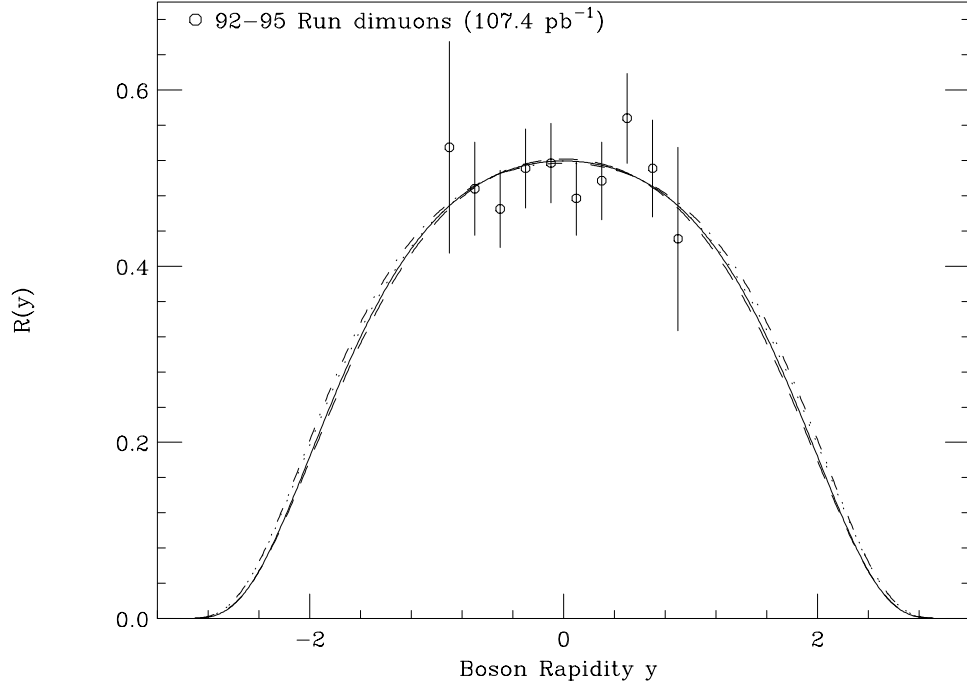


Figure 1.5: The rapidity cross section ratio,  $R(y) = 1/\sigma \times d\sigma/dy$  measured with the Run 1 dimuon data. Only the statistical and non-luminosity related systematic error are included. The measurement is compared to leading order calculations with a K factor. The theoretical curves are calculated using CTEQ3L (dotted line), MRSA (solid line), CTEQ3M (dashed line) and MRSD' (dot-dashed line) PDFs.

$d\sigma/dy$  measurement. Chapter 5 discusses the systematic uncertainty. Chapter 6 gives the measurement results and compares the results with other measurement and theoretical predictions. Chapter 7 presents the conclusions.

## Chapter 2

# The Experiment

Fermi National Accelerator Laboratory (Fermilab) is one of institutions dedicated to the study of elementary particle physics. It is home of a powerful particle accelerator called the Tevatron. In the colliding beam mode, the Tevatron accelerates beams of protons and antiprotons to energies of 900 GeV and collides them at center of mass energy  $\sqrt{s} = 1.8$  TeV within two massive detectors named the Collider Detector at Fermilab (CDF) and DZero (DØ). The data used in this analysis were collected by CDF during the 1992-1995 Tevatron runs (Run 1).

In this Chapter, we describe how the Tevatron works, and the various components of the CDF detector associated with measuring the properties of  $Z$  bosons. Finally, we discuss the CDF trigger system.

## 2.1 The Fermilab Tevatron

Protons and antiprotons are accelerated through five stages to a final energy of 900 GeV. Figure 2.1 shows the schematic of the Tevatron. The beam of particles begins as negative hydrogen ions in the Cockcroft-Walton accelerator. They are

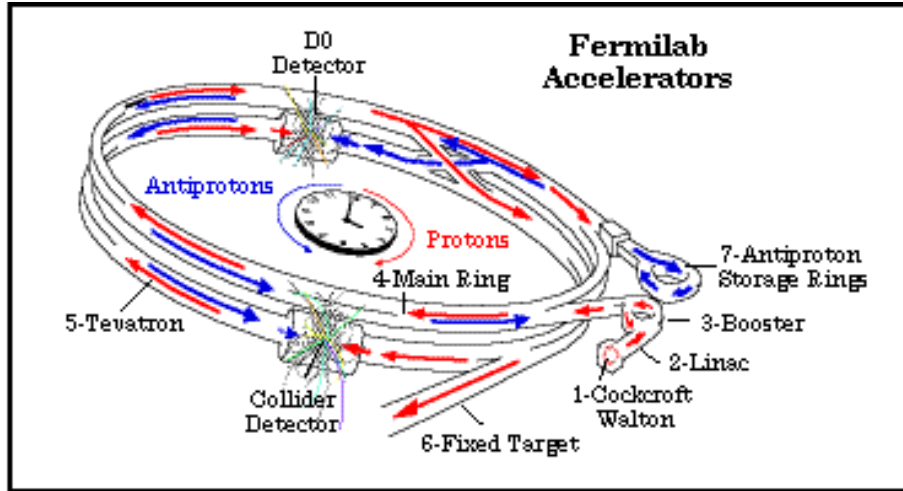


Figure 2.1: Schematic of the accelerator complex at Fermilab.

accelerated to an energy of 750 keV and continue down the 150 meter's long linear accelerator called the Linac. The Linac accelerates the negative hydrogen ions from 750 keV to 400 MeV before injecting them into the Booster accelerator. As the beam of negative hydrogen ions enters the Booster synchrotron, the ions are stripped of their electrons by passing through a carbon foil and become protons. The resulting proton beam is then accelerated to 8 GeV and coalesced into discrete bunches for injection into the next acceleration stage, the Main Ring (the upper ring). During the colliding beam run, the Main Ring synchrotron performs two functions. First, it accelerates proton bunches to 150 GeV for injection into the Tevatron (the lower ring). Second, it provides a source of 120 GeV protons that are used to produce antiprotons.

The 120 GeV protons from the Main Ring are extracted and transported to a target area where the protons collide with a nickel target. The collisions in the target produce a wide range of secondary particles including antiprotons. The antiprotons are focused using a lithium lens and are transported to the Debuncher ring where they are reduced in size by a process known as stochastic cooling. They are then transferred to the Accumulator ring for storage. Finally, when a sufficient number has been produced, the antiprotons are reinjected into the Main Injector and passed down into the Tevatron. The Tevatron is located 65 cm below the Main Ring in the same 1 km radius tunnel. It contains 1,000 superconducting magnets which form a ring directly below the Main Ring magnets and operate in the temperature range of liquid helium (4.6 K). The RF systems of both the Main Ring and the Tevatron operate at 53 MHz. During Run 1, the Tevatron countercirculated six bunches of protons and six bunches of antiprotons with a time between bunch crossing of 3.5 us. The proton and antiproton beams are finally accelerated to 900 GeV inside the same magnetic and RF fields of the Tevatron but in different paths.

When the beams reach 900 GeV, four quadrupole magnets which are installed in the B0 (CDF) and DØ building bring the two beams to collision at the center of the detector. The beam bunches collide inside a vacuum pipe. The apparatus to detect and measure the interactions is assembled around this collision point.

## 2.2 The Collider Detector at Fermilab

The CDF detector [14] is a general purpose detector designed to detect the particles produced in  $p\bar{p}$  collisions, especially high transverse momentum ( $P_T$ ) leptons. It has been discussed in great detail in reference [14]. In this Chapter, we focus on describing the relevant parts of the detector for this measurement.

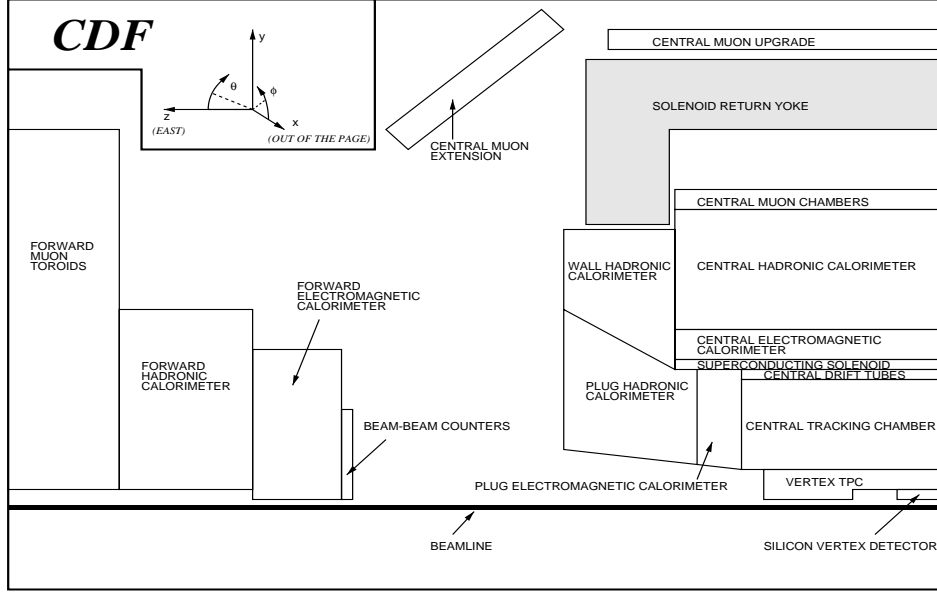


Figure 2.2: One-quarter of an elevation view of the CDF detector.

### 2.2.1 Overview of the Detector

The CDF detector is forward-backward and azimuthally symmetric. It uses a right-handed coordinate system with its origin at the nominal interaction point. Its positive z-axis lies along the beamline in the proton direction (east), the y-axis points vertically upward, and the x-axis points radially outwards in the horizontal plane of the Tevatron (north). Figure 2.2 shows one-quarter of an elevation view of the CDF detector. The azimuthal angle ( $\phi$ ) is measured counterclockwise from the positive x-axis. The polar angle ( $\theta$ ) is measured with respect to the positive z-axis. It is usually given in terms of *pseudorapidity*, which is defined to be:

$$\eta \equiv -\ln[\tan(\theta/2)]. \quad (2.1)$$

For momentum  $p \gg m$ , pseudorapidity is approximately equal to rapidity ( $y$ ) defined in Eq. 1.2.

In the following sections we describe the CDF detector systems which are used in this analysis. These include the tracking systems and the calorimeters.

### 2.2.2 Tracking

A high  $P_T$  particle which is produced at the collision point traverse three separate tracking devices: the Silicon Vertex Detector, the Vertex Time Projection Chambers and the Central Tracking Chamber. They are designed to measure the path of a charged particle as it traverses the detector volume inside the solenoid. The trackers are immersed in a 1.4 Tesla magnetic field which is produced by a superconducting solenoid magnet.

#### The Silicon Vertex Detector

The Silicon Vertex Detector (SVX) is located immediately outside the beam pipe. It provides very high precision tracking information close to the interaction point at the tens of microns level in the x-y plane. Therefore, the SVX is an essential device for secondary vertex detection. In this analysis, the SVX provides electron tracking at high pseudorapidity.

The SVX detector consists of thin silicon wafers implanted with very narrow, closely-spaced conducting strips. It works as follows: When a charged particle passes through the detector, electrons are promoted into the conduction band of the semiconductor material and are drawn to the conducting strips by a high electric field. The strips undergo a voltage drop proportional to the amount of ionization. The strips are then read out by fast electronics.

Because of the radiation doses that the SVX accumulated during the Tevatron 08/1992-05/1993 collider run (Run 1A), the SVX was replaced by a radiation-hardened SVX' for the 01/1994-07/1995 run (Run 1B). The two detectors are similar in design and performance.

The SVX detector consists of two identical barrels placed at both sides of  $z = 0$  along the beamline. There is a 2.15 cm gap between them. Figure 2.3 shows one of the barrels. It is constructed with four concentric radial layers of silicon strip detectors. The inner layer starts at  $r=2.86$  cm from the beam line, and the outer layer is at  $r=7.87$  cm. In  $\phi$  space, each layer of the barrel is divided into 12 sections, known as *ladders*. These ladders are the basic subdivision of the detector. Each ladder consists of three 8.5 cm long,  $300\text{ }\mu\text{m}$  microstrip detectors. The microstrips are electrically bonded to each other along the beamline. The strip pitch is  $60\text{ }\mu\text{m}$  for the inner three layers and  $55\text{ }\mu\text{m}$  for the outer layer. Each ladder is rotated by  $3^\circ$  about its major axis to provide some overlap between adjacent wedges. There are a total of 46,080 channels in the SVX detector.

A typical SVX hit is a cluster of several neighboring strips (usually two or three) and the charge weighted position of the cluster has a position resolution  $\sigma = 10\text{ }\mu\text{m}$ . The single hit efficiency per layer is 96%. The total active length of the detector is 51 cm. Because  $p\bar{p}$  interaction occur with a spread of  $\sigma \approx 30$  cm, the geometrical acceptance of the SVX is about 60%. The SVX covers the pseudorapidity region  $|\eta| < 1.9$  if four hits are required in a SVX track. The coverage extends to  $|\eta| < 2.3$  when three-hit tracks are allowed.

## The Vertex Time Projection Chamber

The main functions of the Vertex Time Projection Chamber (VTX) are to provide precise tracking information for charged particles in the  $r-z$  plane up to a radius of

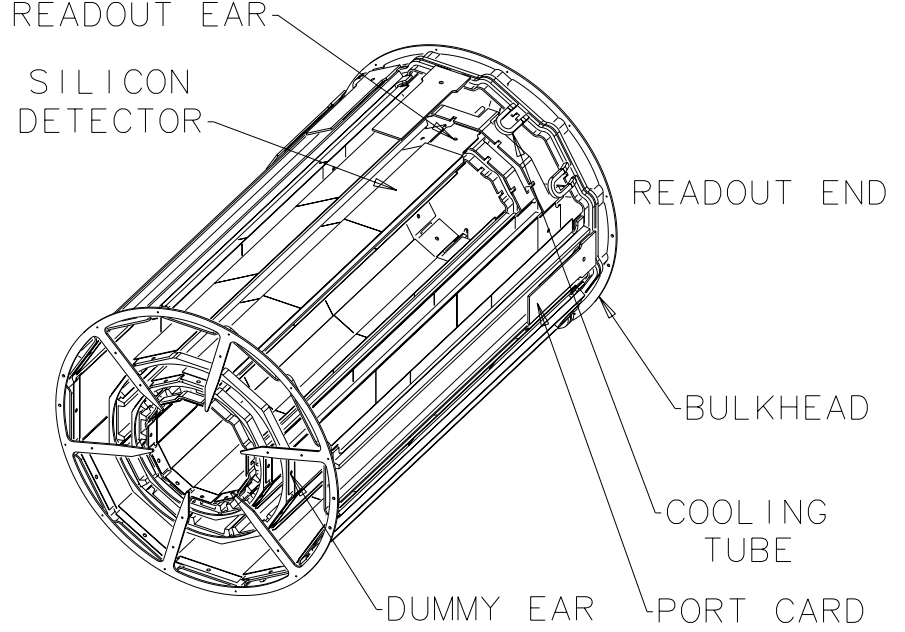


Figure 2.3: A schematic diagram of one of the two SVX barrels.

22 cm and  $|\eta| < 3.25$ , to determine the location along the beamline of the primary interaction vertex, and to distinguish multiple  $p\bar{p}$  interactions in the same beam crossing. In this measurement, it is also an essential tracking device for the high  $\eta$  region.

The VTX is a gas drift chamber that surrounds the SVX. The gas is a 50/50 mixture of argon and ethane with a small amount of isopropyl. The drift velocity is  $46 \mu\text{m/ns}$ . The VTX tracking works as follows: When a charged particle pass through the VTX, it leaves a trail of ionized gas. The freed electrons are accelerated by a large electric field and their collisions with the gas liberate more electrons. The electrons are collected on the sense wires of the chamber. The resulting signal is read out and amplified. The drift time then provides the position of the track in  $z$ .



The VTX consists of a set of drift chambers organized into 8 modules mounted end-to-end along the beamline. Each module is segmented into 8 wedges in  $\phi$ . In each wedge, the wires are perpendicular to the beam line and the radial centerline of the wedges. In order to endow the VTX with some limited  $r - \phi$  tracking information, each module is rotated  $15^\circ$  with respect to the neighboring modules. The radial and  $z$  position of the sense wires combined with the measured drift distance along the  $z$  axis provide track information in the  $r - z$  space. By identifying the tracks of charged particles in the VTX and extrapolating them back to the beam position, we get the  $z$  position of the  $p\bar{p}$  collisions. The resolution along the  $z$  axis is about 2 mm.

### Central Tracking Chamber

The Central Tracking Chamber (CTC) surrounds the VTX and provides full 3-D track reconstruction over the  $|\eta| < 1.1$  region. In this measurement, the 3-D tracking allows us to match the track from a  $Z$  electron with the position of the electron's energy in the electromagnetic calorimeter, hence separating signal from background. The CTC determine the transverse momentum of a charged particle using the curvature of its path in the B field. The CTC also provides the sign of the particle charge using the curvature bend direction.

The CTC is a 3.2 m long cylindrical open cell drift chamber consisting of 84 layers of sense wires. The wires are grouped into nine superlayers, arranged as shown in Figure 2.4. Five of the superlayers have axial wires arranged parallel to the beam line. They are interleaved with four superlayers with stereo sense wires arranged at  $\pm 3^\circ$  to the beamline. A charged particle in the CTC follows a helical trajectory and leaves an ionization trail in the gas. The ionization trail is picked up as hits on the sense wires. The tracks are reconstructed by fitting hits to a

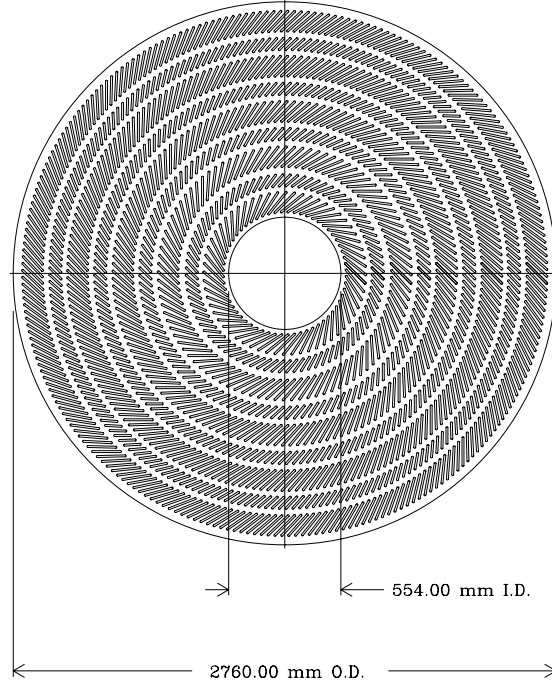


Figure 2.4: Transverse view of the CTC endplate illustrating the 9 superlayer geometry.

helix. The axial layers provide tracking information in the  $r - \phi$  plane only, while the  $3^\circ$  tilt of the stereo layers provides tracking information in the  $r - z$  plane. Together, the axial and stereo layers provide 3-D tracking for charged particles out to a radius of 1.38 m. The resolution using the CTC alone is

$$\delta p_T / p_T \approx 0.002 p_T.$$

It is improved to

$$\delta p_T / p_T \approx 0.001 p_T.$$

when the SVX tracking information is used.

### 2.2.3 Calorimetry

The tracking devices and solenoid are surrounded by calorimeters. A calorimeter is a device that measures the energy of a particle (photon, electron, or hadron) by sampling the energy deposited by the particle in the calorimeter. A calorimeter consists of an electromagnetic (EM) section followed by a hadronic (HAD) section. Each section has two components: absorbing and sampling materials. The absorbing material is typically a heavy metal such as lead or iron which serves to promote electromagnetic cascade (EM section) or nuclear cascade (HAD section). The sampling layers are interleaved with the absorber and are designed to measure the shower activity. In this measurement, the calorimeter measures the energy and position of the electron or positron. It also plays a role in the electron identification by matching the track with EM showers in both position and energy.

In CDF, the calorimeters provide a full coverage in  $\phi$  and a  $\eta$  coverage of  $|\eta| < 4.2$ . The calorimeter system are separated into three regions: central, plug, and forward according to their  $\eta$  coverage. In all, there are seven calorimeter subsystems:

- central calorimeters ( $|\eta| < 1.1$ ):
  - Central Electromagnetic calorimeter (CEM),
  - Central Hadron calorimeter (CHA),
  - Wall Hadron calorimeter. (WHA)
- plug calorimeters ( $1.1 < |\eta| < 2.4$ ):
  - Plug Electromagnetic calorimeter (PEM),
  - Plug Hadron calorimeter. (PHA)
- forward calorimeters ( $2.4 < |\eta| < 4.2$ ):
  - Forward Electromagnetic calorimeter (FEM),

Figure 2.5: A lateral view of one quarter of CDF detector. It shows a clear view of the calorimeter subsystems and their segmentation in pseudorapidity. The position and the size of the forward calorimeter are not to scale.

Forward Hadron calorimeter (FHA).

Each subsystem is segmented in  $|\eta|$  and  $\phi$ , forming a projective tower geometry that points back to the geometric center of the detector. Figure 2.5 shows a lateral view of a quarter of the CDF detector.

The resolution ( $\sigma_E/E$ ) of the calorimeter is usually dominated by sampling fluctuations, and it can be described using

$$\frac{\sigma_E}{E} = \frac{c_1}{\sqrt{E}} \oplus c_2. \quad (2.2)$$

Here  $E$  is in GeV. The first term (stochastic term) comes from the statistical uncertainty in the sampling. The second term is designated as the *constant term*,

System	Coverage ( $ \eta $ )	Segmentation ( $\Delta\eta \times \Delta\phi$ )	Position resolution (cm <sup>2</sup> )	Energy resolution $\frac{\sigma_E}{E}$	Depth
CEM	$< 1.1$	$0.11 \times 15^\circ$	$0.2 \times 0.2$	$13.7\%/\sqrt{E} \oplus 2\%$	$18 X_0$
CHA	$< 0.9$	$0.11 \times 15^\circ$	$10 \times 5$	$50\%/\sqrt{E} \oplus 3\%$	$4.5 \lambda_0$
WHA	$0.7 - 1.3$	$0.11 \times 15^\circ$	$10 \times 5$	$75\%/\sqrt{E} \oplus 4\%$	$4.5 \lambda_0$
PEM	$1.1 - 2.4$	$0.11 \times 5^\circ$	$0.2 \times 0.2$	$22\%/\sqrt{E} \oplus 2\%$	$18 - 21 X_0$
PHA	$1.3 - 2.4$	$0.11 \times 5^\circ$	$2 \times 2$	$106\%/\sqrt{E} \oplus 6\%$	$5.7 \lambda_0$
FEM	$2.2 - 4.2$	$0.11 \times 5^\circ$	$0.2 \times 0.2$	$26\%/\sqrt{E} \oplus 2\%$	$25 X_0$
FHA	$2.4 - 4.2$	$0.11 \times 5^\circ$	$3 \times 3$	$137\%/\sqrt{E} \oplus 3\%$	$7.7 \lambda_0$

Table 2.1: An overview of CDF calorimeter subsystems. The energy resolutions are for incident electrons, positrons or photons (EM calorimeter) and isolated pions (HAD calorimeter). The position are averages for the calorimeter subsystems. Here  $X_0$  is radiation lengths (EM calorimeter) and  $\lambda_0$  is interaction or attenuation length (HAD calorimeter).

i.e. the term in the fractional energy resolution that does not improve with energy. This constant term may result from several causes, for example non-uniformities from cell to cell in the calorimeter, incomplete shower containment, etc. The  $\oplus$  means the second term is added in quadrature to the first term. An overview of the various calorimeter subsystems is given in Table 2.1. Note that the energy resolution for HAD calorimetry is worse than for EM calorimetry. This is due to the fact that the stochastic term results not only from sampling fluctuation but also from nuclei binding energy loss fluctuations. The constant term  $c_2$  results from the same causes as for EM calorimetry plus a new contribution from the unequal response of the calorimeter to electron and hadron showers (e/h).

### Central Calorimeters (CEM, CES, CHA, WHA)

The CEM is composed of lead absorbers interleaved with scintillator layers. The CHA consists of steel plates alternating with scintillator layers. Near the shower

maximum position of the CEM, Central Strip chambers (CES) are embedded to determine the shower position and transverse shower profile. The position resolution for 50 GeV electrons is about 2 mm in both  $r - \phi$  and  $z$  directions. The information from the CES is used for electron identification in the central region. The WHA is constructed with steel absorbers interleaved with scintillators. It covers the gap between central and plug regions. The coverage and resolutions of the central calorimeters are summarized in Table 2.1. The central calorimeters are covered by the CTC. In this measurement, the CTC provides the tracking information (the momentum and charge sign) for the electron candidate in central calorimeters.

### **Plug Calorimeters (PEM, PHA)**

The PEM consists of 34 layers of gas proportional tube arrays interleaved with lead layers. The PHA, located directly behind the PEM, uses 20 layers of proportional tube arrays interleaved with steel layers. It uses the same segmentation as the PEM. The coverage, and resolutions for plug calorimeters are given in Table 2.1. The plug calorimeters are not covered completely by the CTC chamber. However they are covered by the SVX (60%) and the VTX (100%). Therefore, the SVX and VTX provide tracking information for electron candidates in plug calorimeters.

### **Forward Calorimeters (FEM, FHA)**

The FEM is located about 6.5 m from the center of the detector. It is composed of 30 sampling layers of proportional tube chambers interleaved with lead absorber plates. The FHA, has 27 sampling layers of proportional tube chambers alternating with steel absorber plate. The overview of the FEM and FHA is given in Table 2.1. The forward calorimeters are covered only by the VTX.

### 2.2.4 Beam-Beam Counters

The Beam-Beam Counters (BBC) serve as the primary luminosity monitor for CDF. The BBC consists of two sets of scintillation counters mounted on the front of the forward calorimeters, covering the range  $3.24 < |\eta| < 5.90$  ( $0.32^\circ < \theta < 4.47^\circ$ ) at a distance of 5.8 m from the center of the detector. Coincident hits in the east and west BBC counters serve as the minimum bias trigger which indicates that an inelastic collision has occurred. The BBC hits are used to calculate the instantaneous luminosity <sup>\*</sup> at CDF. The instantaneous luminosity is then integrated over time to obtain the total delivered luminosity to the CDF detector. The integrated luminosity  $\mathcal{L}$  is the number to which all other physics processes at CDF are normalized. The followings are the best and typical instantaneous luminosity along with the integrated luminosities for Run 1A and 1B period at CDF.

- Run 1A

The highest instantaneous luminosity was  $0.92 \times 10^{31} \text{ cm}^{-2} \text{ s}^{-1}$ .

A typical instantaneous luminosity was  $0.54 \times 10^{31} \text{ cm}^{-2} \text{ s}^{-1}$ .

Total integrated luminosity of  $19.65 \text{ pb}^{-1}$ . <sup>†</sup>

- Run 1B

The highest instantaneous luminosity was  $2.8 \times 10^{31} \text{ cm}^{-2} \text{ s}^{-1}$ .

A typical instantaneous luminosity was  $1.6 \times 10^{31} \text{ cm}^{-2} \text{ s}^{-1}$ .

Total integrated luminosity was  $90.35 \text{ pb}^{-1}$

---

<sup>\*</sup>The instantaneous luminosity is defined as the number of high energy particles per square centimeter per second passing through the cross section of the interaction region ( $\text{cm}^{-2} \text{ s}^{-1}$ ).

<sup>†</sup>1 pb =  $10^{-36} \text{ cm}^2$

### 2.2.5 Trigger Systems

At the Tevatron, bunch crossing happen at a rate of every  $3.5 \mu\text{s}$ . This corresponds to an event rate of 286 kHz. With a  $p\bar{p}$  total inelastic cross section of 51 mb [15] at  $\sqrt{s} = 1.8 \text{ TeV}$  and a Run 1 instantaneous luminosity of  $10^{31} \text{ cm}^{-2} \text{ s}^{-1}$ , the total inelastic interaction rate is about 0.5 MHz. This is about 1.4 interactions every bunch crossing. This means that the CDF data acquisition system (DAQ) must process a few hundred thousand interactions per second. However, the CDF detector is only capable of writing to tape up to a few events per second. Note that most  $p\bar{p}$  interactions are diffractive, producing minimum bias events that have no high  $p_T$  end products and are of lesser interest. The more interesting hard-scattering events tend to produce high  $p_T$  particles and have very small cross sections. For example, the total cross section for  $Z$  boson production is about 250 pb. This means there is only one  $Z$  event every 6.7 minutes. Furthermore, due to detector acceptances and efficiencies, only a small fraction of these events are actually recorded by the experiment. Therefore, CDF employs a three level trigger system. The goal of the trigger system is to reduce the event rate down to a manageable level, while maintaining high trigger efficiencies for interesting events. At CDF, we need a rejection factor of about  $10^4 - 10^5$ .

Each level of the trigger is a logical OR of many triggers which select events that have electrons, muons, or jets. At each trigger level, the event rate decreases, as the level of sophistication and processing time increases. CDF's Level 1 and Level 2 triggers are implemented in hardware, while Level 3 is implemented in software. Individual trigger paths can be prescaled in the Level 2 or Level 3 trigger systems which means only a fraction of events that pass a prescaled trigger are accepted. This is done to keep an acceptable livetime for the experiment without raising the trigger thresholds to a high level. Some of these prescale factor are automatically



altered during a run, while some are fixed.

As the cross section for any physics process falls rapidly with increasing transverse momentum, most  $p\bar{p}$  interactions yield events with low transverse momentum end-products. Most trigger paths therefore require events with at least 5-10 GeV of energy (or momentum) to select interesting high- $p_T$  events. The trigger thresholds and efficiencies used for the data selection in this measurement is discussed in Chapter 3.

The Level 1 trigger takes less than  $3.5 \mu\text{s}$  to form a decision and therefore has no *deadtime* (the time interval when the trigger systems cannot react to a beam crossing). The trigger is based on the presence of an energy cluster above some energy threshold in  $\Delta\eta \times \Delta\phi = 0.2 \times 15^\circ$  trigger towers of calorimeters. It also triggers on the presence of muon tracks in the muon chambers. The Level 1 trigger reduces the event rate from 285 kHz to a few kHz with a typical rejection factor of 350. The events that pass the Level 1 trigger are passed on to Level 2.

At Level 2, the average processing time is  $20 \mu\text{s}$ . Therefore the Level 2 trigger incurs a dead time of a few percent. The Level 2 trigger uses information from the calorimeters, tracks from the central fast tracker (CFT) [16] and muon track segments. The energy cluster information is gathered by a hardware cluster finder. The clusters are formed by searching for a seed tower above a certain threshold and adding in neighboring towers which are over a lower threshold. The  $E_T$  and mean  $\eta$  and  $\phi$  are calculated for each found cluster. The CFT is a hardware processor that uses CTC hits to reconstruct tracks with a momentum resolution of  $\delta P_T/P_T^2 = 3.5\%$ . Tracks found by the CFT are matched to clusters in the CEM to form electron candidates or to tracks in the muon chambers to form muon candidates. The Level 2 trigger reduces the event rate to 20-25 Hz with a rejection factor of around 50.

The Level 3 trigger is a software trigger. It is written in FORTRAN and runs a simplified version of the CDF reconstruction code on a farm of Silicon Graphics processors. The Level 3 trigger constructs more complex triggers for various physics processes of interest. The Level 3 reduces the event rate to a few Hz with a rejection factor of 3-4. All events passing Level 3 are spooled to tape for later processing.

## Chapter 3

# The Data Sample

The  $p\bar{p}$  collisions are described using kinematic quantities which are defined transverse to the beamline. The followings are the definitions of variables which are used throughout this analysis. They are defined in the coordinate system shown in Figure 2.2.

- Transverse energy,  $E_T = E \sin(\theta)$ . In the experiment,  $E$  is the energy deposited in the calorimeter, and  $\theta$  is the polar angle measured from the event vertex to the position of the EM shower.
- Transverse momentum,  $p_T = p \sin(\theta)$ . The momentum  $p$  is measured using the CTC, and  $\theta$  is the polar angle of the associated CTC track.
- Invariant mass of the  $e^+e^-$  pair,  $M_{ee} = (E_1 + E_2)^2 - (\mathbf{p}_1 + \mathbf{p}_2)^2$ , where  $E_1$  and  $\mathbf{p}_1$  are one electron's energy and momentum, and  $E_2$  and  $\mathbf{p}_2$  are the other electron's energy and momentum.
- Pseudorapidity,  $\eta = -\ln[\tan(\theta/2)]$ .
- Radius of a cone,  $\Delta R = \sqrt{(\Delta\eta)^2 + (\Delta\phi)^2}$ .

### 3.1 Event Selection

To identify the  $\gamma^*/Z$  boson among the other particles in a  $p\bar{p}$  collisions, we search for the dielectron decay of the  $\gamma^*/Z$ . The signal of an electron in the CDF detector is very distinct. First, the energy is deposited mostly in the EM section of the calorimeter, and the shower is usually contained within a small cluster of towers. The measured track momentum is approximately the same as the measured calorimeter energy. Finally, the track direction matches the cluster position.

The  $e^+e^-$  pair events are divided into five categories based on the calorimeter region where the EM showers are found:

- CC: Central-Central  $e^+e^-$  pairs;
- CP: Central-Plug  $e^+e^-$  pairs;
- CF: Central-Forward  $e^+e^-$  pairs;
- PP: Plug-Plug  $e^+e^-$  pairs;
- PF: Plug-Forward  $e^+e^-$  pairs.

Electron selection begins with the three-level trigger system. The events passing the triggers are later processed with offline reconstruction code. Analysis selection cuts, (also called offline selection cuts) are then applied to further select electron candidates. The result is a sample of  $\gamma^*/Z \rightarrow e^+e^-$  events with a certain fraction of backgrounds.

### 3.1.1 Electron Triggers

The online selection of  $\gamma^*/Z \rightarrow e^+e^-$  events uses a trigger path designed to identify events with at least one high- $E_T$  electron in the central or plug calorimeter. \*

#### Level 1:

The events are required to pass the Level 1 trigger L1\_CALORIMETER. This trigger is on when the energy deposited in any calorimeter trigger tower exceeds a preset threshold. The Level 1 trigger efficiency is 100% (see Section 3.4.1).

#### Level 2:

The events are required to pass the Level 2 trigger:

- Run 1A: CEM\_9\_SEED\_9\_SH\_7\_CFT\_9\_2 or PEM\_20
- Run 1B: CEM\_16\_CFT\_12 or PEM\_20

The central electron trigger CEM\_9\_SEED\_9\_SH\_7\_CFT\_9\_2 requires an energy cluster in the CEM with  $E_T > 9$  GeV and a CFT track with  $p_T > 9.2$  GeV/c. The trigger CEM\_16\_CFT\_12 requires a CEM cluster with  $E_T > 16$  GeV, and a track with  $p_T > 9.2$  GeV/c. The plug electron trigger PEM\_20 requires a PEM cluster with  $E_T > 20$  GeV. For each of these triggers, the ratio of the  $E_T$  in the HAD section to the  $E_T$  in the EM section of the central or plug calorimeter ( $\frac{H_{ad}}{E_m}$ ) is required to be less than 0.125. The Level 2  $E_T$  assumes electron  $z_{vertex}$  to be zero since  $z_{vertex}$  has not yet been reconstructed. The Level 2 trigger efficiency is discussed in Section 3.4.1.

---

\*There is no forward electron trigger. Therefore we do not have Forward-Forward  $e^+e^-$  pairs in the event sample.

### Level 3:

At Level 3, the events are required to pass the following triggers:

- Run 1A: ELE1\_CEM\_15\_10\* or ELE2\_CEM\_18\* or ELE2\_CEM\_25GEV\_Z\* or ELE1\_PEM\_20
- Run 1B: ELEA\_CEM\_22\_Z or ELEA\_PEM\_20\_Z

Run 1A events must pass logical “or” of 4 electron triggers. ELE1\_PEM\_20 is a plug electron trigger and the rest of them are central electron triggers. The ELE1\_CEM\_15\_10\* requires one CEM electron with  $E_T > 15$  GeV. A 3-D track with  $p_T > 10$  GeV/ $c$  is required to point to the electron cluster. The cuts  $L_{shr} < 0.25$ ,  $|\delta x| < 3$  cm, and  $|\delta z| < 5$  cm are imposed. The  $\chi^2_{strip}$  is required to be less than 15.0. (See Section 3.1.6 for a detail discuss on these cuts.) The ELE2\_CEM\_18\* requires one CEM electron with  $E_T > 18$  GeV,  $p_T > 13$  GeV/ $c$ ,  $L_{shr} < 0.2$ ,  $|\delta x| < 3$  cm, and  $|\delta z| < 10$ . The  $\chi^2_{strip}$  is required to be less than 10.0. The ELE2\_CEM\_25GEV\_Z\* is a dielectron trigger. It requires one CEM with  $E_T > 25$  GeV,  $L_{shr} < 0.2$ , and a minimum  $E_T$  on the second CEM, PEM, or FEM electron to be 20, 15, or 10 GeV, respectively. The ELE1\_PEM\_20 is the plug electron trigger which requires  $E_T > 20$  GeV and  $\chi^2_{3 \times 3} < 6$ .

The Run 1B Level 3 triggers are dielectron triggers. The central electron trigger ELEA\_CEM\_22\_Z\* requires one CEM electron with  $E_T > 22$  GeV and  $\frac{H_{ad}}{E_m} < 0.125$ , a corresponding CTC track with  $p_T > 13$  GeV/ $c$ , and a second CEM, PEM, or FEM electron with  $E_T > 20, 15$ , or 10 GeV, respectively. It requires one PEM electron with  $E_T > 20$  GeV and a transverse  $\chi^2$  to be less than 3.0. The second CEM electron is required to have  $E_T > 15$  GeV and  $p_T > 10$  GeV. The second PEM electron is required to have  $E_T > 15$  GeV and a transverse  $\chi^2$  less than 5.0. If the second electron is in the FEM, it is required to have  $E_T > 15$  GeV and

isolation less than 0.2. Note, the  $E_T$  used in Level 3 trigger is  $E_T$  measured at electron's  $Z_{vertex}$ .

The efficiencies of Level 3 triggers are discussed in Section 3.4.1.

### 3.1.2 Electron Clustering

The offline selection of electron candidates begins with the electromagnetic clustering in the EM section of the calorimeters. An electron cluster consists of a seed tower (the tower in the cluster with the largest energy) and shoulder towers (adjacent towers). Towers with EM  $E_T > 3$  GeV are eligible to be seed towers. Towers with EM  $0.1 < E_T < 3$  GeV are eligible to be shoulder towers. Beginning with each seed tower, a cluster is formed by incorporating neighboring shoulder towers until either no further shoulder towers or until the maximum cluster size is reached. The maximum cluster sizes are for the different calorimeter subsystems:

- Central region: three towers in  $\eta$  ( $\Delta\eta \approx 0.3$ ) by one tower in  $\phi$  ( $\Delta\phi \approx 15^\circ$ ). Electrons deposit very little energy in adjacent  $\phi$  towers because of the amount of material between the central wedges.
- Plug region: five towers in  $\eta$  ( $\Delta\eta \approx 0.5$ ) by five towers in  $\phi$  ( $\Delta\phi \approx 25^\circ$ ).
- Forward region: seven towers in  $\eta$  ( $\Delta\eta \approx 0.6$ ) by seven towers in  $\phi$  ( $\Delta\phi \approx 35^\circ$ ).

The size variation accounts for the fact that the physical tower size changes with  $\eta$  while the shower size remains roughly the same.

The final clusters are retained as *electron candidates* if the total  $E_T$  of the cluster exceeds 5 GeV, and the ratio  $\frac{H_{ad}}{E_m}$  of the cluster is less than 0.125.

The energy of the cluster is the sum of the seed and shoulder tower energies. A few corrections are made to the cluster energy. The first correction is the so-called

tower-to-tower correction which is designed to remove gain variations between towers. It is derived from the testbeam data. A non-linearity correction which is also derived from the testbeam data is applied to the measured energy to account for the calorimeter's non-linear response at high energy due to the limited longitudinal depth of the calorimeter. A quadrant-to-quadrant correction is applied to the Run 1B plug and forward electron energy. After these corrections, a global energy scale correction factor determined from  $Z \rightarrow e^+e^-$  events is applied to bring the CEM's overall energy scale to within 0.5% of the  $Z$  mass. The detail discussion of the energy correction can be found in references [17, 18, 19].

### 3.1.3 Electron Geometric and Kinematic Cuts

The electrons are required to be in the kinematic and geometric regions defined in Table 3.1. The details are described in the following paragraphs.

- **Fiducial:** The *fiducial* region of the detector is the area where normal performance and reliable measurements is expected. For example, the gaps in the CEM where wedges meet and the gap at the junction of east and west sides ( $\eta = 0.0$ ) are not in the fiducial region of the CEM. In this measurement, all electron candidates are required to be in the fiducial region.
- **$|\mathbf{z}_{\text{vertex}}| < 60 \text{ cm}$ :** A  $Z$  boson can be produced in any region where the proton and antiproton bunches overlap. To keep the  $\gamma^*/Z \rightarrow e^+e^-$  interaction within the fiducial volume of the detector, and to maintain the calorimeter's projective tower geometry, we require the interaction vertex ( $|z_{\text{vertex}}|$ ) to be within 60 cm of the center of the detector. Here  $|z_{\text{vertex}}|$  is determined by the VTX. For each event, several vertices can be reconstructed using the VTX track segments, particularly at high instantaneous luminosity. The algorithm to select the event  $z_{\text{vertex}}$  in this analysis is discussed in Section 3.1.4.



Detector Region	Central	Plug	Forward
Fiducial	Yes	Yes	Yes
$ z_{vertex} $	$< 60$ cm	$< 60$ cm	$< 60$ cm
$E_T(z_{vertex})$	$> 22$ GeV	$> 20$ GeV	$> 15$ GeV
$M_{ee}$	same	$66 < M_{ee} < 116$ GeV/ $c^2$	same

Table 3.1: The geometric and kinematic acceptance for electron candidates

- **$E_T(\mathbf{z}_{vertex})$ :** Electrons from  $\gamma^*/Z \rightarrow e^+e^-$  decays typically have a large  $E_T$ . In this analysis, the electron candidates' transverse energies measured at the electrons'  $|z_{vertex}|$ 's ( $E_T(z_{vertex})$ ) are required to be greater than 22 GeV, 20 GeV, and 15 GeV for central, plug, and forward electrons, respectively.
- **$M_{ee}$ :** The invariant mass of  $e^+e^-$  pairs ( $M_{ee}$ ) is restrained to be in the  $Z$  mass region:  $66 < M_{ee} < 116$  GeV/ $c^2$ .

### 3.1.4 The Event Primary $z$ Vertex Measurement

The position in  $z$  of the primary event vertex is measured by the VTX. The VTX can provide a 3-D picture of a charged particle which pass through the VTX chamber. The reconstruction routine calculates the primary  $z$  vertex using the tracks of charged particles in the VTX and extrapolates them back to the beam position. The  $z$  position of the intersection of extrapolated tracks and the beam position is the  $z$  vertex.

In the  $\gamma^*/Z \rightarrow e^+e^-$  case, each leg of the  $e^+e^-$  pair has a vertex reconstructed from its track in VTX. However, background events can also leave tracks in VTX. As a result, multiple primary  $z$  vertices can be reconstructed for one event. The following paragraphs discuss the algorithm for selecting primary  $z$  vertex. It was developed for this analysis and it is an improvement compared to the CDF default

algorithm.

First, we define a variable, the hit occupancy in the VTX octant (VTXOCC), which is used in the reconstruction algorithm. The VTXOCC is the ratio of layers in the VTX in which the electron deposits charge divided by the expected number of layers traversed by the electron in the VTX. When a track is in the VTX fiducial region, i.e. there is at least one expected hit, the VTXOCC is given in a number varying from 0.0 to 1.0. Otherwise, it is set to -1. The VTXOCC variable is calculated using one of the offline reconstruction routine. The program starts by collecting all the VTX hits along a road with its center defined by a line between the  $z_{vertex}$  and the position of the EM cluster for an electron candidate. The width of the road is defined by the resolution. Then the number of hits found is divided by the number of wires that are traversed by the road. This yields the VTXOCC of the VTX track.

This measurement uses the following algorithm to select the primary  $z_{vertex}$ .

1. Get a list of  $z$  prime vertices ( $z_{vertex}$ ).

2. nv: number of  $z_{vertex}$ .

if (nv=0) then

if(track) zv=Z(track)

if(.not.track) zv=0

elseif(nv=1)

take this one

else

if (track) zv is the  $z_{vertex}$  closest to

$z_0$  of the track, but not more than 5cm.

if(.not.track) pick the one which yields the largest VTXOCC value.

This algorithm is the same as the standard CDF reconstruction routine except for the decision made when there is no track found, ie. `if(.not.track)`. The standard CDF routine pick the one which has the highest  $z_{vertex}$  classification. The classification represents the quality of the reconstructed  $z_{vertex}$ . It is obtained based on a set of quality criteria. These criteria are related to the number of segments and the number of hits within a segment of the VTX for track “stubs” and the density of vertices. In general, the larger the absolute value of the classification word, the better the quality of the vertex. This choice works fine for the central electrons which most of time have reconstructed CTC tracks and are also required to have tracks in the electron identification cuts (see Section 3.1.6). However, the CTC tracking efficiency falls rapidly to zero in the plug calorimeter region, and the forward region is not covered by CTC. Therefore full 3-D CTC tracks cannot be reconstructed for plug or forward electrons. Hence, for the plug or forward electron, the  $z$  primary vertex is chosen based on the classification of the vertices. We find that this criteria is wrong 23% and 24% of the times for plug and forward electrons, respectively. This study is performed using clean CP and CF samples. We assume the  $z_{vertex}$  returned by central leg is correct. Since the  $\gamma^*/Z e^+e^-$  pair has to come from the same vertex, then if the  $z_{vertex}$  of the opposing leg (plug or forward) is more than 5 cm away from the one reconstructed from central leg, we define the plug’s or forward’s  $z_{vertex}$  to be wrong. After modification, the wrong  $z_{vertex}$  fractions go down to 1% and 5% for plug and forward electrons, respectively.

This improvement is due to the application of VTXOCC variable when there is no CTC track. The VTXOCC states how well the VTX track matches the EM calorimeter shower. A good electron candidate is expected to leave a track in the VTX that points in the direction of the EM cluster. By using this information, the algorithm can veto the vertices of tracks left by backgrounds.

### 3.1.5 CTC, VTX, and SVX Trackings.

Tracking information from the tracking systems together with calorimeter information provides identification of electrons. In the following paragraphs, we discuss how the three tracking systems can be used to identify electron candidates.

For the central electron candidates, the CTC provides momenta (with momentum resolution  $\delta p_T/p_T \approx 0.001 p_T$  in GeV/c), charges, and position of EM showers. This tracking information is important in removing backgrounds in the central region. The details are discussed in Section 3.1.6.

As mentioned before, the track-finding efficiency for tracks in the central tracking chamber falls rapidly in the range of  $\eta$  covered by the plug calorimeters. Therefore, the information from the CTC in the region covered by the plug calorimeter is not used in this analysis. The forward region is not covered by the CTC either. In the following paragraphs, we discuss the VTX and SVX tracking which are implemented on electron candidates in the high  $\eta$  region (plug and forward). A consistency check of these two tracking devices is also discussed.

To identify the presence of charged tracks pointing toward the cluster, the VTX-OCC variables are used for plug and forward electron candidates. The advantage of VTX tracking is that the VTX chamber covers the entire rapidity range in this study. However, it can not measure the momentum or the charge of the charged particle. The VTXOCC is required to be greater than 70% and 50% for plug and forward electrons, respectively (VTX tracking requirement). The corresponding efficiencies are  $(97.8 \pm 0.3)\%$  and  $(97.0 \pm 0.9)\%$ , respectively. Figure 3.1 illustrates how backgrounds can be reduced by requiring that VTX tracks are found for plug electrons in the PP and PF samples. The mass window cut is removed to show how the VTX tracking requirement removes backgrounds at the low as well as at the high mass range. As we discussed in Section 3.1.4, the CDF default algorithm

of  $z_{vertex}$  reconstruction resulted in a wrong  $z_{vertex}$  determination of 23% of the time. Since the VT OCC depends on  $z_{vertex}$ , this results in a low VTX tracking efficiency. The cuts,  $VTX OCC > 50\%$  and  $VTX OCC > 30\%$ , for plug and forward electrons have efficiencies of  $(80.8 \pm 0.9)\%$  and  $(85.1 \pm 0.2)\%$ , respectively. Therefore, an improvement in measuring vertices for plug and forward electrons would also improve the VTX tracking efficiency significantly.

The stand-alone SVX Track Finding method [20] provides SVX tracking information for plug electron candidates. It searches for SVX tracks inside a  $\phi$  cone defined by a PEM cluster and the  $z$  primary vertex. Hence, it uses the same principle as VTX tracking, i.e. finding the tracks which point in the direction of EM cluster. Compared to VTX tracking, SVX tracking can also provide information on the sign of the electron (or positron) candidate. By requiring SVX tracks for PEM showers, we can separate the electron candidates from backgrounds. SVX tracking has an efficiency of  $(94.1 \pm 0.6)\%$  inside the SVX fiducial region <sup>†</sup>. Figures 3.2 illustrates how the backgrounds are removed by requiring that SVX tracks are found for plug electrons in the PP and PF samples. The mass window cut is removed to show how the SVX tracking requirement removes backgrounds at the low as well as at the high mass range. The SVX has an acceptance of 60%. After taking into account of its tracking efficiency, half of the plug electron candidates are rejected. Since the VTX chamber has 100% acceptance for plug and forward electrons, and a higher tracking efficiency than the SVX tracking does, we use the VTX instead of the SVX tracking in this analysis. SVX tracking is used as one of the background estimate methods.

The SVX is mounted inside the VTX. Therefore, if a plug electron has an associated SVX track, a VTX track is expected. Consequently, a plug electron

---

<sup>†</sup>We define the fiducial region of SVX to be the region where at least three layers are expected to be traversed by a charged particle.

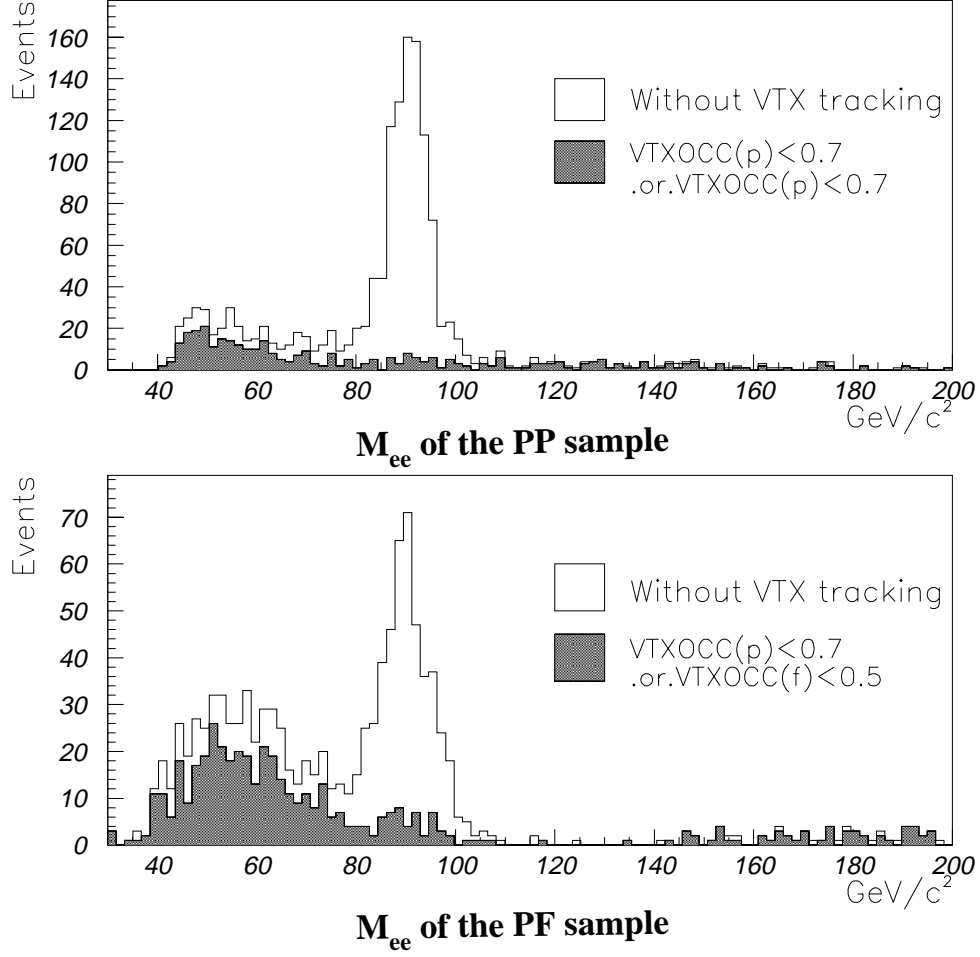


Figure 3.1:  $e^+e^-$  pair mass distribution for the PP (upper plot) and PF (lower plot) samples. The un-shaded histograms show the  $e^+e^-$  pairs before requiring associated VTX tracks for PEM or FEM showers. The shaded histograms show the  $e^+e^-$  pairs which fail the VTX tracking requirement (one or both legs). The un-shaded histogram minus the shaded one gives the  $e^+e^-$  pairs passing VTX tracking requirement. The small bumps at the  $Z$  mass region on the shaded histograms are due to the VTX tracking inefficiency (4% for the PP sample and 5% for the PF sample).

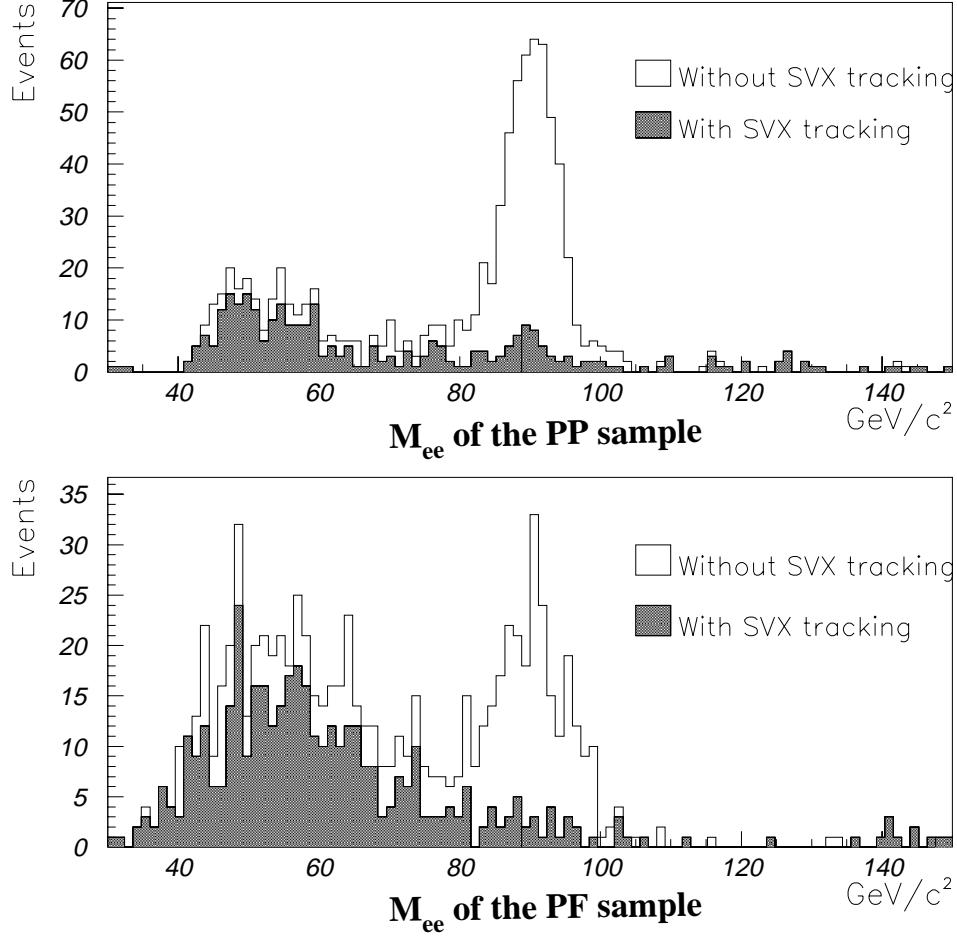


Figure 3.2:  $e^+e^-$  pair mass distribution for the PP (upper plot) and PF (lower plot) samples. The electrons shown in this figure are all in SVX fiducial region. The un-shaded histograms show the  $e^+e^-$  pairs before requiring associated SVX tracks for PEM showers. The shaded histograms show the  $e^+e^-$  pairs which fails the SVX tracking requirement (one or both legs). The un-shaded histogram minus the shaded one gives the distribution for  $e^+e^-$  pairs passing SVX tracking requirements. The small bumps on the  $Z$  mass region in the shaded histograms are due to the SVX tracking inefficiency (12% for the PP sample, and 6% for the PF sample).

with an associated SVX track should have a reasonably good VTXOCC. Figure 3.3 shows the VTXOCC of the first leg versus the VTXOCC of the second leg for the PP sample (upper plot) and PF sample(lower plot), respectively. As you can be seen in the figure, plug electrons which have matching SVX tracks also have associated VTX tracks.

### 3.1.6 Electron Identification Cuts

In this section, we discuss the electron identification cuts which are applied to the electron candidates to reject backgrounds and enhance the fraction of true electron signals.

For the CC, CP, and CF  $e^+e^-$  topologies, one of the central electron candidates is required to pass tight cuts. Those candidates that pass are called tight central electrons (TCE's). The second legs are required to pass relatively looser cuts. The loose central electrons are denoted as LCE's. Table 3.2 lists the identification cuts for the CC, CP, and CF samples. Table 3.3 lists the identification cuts for the PP and PF samples. The details of these cuts are described in the following paragraphs.

**E/p:** We require the ratio of the EM energy, E, of the electron cluster in the calorimeter and the electron's momentum, p, measured in the CTC to lie in the range 0.0 to 4.0 for the LCE's and 0.5 to 2.0 for the TCE's. The cut allows for some photon radiation off the electron.

**L<sub>shr</sub>:** The energy of an electron is generally spread over more than one CEM calorimeter tower. The calorimeter transverse profile, or " $L_{shr}$ ", of a central electron compares the lateral sharing of energy in the calorimeter towers of an electron cluster to electron shower shapes from testbeam data. The variable  $L_{shr}$  is defined



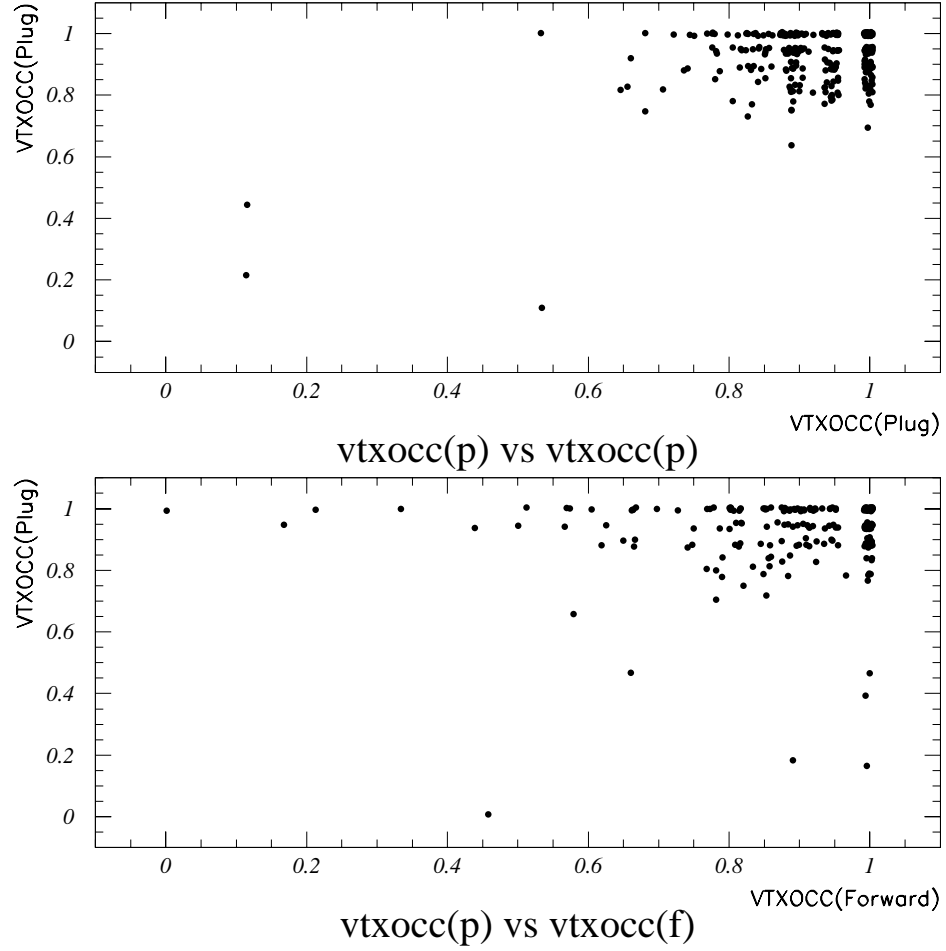


Figure 3.3: (a) Upper plot: the VTXOCC of the first plug electron vs the VTXOCC of the other plug electron for PP electron pairs. Both plug legs are required to have associated SVX tracks. (b) Lower plot: the VTXOCC of the plug electron vs the VTXOCC of the forward electron for PF electron pairs. The plug legs are required to have SVX tracks. These plots illustrate that the VTX tracking and the SVX tracking are consistent with each other.

In good run list.		
One TCE		
$0.5 < E/p < 2.0$		
$L_{shr}$	$<$	0.2
$\chi^2_{strip}$	$<$	10.0
$ \Delta x $	$<$	1.5 cm
$ \Delta z $	$<$	3.0 cm
$\frac{Had}{Em}$	$<$	$0.055 + 0.00045E$ (GeV)
$ z_{vertex} - z_o $	$<$	5.0 cm
Eiso4	$<$	4.0 GeV
or 2nd electron in CEM (LCE):		
$\frac{Had}{Em}$	$<$	$0.055 + 0.00045E$ (GeV)
Eiso4	$<$	4.0 GeV
$0.0 < E/p < 4.0$		
$L_{shr}$	$<$	0.2
$ \Delta x $	$<$	1.5 cm
$ \Delta z $	$<$	3.0 cm
or 2nd electron in PEM		
$\frac{Had}{Em}$	$<$	0.1
$\chi^2_{3 \times 3}$	$<$	3.0
Eiso4	$<$	4.0 GeV
$VTXOCC$	$>$	0.7
or 2nd electron in FEM		
$\frac{Had}{Em}$	$<$	0.1
Eiso4	$<$	3.0 GeV
$VTXOCC$	$>$	0.5

Table 3.2: Selection cuts for the CC, CP, CF categories.

as

$$L_{shr} = 0.14 \sum_i \frac{E_i^{adj} - E_i^{exp}}{\sqrt{0.14^2 E + (\Delta E_i^{exp})^2}}, \quad (3.1)$$

where  $E_i^{adj}$  is the measured energy in a tower adjacent to the seed tower,  $E_i^{exp}$  is the expected energy in the adjacent tower,  $0.14\sqrt{E}$  is the error on the energy measurement, and  $\Delta E_i^{exp}$  is the error on the energy estimate.  $E_i^{exp}$  is calculated

<b>Plug electron:</b>	
$\frac{Had}{Em}$	< 0.1
Eiso4	< 3.0 GeV
$\chi^2_{3 \times 3}$	< 3.0
VTXOCC	> 0.7
Second electron found in plug or forward:	
<b>Plug:</b>	<b>Forward:</b>
$\frac{Had}{Em} < 0.1$	$\frac{Had}{Em} < 0.05$
Eiso4 < 3.0 GeV	Eiso < 3.0 GeV
VTXOCC > 0.7	VTXOCC > 0.5
$\chi^2_{3 \times 3} < 3.0$	
$ \Delta z_{vertex} $	< 5.0 cm

Table 3.3: Selection criteria for Plug-Plug and Plug-Forward events.

using a parameterization from testbeam data. The sum is over the two adjacent towers in the same azimuthal wedge as the seed tower. The variable  $L_{shr}$  is required to be less than 0.2.

**Strip chamber profile ( $\chi^2_{strip}$ ):** The  $\chi^2_{strip}$  is the  $\chi^2$  of the fit of the energy deposited on each of the 11 strips in  $z$  in the CES shower compared to the test beam shape. It is required to be less than 10.0.

**Track matching ( $|\Delta \mathbf{x}| < 1.5 \text{ cm}$  and  $|\Delta \mathbf{z}| < 3.0 \text{ cm}$ ):** The CTC track pointing to the electron cluster is extrapolated to the CES, and the extrapolated position is compared to the shower position as measured in the CES. The variables  $|\Delta x|$  and  $|\Delta z|$  are the distances between the extrapolated track position and the CES strip cluster position in  $x$  and  $z$  directions, respectively.

**Track vertex matching ( $|\mathbf{z}_{vertex} - \mathbf{z}_o| < 5 \text{ cm}$ ):** The difference between the  $z_o$  measured by the CTC track and the  $z_{vertex}$  measured by VTX is required to be less than 5 cm. This ensures that the event vertex is determined correctly in the environment of high instantaneous luminosity.

**$\frac{Had}{Em}$** : Electron showers are usually contained within the EM section of the calorimeter, while hadronic jets deposit a large fraction of energy in the HAD section. Therefore, we require that within a central electron cluster, the ratio of the energy deposited in the HAD ( $Had$ ) and EM sections ( $Em$ ) to satisfy the following:

$$\frac{Had}{Em} < 0.055 + 0.00045E, \quad (3.2)$$

where  $E$  is the energy of the electron cluster in GeV. This sliding cut (linear term) is to maintain a high efficiency for high energy electron candidates. The parameters were determined from test beam data.

**Isolation energy (Eiso4)**: Electrons from  $Z$  decay are expected to be “isolated”, while electrons from other physics processes (e.g. b,c quark decay) are produced with jets of other particles nearby in  $\eta - \phi$  space. The variable Eiso4 is defined as

$$Eiso4 = E_T^{cone} - E_T, \quad (3.3)$$

where  $E_T^{cone}$  is the sum of the EM and HAD transverse energies in all of the towers (including the electron cluster) in a cone of radius  $\Delta R = 0.4$  centered around the electron cluster, and  $E_T$  is the EM transverse energy in the electron cluster.

**$\chi_{3 \times 3}^2$** : The variable  $\chi_{3 \times 3}^2$  is a fit of the lateral sharing of energy in the 3 by 3 towers in  $\eta - \phi$  around the electron cluster’s center to the shape expected from test beam data. It is required to be less than 3.0.

**VTX tracking (VTXOCC)**: We require a VTX track pointing in the direction of a PEM or FEM shower. This requirement is implemented using the variable VTXOCC. We require VTXOCC to be greater than 0.7 and 0.5 for plug and forward electron candidates, respectively. The details of the VTX tracking is discussed in Section 3.1.5.

## 3.2 Backgrounds

After all the electron identification cuts, a total of 9151 events remain in the data sample. However, this  $e^+e^-$  sample still includes a fraction of background events. These background events could have been removed by tightening the electron identification cuts. However, tightening the cuts would result in a loss of efficiency for identifying real electrons. Therefore, the backgrounds must be measured and subtracted from the data sample on a statistical basis.

In this section, we first describe the sources of background in the  $e^+e^-$  sample. Then the method of estimating the total amount of background in the sample is discussed. The background shape is determined using data. The shape is scaled by the total background and subtracted from the observed spectrum on a bin-by-bin basis. The total background is about 1% of the events in the final data sample.

Two types of background are discussed in the following:

- Charge symmetric background.

This type of background comes from jets which fake electron signatures. Jets detected by CDF usually have a signature very different from electrons. The energy is deposited in both the EM and HAD sections of the calorimeter. The jet is normally distributed over a large area in  $\eta - \phi$  space. However, it is possible for some partons to fragment in a way which mimics an electron signal. If two of the jets fake the signatures of a  $\gamma^*/Z$  decay into electrons, they can pass the identification cuts and are backgrounds in the final  $e^+e^-$  sample. Although the probability of such a case is small, the cross section for jet production is much larger than  $Z$  boson production. The backgrounds from this process are charge symmetric and typically have large calorimeter isolation. The notation "charge symmetric" means that the background would likely have equal numbers of same-sign and opposite-sign events, i.e.

$$N_{+-} \approx N_{++} + N_{--}.$$

Electrons from  $\gamma^*/Z$  decay are expected to be “isolated”, i.e. they are not produced in association with jets of other particles nearby in  $\eta - \phi$  space. Although the cut on isolation can remove most of this type of background, there is still some fraction left in the samples, and it is the dominant background in the  $e^+e^-$  data sample. The fraction of this type of background is estimated for each  $e^+e^-$  sample category using the *isolation energy*(Eiso) *extrapolation* method. That is, extrapolating the isolation energy variable for electrons from a region away from the  $\gamma^*/Z$  signal into the  $\gamma^*/Z$  signal isolation region. This method is discussed in Section 3.2.1.

- Mostly opposite charge background.

This type of background comes from the decay products of  $\tau^+\tau^-$ ,  $W^+W^-$ ,  $t\bar{t}$ ,  $b\bar{b}$ ,  $c\bar{c}$  pairs. The  $e^+e^-$  pairs from these sources are mostly oppositely charged. This background results in dielectron, dimuon and electron-muon events.

For the CC topology, the CTC tracking provides charge information on both legs. After all the electron identification cuts, there are only 9 same-sign events in the CC sample (total 2894). The invariant mass spectrum of these 9 events appears to have a  $Z$  peak. This indicates that these 9 events are real  $\gamma^*/Z \rightarrow e^+e^-$  events where the charge of one of the  $e$ ’s is incorrectly reconstructed. This happens when the electron’s trajectory in the CTC is distorted by external bremsstrahlung and  $e^+e^-$  pair production in the detector. Therefore, we keep both the same-sign and opposite-sign charged events in the CC data sample and assume there is no charge symmetric backgrounds after the identification cuts. This assumption is relaxed when calculating the identification efficiency. The mostly opposite charge

background for the CC topology is estimated from the Run 1B data using central-central  $e\mu$  pairs. Both leptons are required to be isolated and no jet cuts are applied. In the mass window  $66 < M_{e\mu} < 116 \text{ GeV}/c^2$ , there are 5 events. Assuming equal acceptance and efficiencies for  $e\mu$  and  $e^+e^-$ , 2.5 events are expected in the  $e^+e^-$  channel for Run 1B. Using the ratio of integrated luminosities for Run 1A and 1B, (0.2), we estimate that there is 0.5 event in  $e^+e^-$  channel for Run 1A. Therefore, the background fraction in the CC data sample is only 0.1%.

For the CP, CF, PP, and PF topologies, the charge symmetric background is measured using the Eiso extrapolation method. For the mostly opposite charge background, the  $e\mu$  measurement is not possible because of limited muon detector coverage. Therefore, the mostly opposite charge background from  $\tau^+\tau^-$ ,  $W^+W^-$ ,  $t\bar{t}$  is predicated using a Monte Carlo program. It is calculated to be less than 0.1% [21]. Since the electrons from  $b\bar{b}$  and  $c\bar{c}$  decays tend to have other particles near the electrons, i.e. not isolated, the  $b\bar{b}$  and  $c\bar{c}$  backgrounds should be covered by the Eiso extrapolation method. For the event topologies where one of the  $e$ 's is a plug electron, the SVX tracking is also used to estimate the background fractions. In the following paragraphs, we discuss the Eiso extrapolation method and SVX tracking method.

### 3.2.1 Isolation Energy Extrapolation Method

The Eiso distributions for electrons and for QCD jets are different. The Eiso distributions of electrons and QCD jets are determined using a pure  $e^+e^-$  pair sample, and a background dominated sample. Then, the Eiso distributions of the data are fit to a linear sum of the signal and background shapes with only the normalization parameters allowed to float. The fit is used to estimate how many background events pass the Eiso cut. For every event sample category, the Eiso

distribution of each of the two legs can be used to estimate the background fraction. Therefore, two independent estimates of the background can be extracted from the data.

In order to determine the Eiso distribution for the signal events, a clean  $\gamma^*/Z$  event sample is made with the identification cuts listed in Tables 3.2 and 3.3. In order to further reduce the backgrounds, a tighter  $\frac{Had}{Em}$  cut ( $< 0.05$ ) and  $e^+e^-$  mass window cut (82-100 GeV/c<sup>2</sup>) are applied. In order to determine the Eiso distribution for the background events, a background dominated sample is made with the following requirements:

1. Require all the identification cuts except for Eiso4 and  $\frac{Had}{Em}$ .
2. Apply  $\frac{Had}{Em} > 0.06$  on the leg which is used to determine the Eiso shape.
3. Apply Eiso4  $> 3$  GeV on the leg which is opposite the leg used to determine the Eiso shape.

Using the clean  $\gamma^*/Z$  event sample and background dominated samples, we can study the Eiso distributions of the  $\gamma^*/Z$  electrons and QCD backgrounds. Figure 3.4 gives examples of the Eiso distributions of the  $\gamma^*/Z$  electrons (signal) and QCD background in the central, plug, and forward calorimeters. As can be seen from the plots, the Eiso distributions for signal and background are different. The background tend to have large Eiso values. Note also that the Eiso distributions for central, plug, and forward electrons are different. This might due to differences in the so called *underlying events*. In the  $p\bar{p}$  collisions, the underlying event is an object that is not very well understood. It is believed to be formed from the beam-beam remnants, initial-state radiation, and possibly from multiple parton interactions. The underlying event produces ambient background energy in the calorimeter that might be included into the  $\Delta R = 0.4$  cone, and as a re-



	Run 1A	Run 1B
$S_{c1}$ (GeV <sup>-1</sup> )	1.6390±0.0660	1.2878±0.0237
$S_{c2}$	0.009007±0.002116	0.008406±0.001141
$S_{c3}$ (GeV <sup>-1</sup> )	0.25±0.07	0.25±0.07

Table 3.4: The parameter values for the Eiso distribution of central electrons. ( $S_c(x) = e^{-S_{c1}x} + S_{c2} \times e^{-S_{c3}x}$ )

sult yields a bigger Eiso value. The light energetic underlying event tends to be boosted into the high  $\eta$  region of the detector, leaving more background energy in the plug or forward region than in the central region. Because of the differences among the Eiso distributions, we determine the Eiso distribution for central, plug, and forward electrons/backgrounds separately.

The Eiso distribution of central electron can be described by

$$S_c(x) = e^{-S_{c1}x} + S_{c2} \times e^{-S_{c3}x}, \quad (3.4)$$

where  $S_{c1}$ ,  $S_{c2}$  and  $S_{c3}$  are parameters. Their values are allowed to be different for Run 1A and Run 1B data and are determined in reference [21]. Table 3.4 lists the results. The Eiso distribution of the QCD background in the central region can be described by

$$B_c(x) = e^{-(x/\sigma_B)^2/2}, \quad (3.5)$$

where  $\sigma_B$  is the parameter. Its value are determined using CC, CP and CF background samples. The Run 1A and 1B background sample distributions are similar. However, the distributions are observed to be a little different between the CC, CP and CF samples. Therefore, the parameter  $\sigma_B$  is determined using CC, CP and CF samples separately. The results are listed in Table 3.5.

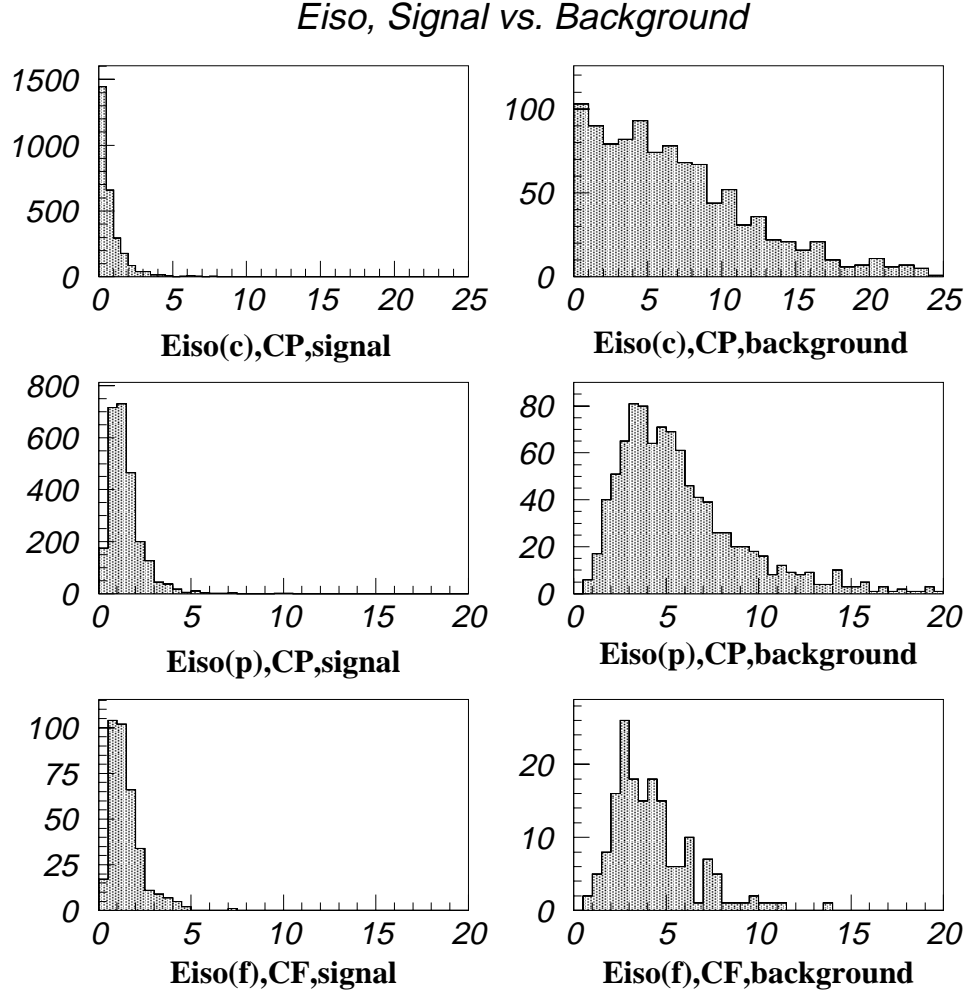


Figure 3.4: Eiso distributions of the  $\gamma^*/Z$  electrons (signals) and QCD backgrounds from central, plug, and forward calorimeters. They are extracted from the clean  $\gamma^*/Z$  event samples and background samples. The unit on Eiso is GeV.

	$\sigma_B$ (GeV)
CC	$9.9 \pm 0.3$
CP	$8.6 \pm 0.2$
CF	$7.5 \pm 0.5$

Table 3.5: The parameter values for the Eiso distribution of QCD background in the central region. ( $B_c(x) = e^{-(x/\sigma_B)^2/2}$ ) It is determined using a background dominated sample.

The application of the Eiso extrapolation method using the central leg yields the background estimates for the CP and CF samples. In order to extract the background, the Eiso distributions of the central electron (Eiso(c)) for the CP and CF samples are fit to a sum of the shapes of electrons and QCD backgrounds, i.e.

$$\text{Eiso}_c(x) = P1 * S_c(x) + P2 * B_c(x) \quad (3.6)$$

Figure 3.5 shows the Run 1A and Run 1B Eiso(c) for the CP and CF samples. The dashed curves in the CP and CF figures are the background predictions. The integral under the background curves in the Eiso(c) region of 0–4 GeV gives the estimated number of background events in the final CP and CF samples.

The general shapes of the Eiso distributions of plug and forward electrons can be described using function:

$$S(x) = x^{s1} e^{-(x/s2)}. \quad (3.7)$$

The Eiso distributions of QCD backgrounds in the plug and forward regions can be described using the function:

$$B(x) = x^{b1} e^{-(x/b2)} \quad (3.8)$$

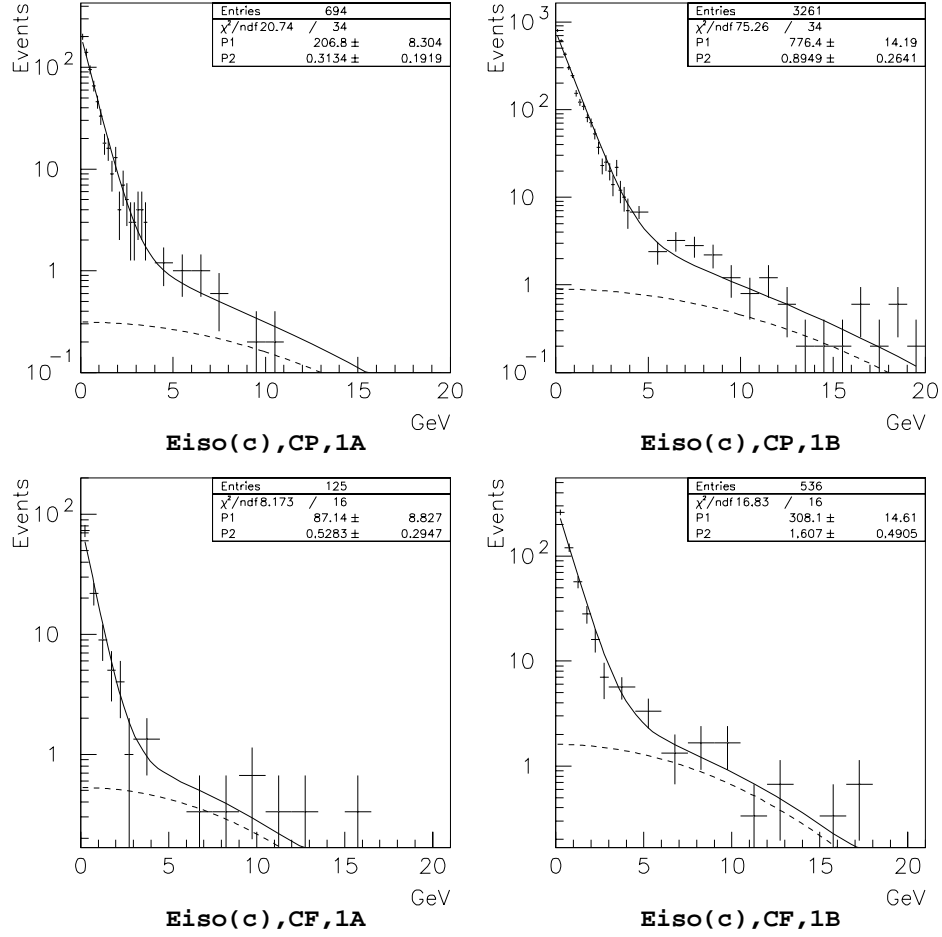


Figure 3.5: The Run 1A (left two) and 1B Eiso distribution of the central electron for the CP and CF samples. They are fitted using Eq. 3.6. The dashed curves are the background predictions. The integral under the background curves in the Eiso(c) region of 0-4 GeV gives the estimated number of background events in the final CP or CF sample.

	1A(CP,PP,PF)	1B(CP)	1B(PP,PF)
s1	$2.53 \pm 0.13$	$2.33 \pm 0.22$	$2.70 \pm 0.29$
s2	$0.38 \pm 0.02$	$0.41 \pm 0.03$	$0.38 \pm 0.03$
b1	$1.93 \pm 0.37$	$2.47 \pm 0.28$	$2.77 \pm 0.42$
b2	$1.74 \pm 0.27$	$1.60 \pm 0.16$	$1.14 \pm 0.14$

Table 3.6: The parameters which define the Eiso distribution of plug electrons ( $S(x) = x^{s^2}e^{-(x/s^3)}$ ) and Eiso distribution of QCD jets in the plug region ( $B(x) = x^{b^2}e^{-(x/b^3)}$ ). 1A(CP,PP,PF) column is for the plug electron from the CP, PP, and PF samples for Run 1A. 1B(CP) column is for the plug electron from the CP sample for Run 1B. The 1B(PP,PF) column is for the plug electron from the PP and PF samples for Run 1B.

	1A+1B(CF)	1A+1B(PF)
s1	$2.96 \pm 0.54$	$4.07 \pm 0.56$
s2	$0.34 \pm 0.06$	$0.27 \pm 0.04$
b1	$8.37 \pm 0.67$	$4.64 \pm 0.95$
b2	$0.38 \pm 0.03$	$0.62 \pm 0.13$

Table 3.7: The parameters which define the Eiso distribution of forward electron ( $S(x) = x^{s^2}e^{-(x/s^3)}$ ) and Eiso distribution of QCD jets in forward region ( $B(x) = x^{b^2}e^{-(x/b^3)}$ ). 1A+1B(CF) and 1A+1B(PF) columns are for the forward electron from the CF and PF for combined Run 1A and Run 1B, respectively.

The parameters, s1, s2, b1, and b2, are determined using data. (signal and background samples). Their values for Run 1A and Run 1B data, or between different  $e^+e^-$  topologies are allowed to be different if they are observed to be different. The parameter values are listed in Tables 3.6 and 3.7 for plug and forward calorimeters, respectively.

The application of the Eiso extrapolation method using the plug leg yields the background estimates for the CP, PP, and PF samples, while the forward leg provides background estimates for the CF and PF samples. The Eiso distribution of the plug leg (Eiso(p)) of the CP, PP, and PF data samples are then fit to the

	Eiso <sub>1</sub> (%)	Eiso <sub>2</sub> (%)	SVX-PEM(%)	Combined(%)
$f^{background}(CP)$	$0.6 \pm 0.2$	$0.8 \pm 0.1$	$0.4 \pm 0.4$	$0.7 \pm 0.1$
$f^{background}(CF)$	$2.4 \pm 0.7$	$1.6 \pm 0.4$	N/A	$1.8 \pm 0.3$
$f^{background}(PP)$	$2.0 \pm 0.3$	$2.0 \pm 0.3$	$1.1 \pm 1.1$	$2.0 \pm 0.2$
$f^{background}(PF)$	$4.4 \pm 0.8$	$3.1 \pm 1.0$	$3.2 \pm 2.0$	$3.8 \pm 0.6$

Table 3.8: The estimated QCD background fractions using different methods. Here, Eiso<sub>1</sub> refers to the Eiso of one leg, and Eiso<sub>2</sub> refers to the other leg. The second column is the estimate using the Eiso(c) distributions for the CP and CF samples, and Eiso(p) for the PP and PF samples. The third column is the estimate using the Eiso(p) distributions for the CP and PP samples, and Eiso(f) for the CF and PF samples. The fourth column is the estimate from the SVX tracking method. The fifth column is the final background estimates using the combined result from the Eiso<sub>1</sub>, Eiso<sub>2</sub> and SVX techniques.

sum of the signal and background shapes, i.e.

$$\text{Eiso}_p(x) = P1 * S(x) + P2 * B(x) \quad (3.9)$$

Figure 3.6 shows the Run 1A and Run 1B Eiso(p) distribution the CP, PP, and PF samples. The dashed curves are the background predictions. The integral under background curves in the Eiso(p) region of 0–4 GeV gives the estimated number of background events in the final CP, PP, and PF samples. The same exercise is applied to the forward leg of the CF and PF samples to extract the background in the samples. The “Eiso<sub>1</sub>” and “Eiso<sub>2</sub>” columns of Table 3.8 list the background fractions in the CP, CF, PP, and PF samples estimated using Eiso extrapolation method for each leg.

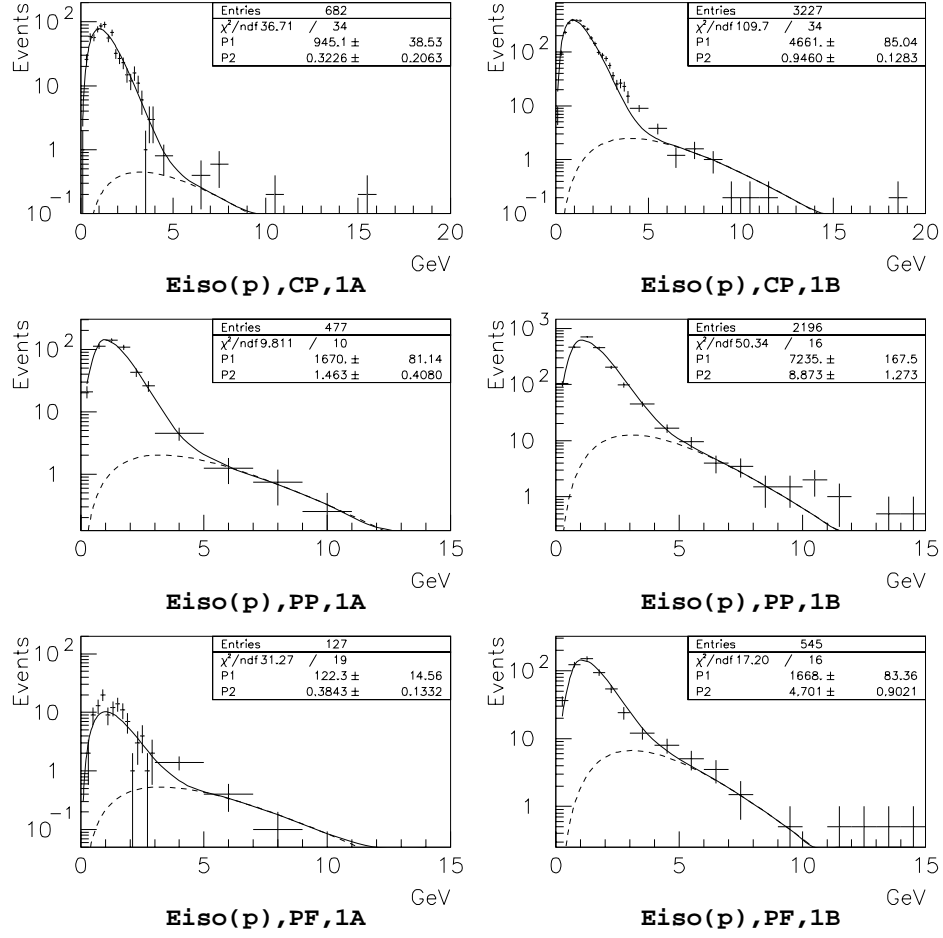


Figure 3.6: The Run 1A (left two) and Run 1B (right two)  $E_{iso}(p)$  distribution for the CP, PP, and PF samples. The dashed curves are the background predictions from the fit.

### 3.2.2 Background Estimate with SVX Tracking

The SVX tracking method searches for SVX tracks which are associated with PEM showers. As discussed in Section 3.1.5, by requiring that SVX tracks point towards the direction of PEM showers, we can separate signal from background events. Electrons are identified by requiring a close match between the SVX track and the shower centroid of the PEM cluster. Therefore, this technique can be used to measure the background fractions in the CP, PP, and PF samples.

We denote:

- $N_{tot}$ : the number of events in the SVX fiducial region after the selection cuts defined in Tables 3.2 and 3.3.
- $N_{pass}$ : the number of events after a SVX tracking requirement is applied to the events for  $N_{tot}$ .
- $N_s$ : the number of signal events in  $N_{tot}$ .
- $N_b$ : the number of background events in  $N_{tot}$ .
- $\epsilon(SVX)$ : the SVX tracking efficiency which is equal to  $(94.1 \pm 0.6)\%$ .
- $f_b$ : the background fraction in  $N_{tot}$ , i.e.  $\frac{N_b}{N_{tot}}$ .

The SVX fiducial requirement is applied throughout this background measurement. The number of the expected SVX hits for the plug EM shower is calculated using the z prime vertex ( $z_{vertex}$ ) and the PEM shower position. The SVX fiducial region cut requires that plug EM showers have at least 3 expected hits in the SVX. The maximum number of SVX hits is 4. We assume that there is no background with the SVX tracking requirement. Therefore we have:



$$\begin{aligned}
N_{tot} &= N_s + N_b \\
N_{pass} &= N_s \epsilon(SVX) \\
N_{tot} &= \frac{N_{pass}}{\epsilon(SVX)} + N_b \\
f_b &= \frac{N_b}{N_{tot}} = 1 - \frac{N_{pass}}{N_{tot} \epsilon(SVX)}
\end{aligned}$$

We assume that the overall background fraction in the entire sample is the same as the background fraction for the restricted sample in the SVX fiducial region. Hence, the quantity  $f_b$  is the background fraction estimated using the SVX tracking method. The results are given in the fourth column of Table 3.8. The last column of Table 3.8 lists the combined results using the Eiso extrapolation method and the SVX tracking technique. The combined results are chosen as the background fraction for each data sample.

### 3.2.3 Background $y$ Distribution

The background fraction from all sources in the CC topology is very small (0.1%) and is neglected. In the CP, CF, PP, and PF samples, the backgrounds from  $\tau^+\tau^-$ ,  $W^+W^-$ , and  $t\bar{t}$  decays (less than 0.1%) are much smaller than the backgrounds from the QCD background, and are neglected.

The background shape in  $y$  is measured using the background sample of non-isolated events. Figure 3.7 shows the background distribution as a function of  $y$  for each of the  $e^+e^-$  categories. Since the background shapes for Run 1A and Run 1B are the same, they are combined and fitted to a sum of two or three Gaussian distributions. The overall levels of the Gaussian distributions are scaled down such that the number of events is equal to the total number of background estimates in Table 3.9. The fitted distributions are used in the calculation of background for the  $d\sigma(\gamma^*/Z)/dy$  distribution. Figure 3.8 shows the combined Run 1A and 1B raw  $y$  distribution for the signal candidates ( $\sum_j (N^{candidates})_{ij}$ ), and for the

background estimate ( $\sum_j (N^{background})_{ij}$ ) shown as the shadowed histogram. The dash-dot curve on Figure 3.8 is the sum of all the Gaussian fit to the CP, CF, PP, and PF background samples (shown in Figure 3.8). The summed curve is scaled down such that the number of events is equal to the total number of background.

### 3.3 Signal versus Background

Table 3.9 lists the number of events remaining after the selection cuts ( $N^{candidates}$ ), the estimated background ( $N^{background}$ ), and the background fraction ( $f^{background} = N^{background}/N^{candidates}$ ) for each of the sample categories. The errors on the backgrounds are the fit errors. The total number of events in the  $e^+e^-$  sample is 9151 with a background of 90.7 events (1.0%).

### 3.4 Event Selection Efficiency

The selection of  $\gamma^*/Z \rightarrow e^+e^-$  events utilizes tight requirements on the electron to reject background events. Unfortunately, these requirements also lead to the loss of a large fraction of real  $\gamma^*/Z$  boson events. In this section, we describe techniques for measuring the efficiencies associated with selecting  $\gamma^*/Z \rightarrow e^+e^-$  events. We measure three types of efficiencies:

1. the efficiency of triggers listed in Section 3.1.1.
2. the efficiency of the electron ID cuts listed in Tables 3.2 and 3.3.
3. the efficiency of the primary  $z$  vertex cut.

In the next chapter, we present a study of the measurement of acceptance which is the fraction of events that pass the geometric and kinematic requirements on

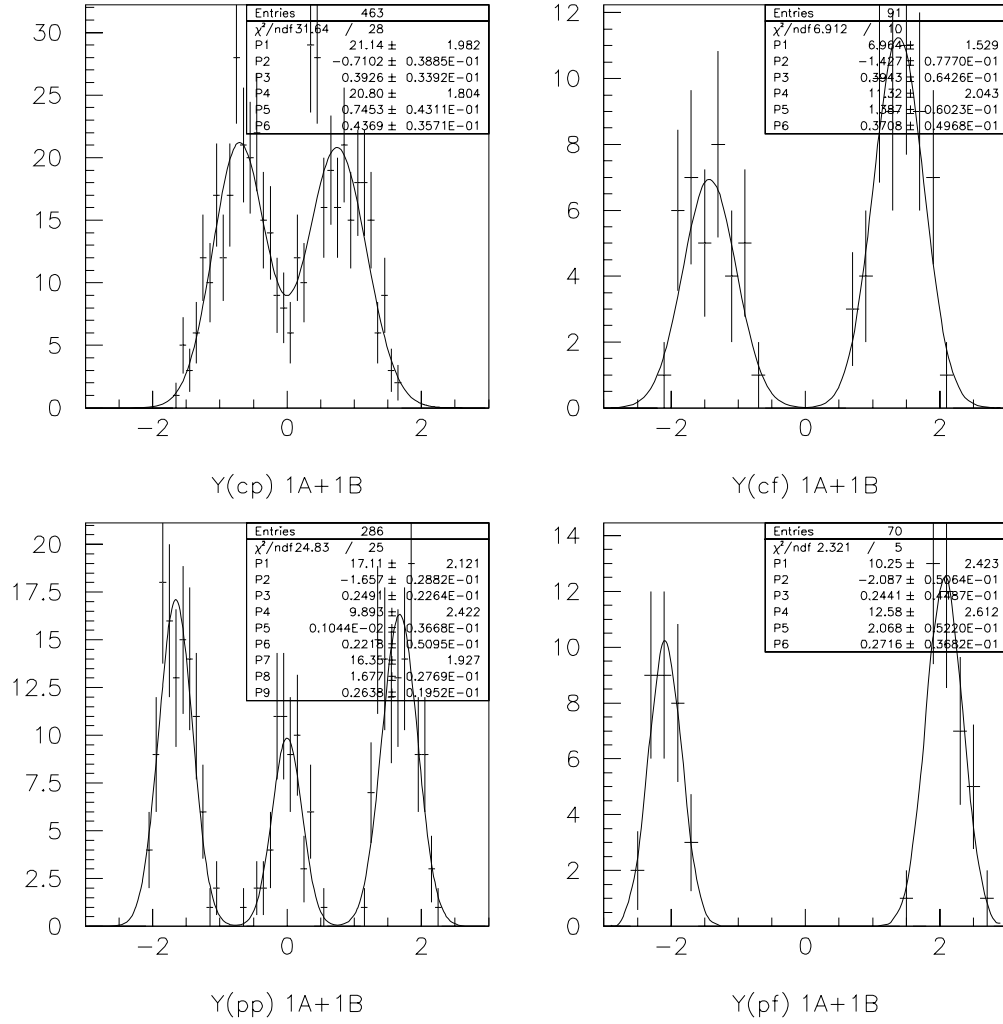


Figure 3.7: Background shapes as a function of  $y$ . It is extracted from background samples.

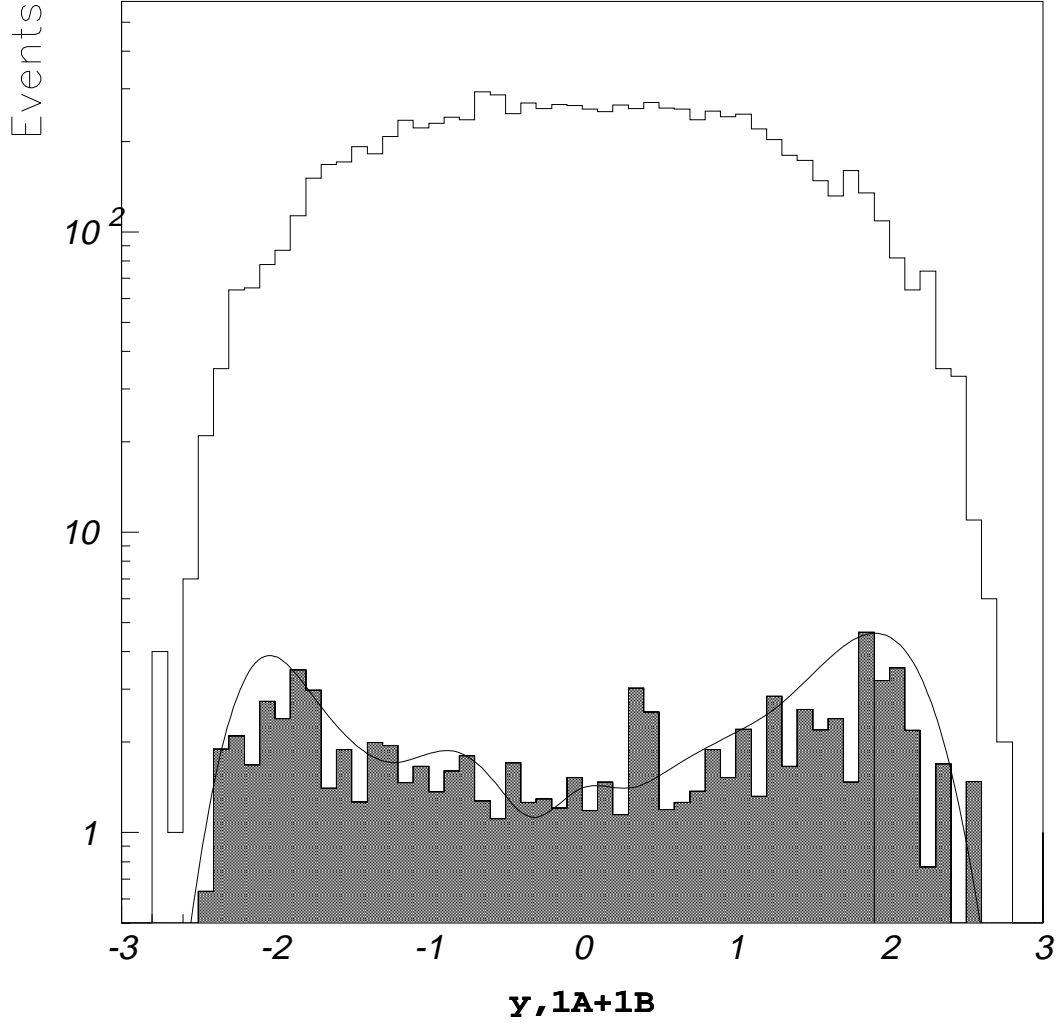


Figure 3.8: The combined Run 1A and 1B raw  $y$  distribution for the  $e^+e^-$  pair candidates and for the backgrounds (shadow histogram). The dash-dot curve on the background histogram is the sum of the fit curves in Figure 3.7 normalized to the total number of background in Run 1A and 1B.

		$N^{candidates}$	$N^{background}$	$f^{background}(\%)$
CC:	1A	499	0.5	0.1
	1B	2395	2.5	0.1
	1A+1B	2894	$3.0 \pm 1.7$	
CP:	1A	670	$6.0 \pm 3.9$	$0.9 \pm 0.6$
	1B	3141	$22.0 \pm 3.1$	$0.7 \pm 0.1$
	1A+1B	3811	$28.0 \pm 5.0$	
CF:	1A	118	$4.0 \pm 2.3$	$3.4 \pm 1.9$
	1B	503	$9.1 \pm 1.5$	$1.8 \pm 0.3$
	1A+1B	622	$13.1 \pm 2.7$	
PP:	1A	225	$3.6 \pm 1.0$	$1.6 \pm 0.4$
	1B	1011	$20.0 \pm 2.0$	$2.0 \pm 0.2$
	1A+1B	1236	$23.6 \pm 2.2$	
PF:	1A	108	$4.8 \pm 1.2$	$4.4 \pm 1.1$
	1B	481	$18.2 \pm 2.9$	$3.8 \pm 0.6$
	1A+1B	588	$23.0 \pm 3.1$	
Total		9151	$90.7 \pm 7.0$	

Table 3.9: Number of events passing all the event selection cuts ( $N^{candidates}$ ) and background estimates ( $N^{background}$ ). The background fraction  $f^{background} = N^{background}/N^{candidates}$ .

the electrons. The efficiency and acceptance are important for the normalization of the  $d\sigma/dy$  measurement.

### 3.4.1 Trigger Efficiency

The selection of the  $\gamma^*/Z$  events sample begins with the three-level trigger (See Section 3.1.1. We measure the efficiency of the trigger for the events that pass all of our offline identification cuts. The trigger efficiency measurement employs a commonly used technique. An event sample is obtained by requiring all the offline identification cuts and an independent or a low threshold trigger. Then the probability that the trigger under consideration is satisfied is the efficiency of that

trigger. In the following paragraphs, we study the efficiencies of the triggers at each level. Since some of the efficiencies are measured in other measurements, we only provide the references and focus on the trigger efficiencies which are measured in this analysis.

### Level 1

The Level 1 electron trigger efficiency, denoted as  $\epsilon_{L1}$ , is the probability that a Level 1 calorimetry trigger is “on” in a collision, given that there is a tightly-selected electron that satisfies the Level 2 electron trigger. In reference [21],  $\epsilon_{L1}$  is measured and the result is 1.0 for both Run 1A and Run 1B.

### Level 2

The level 2 trigger efficiency of the central electrons for Run 1A ( $\epsilon(\text{CEM\_9\_SEED\_9\_SH\_7\_CFT\_9\_2})$ ) is obtained from CDF3120 and CDF3665 [22]. The level 2 trigger efficiency of the central electrons for Run 1B ( $\epsilon(\text{CEM\_16\_CFT\_12})$ ) is obtained from CDF4561 [21].

The level 2 plug electron trigger efficiency,  $\epsilon(\text{PEM\_20}^*)$ , is measured using the CP efficiency sample. The CP efficiency sample is selected using the offline selection cuts listed in Table 3.2, with a tighter mass window cut of  $82 < M_{ee} < 100 \text{ GeV}/c^2$  to ensure a clean  $e^+e^-$  sample. In addition, the central electrons are required to pass the CEM\_16\_CFT\_12 L2 trigger. The efficiency  $\epsilon(\text{PEM\_20}^*)$  is defined to be the fraction of events with the L2 PEM\_20\* trigger on.

For the Run 1A data, the efficiency as a function of  $E_T$  is shown in Figure 3.9. It is fitted using the functional form  $P1 * \text{Freq}((E_T - P2)/P3)$ . Figure 3.9 shows that the  $E_T$  dependence of the trigger efficiency is different on the two sides of the detector. The curve rises a little slower for the east PEM ( $\eta_{det} < 0$ ) than it

does for the west PEM. In addition, the overall  $\epsilon(PEM\_20)$  for  $E_T > 30$  GeV is lower on the west side with  $\epsilon(PEM\_20, E_T > 30 GeV) = 0.947 \pm 0.016$ , versus  $\epsilon(PEM\_20, E_T > 30 GeV) = 0.987 \pm 0.009$  on the east side. The fit parameters on the detector east side are:  $P1 = 0.96, P2 = 24.04, P3 = 1.98$ . The fit parameters on the detector west side are:  $P1 = 1.0, P2 = 23.11, P3 = 1.55$ .

During Run 1B, the PEM L2 trigger PEM\_20 was switched to PEM\_20\_V1 after run 69520. The PEM\_20\_V1 trigger is supposed to have a dynamic prescale factor of 1.0-2.0 according to the trigger table. However, a comparison of the overall L2 trigger efficiency  $\epsilon(PEM\_20) = 2059/2232 = 0.922 \pm 0.006$  (for run before 69520), and  $\epsilon(PEM\_20\_V1) = 252/273 = 0.918 \pm 0.015$  (for run after 69520), does not show any prescaling effect in the PEM\_20\_V1 trigger. Therefore, the two versions of the L2 trigger, the PEM\_20 and the PEM\_20\_V1, are folded together and an overall efficiency  $\epsilon(PEM\_20^*)$  is measured.

Figure 3.10 shows the  $\epsilon(PEM\_20^*)$  as a function of  $\eta_{det}$  and  $\phi$ . Based on the plots, we conclude that  $\epsilon(PEM\_20^*)$  does not depend on  $\eta_{det}$  or  $\phi$ . The efficiency as a function of  $E_T$  is shown in Figure 3.11. The  $E_T$  here is the  $E_T$  with the z vertex input of zero. The efficiency histogram is fitted to the Equation  $P1 * Freq((E_T - P2)/P3)$ . The fit parameters are:  $P1 = 0.98, P2 = 23.08, P3 = 2.15$ .

### Level 3

The Level 3 trigger efficiency is the efficiency of Level 3 relative to the offline analysis. For Run 1A, the Level 3 trigger requirement for the CC, CP, and CF samples is ELE1\_CEM\_15\_10\* or ELE2\_CEM\_18\* or ELE2\_CEM\_25GEV\_Z\* or ELE2\_CEM\_15. The efficiency of the Run 1A L3 trigger has been measured to be 1.00 [21].

The ELE1\_PEM\_20\* trigger is required for the PP and PF data samples in

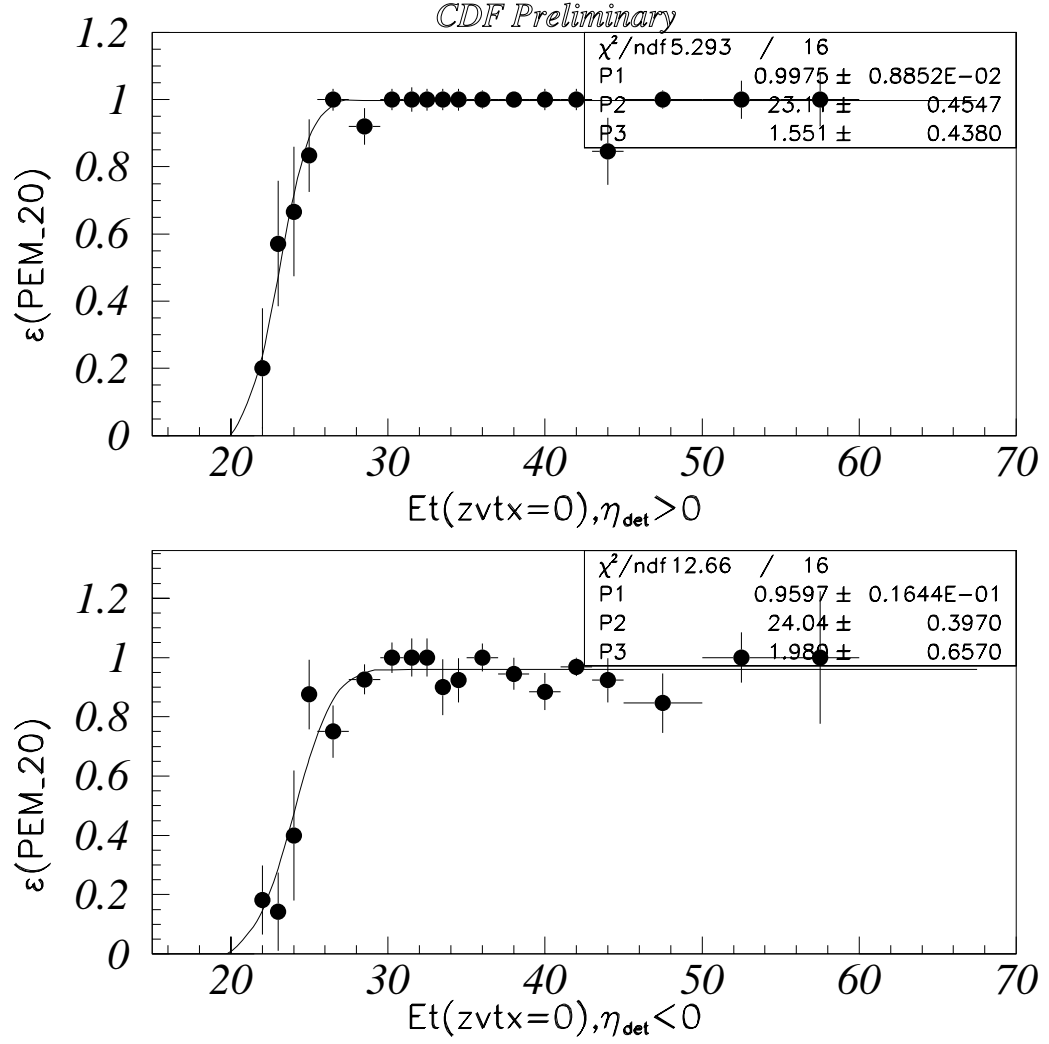


Figure 3.9: Run 1A L2 trigger (PEM<sub>20</sub>\*) efficiency as a function of  $E_t$  assuming that the  $z$  vertex is zero. The unit on  $E_t$  is GeV.



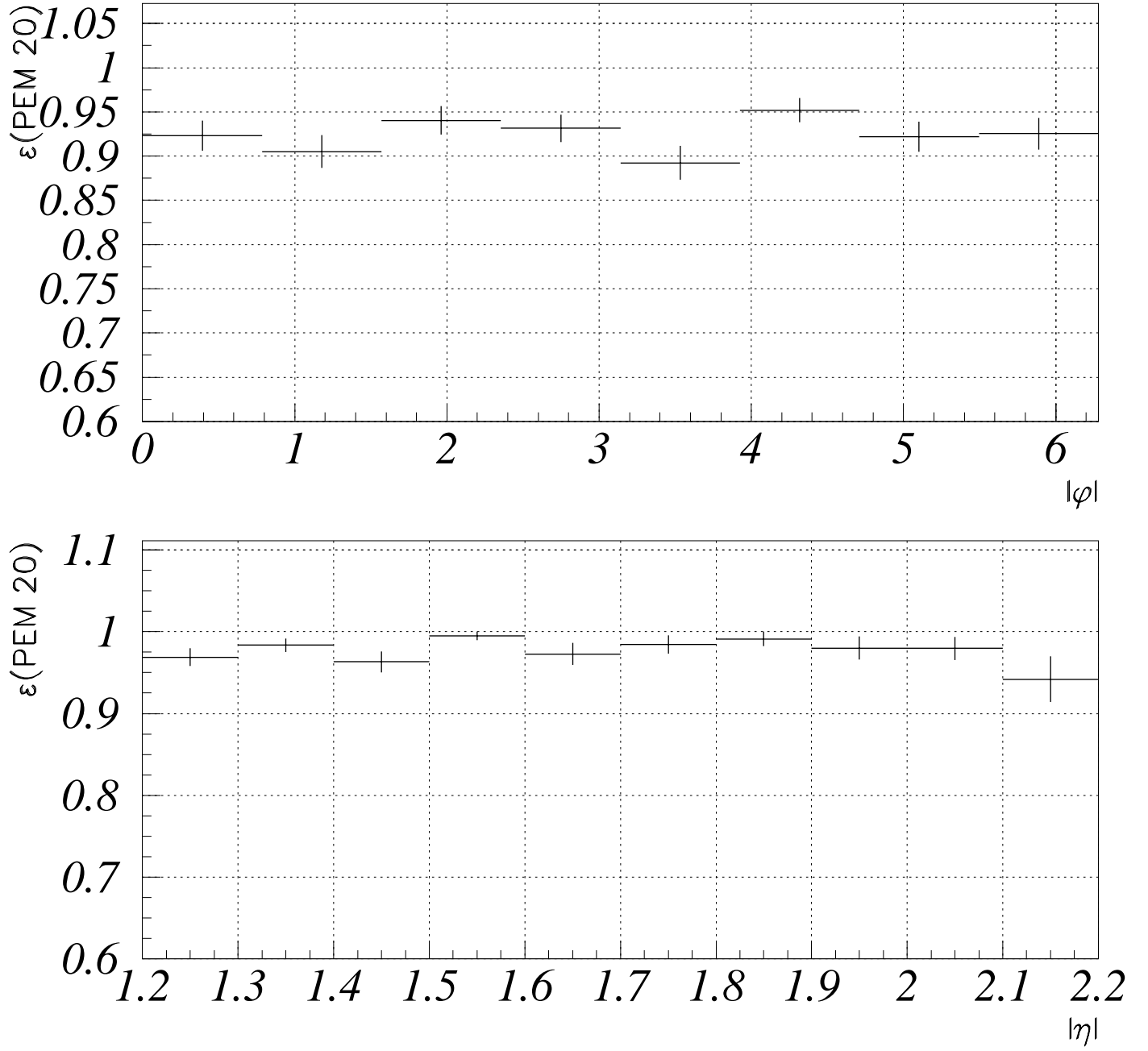


Figure 3.10: Run 1B L2 trigger (PEM\_20\*) efficiency as a function of  $\phi$  (upper plot) and detector Eta (lower plot).

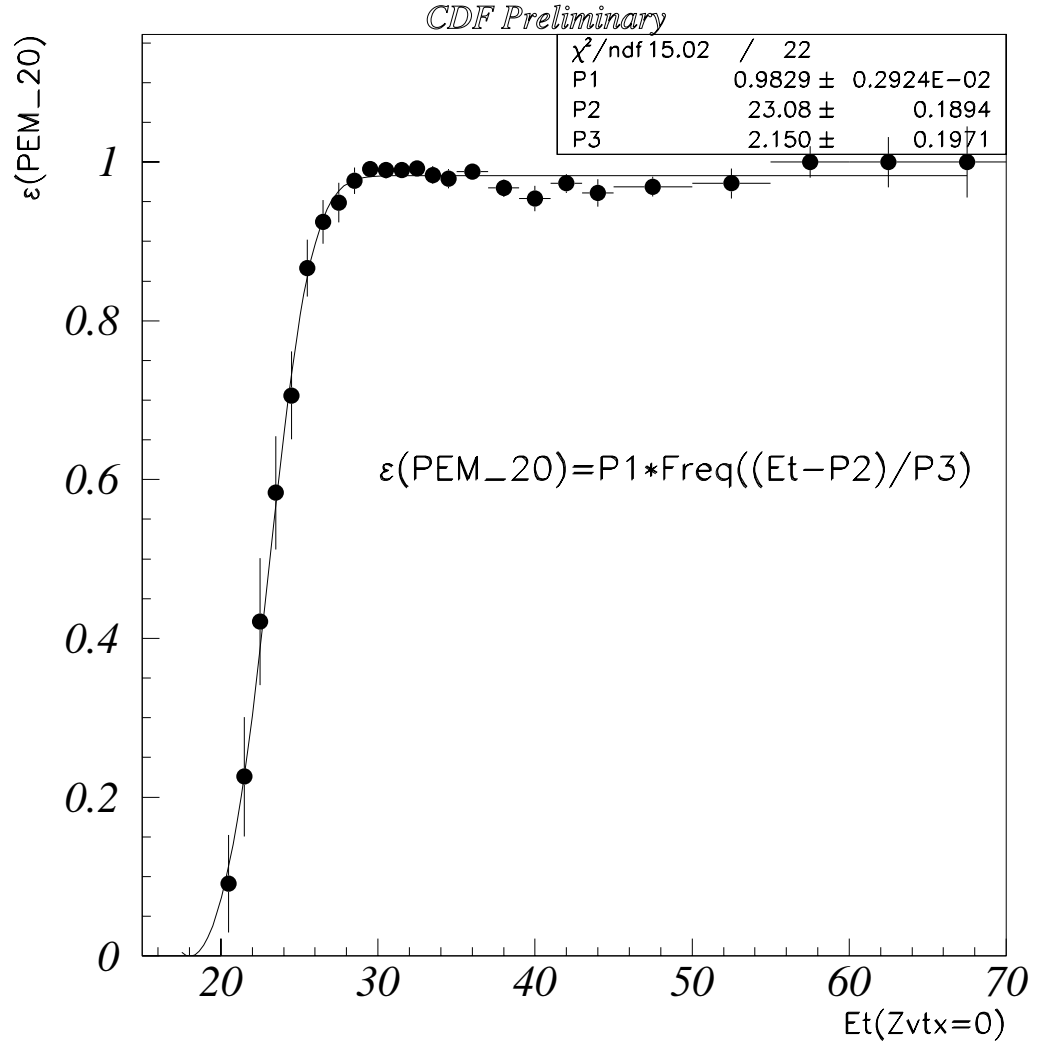


Figure 3.11: Run 1B L2 trigger (PEM\_20\*) efficiency as a function of  $E_t$  assuming that the  $z$  vertex is zero. The unit on  $E_t$  is GeV.

Run 1A. For the CP sample, events from ELE1\_PEM\_20\* are also allowed. The efficiency of the ELE1\_PEM\_20\* trigger,  $\epsilon(\text{ELE1\_PEM\_20}^*)$ , is measured using the CP sample. The selection criteria on the CP sample are basically the offline selection cuts. In addition, the central electron has to pass the L1, L2 and L3 triggers. Here,  $\epsilon(\text{ELE1\_PEM\_20}^*)$  is taken to be the fraction of events with the ELE1\_PEM\_20 trigger on. It is  $\frac{523}{531} = 0.985 \pm 0.005$ . Table 3.11 lists the  $\epsilon(L3)$  of each  $e^+e^-$  sample for Run 1A.

The Level 3 triggers, ELEA\_CEM\_22\_Z\* and ELEA\_CEM\_22\_Z\*, for Run 1B data are dielectron triggers. The efficiency of these dielectron triggers can not be measured directly. Therefore, we investigate the sources which contribute to the inefficiencies at the L3 stage, and then estimate the level of the inefficiency due to the sources. The inefficiencies of the L3 triggers originate from the following sources:

- Energy calibration corrections: These are used in the offline analysis to remove non-linearity and gain variation of the calorimeter. These correction were not applied at the L3 stage. The  $E_T$  used at the L3 trigger is the  $E_T$  using the constructed  $z_{vertex}$ , before energy correction. However, the  $E_T$  used in the offline cuts is  $E_T$  at the  $z_{vertex}$  with energy correction. The ratio in the  $E_T$  before and after gain corrections can be represented by a Gaussian distribution with a mean and a RMS, and the effect can be represented as a shift plus a smearing in energy, which results in a L3 trigger inefficiency.
- $z_{vertex}$  : the  $z_{vertex}$  for plug and forward electrons are recalculated in this analysis. About 24% of the plug electrons and 26.4% of the forward electrons have different a  $z_{vertex}$ . This means that the calculated  $E_T$  is different for events for which the  $z_{vertex}$  is changed.
- CTC tracking: In the ELEA\_CEM\_22\_Z\* trigger, there is a  $p_T > 13$  GeV

Region	Energy Correction Factor		$E_T(newZ vtx)/E_T(oldZ vtx)$	
	mean	RMS	mean	RMS
Central	0.99	0.04	1.0	0.0
Plug	0.94	0.02	1.02	0.17
Forward	0.96	0.03	1.008	0.063

Table 3.10: The mean and RMS of the  $E_T(newZ vtx)/E_T(oldZ vtx)$  and energy correction factors for the electrons from various detector regions.

requirement which has a inefficiency of about 0.5%. Note that we do not require this cut in the offline analysis.

The inefficiency from the first two sources can be estimated using a simulation with a RMS Gaussian smearing. The mean and RMS of the energy correction factors, and the mean and RMS for the ratio of the  $E_t(newZ vtx)/E_t(oldZ vtx)$  for the central, plug and forward electrons are list in Table 3.10. Note that the  $z_{vertex}$  for the central electron is well identified because of the CTC tracking, and the new algorithm for identifying the  $z_{vertex}$  is only implemented on the plug and forward electrons. Hence, the mean and RMS of the  $E_t(newZ vtx)/E_t(oldZ vtx)$  for the central electron are 1.0 and 0.0, respectively.

The Gaussian smearing is applied to the MC data (discussed in Section 4) to simulate the efficiency “turn on” versus  $E_T$ . The efficiency of the L3 trigger for each  $e^+e^-$  category is listed in Table 3.11. Due to the different shapes of the  $E_T$  distributions of electrons from different  $e^+e^-$  topologies, the levels of the inefficiency from the energy correction and from the  $z_{vertex}$  are different. The inefficiency of the CEM\_22\_Z trigger for the CC sample is 0.02%. It is very small and is neglected. The inefficiency of the CEM\_22\_Z trigger for the CP sample is 0.2%, and the inefficiency of the PEM\_20\_Z trigger for the CP sample is 1.5%. Because both triggers are allowed for the CP sample, the combined  $\epsilon(L3)$  for the

$\epsilon(L3)$	CC	CP	CF	PP	PF
1A	1.0	1.0	1.0	0.995	$0.975 \pm 0.006$
1B	1.0	1.0	0.985	0.995	0.997

Table 3.11: The efficiency of the L3 trigger for different  $e^+e^-$  pair categories in Run 1A and Run 1B. The 0.5% inefficiency for the Run 1B CF sample originates from the CTC tracking inefficiency at Level 3.

CP sample is 1.0. The 1.5% inefficiency for the Run 1B CF samples is from a 0.5% CTC tracking inefficiency at Level 3, and a 1.0% of inefficiency from the energy correction. The combined inefficiencies from the energy correction and the  $z_{vertex}$  effect are 0.5% and 0.3% for the PP and PF samples, respectively.

### 3.4.2 Offline Selection Efficiency

As described in Section 3.1.6, a set of electron identification cuts is applied to the EM calorimeter cluster to select electron candidates. Although the cuts are intended to select electrons and veto backgrounds, a fraction of real electron can still fail one or more cuts and thus are not identified. In this section, we describe a measurement of the electron ID efficiency using the CC, CP, and CF samples.

The efficiency samples are obtained by applying the following selection criteria to each of the categories: One central electron has to be a TCE, and the second electron has to be in the kinematic and fiducial region of the detector. In addition, a tighter invariant mass window cut,  $82 < M_{ee} < 100 \text{ GeV}/c^2$ , is applied to the samples. As discussed below, the background in the CC efficiency sample is estimated using the same-sign rate. The background in the CP and CF samples are estimated using the isolation extrapolation method.

The selection efficiency is measured as follows: First measure the efficiency of the cuts on a single leg by observing the fraction of second electrons that pass the

selection criteria. We then combine the efficiencies for each leg to get the selection efficiency for the  $e^+e^-$  pair.

We identify seven efficiencies which must be measured:

1.  $\epsilon(TCE)$ : The efficiency of the TCE cut.
2.  $\epsilon(\overline{TCE} \cdot LCE)$ : The exclusive LCE efficiency, i.e. the probability that an electron fails the TCE cut, but passes the LCE cut.
3.  $\epsilon_{cp}(p)$ : The efficiency of the plug electron cut in the CP sample.
4.  $\epsilon_{cf}(f)$ : The efficiency of the forward electron cut in the CF sample.
5.  $\epsilon_{pp}(p)$ : The efficiency of the plug electron cut in the PP sample.
6.  $\epsilon_{pf}(p)$ : The efficiency of the plug electron cut in the PF sample.
7.  $\epsilon_{pf}(f)$ : The efficiency of the forward electron cut in the PF sample.

As can be seen in Tables 3.2 and 3.3, the selection criteria for plug electrons in the CP and PP samples are slightly different. The Eiso4 cut in the PP sample is tighter. The selection cuts for forward electrons in the CF and PF samples are also different. The  $\frac{Had}{Em}$  cuts in the PF samples are tighter. Hence, the efficiency of these cuts must be measured separately.

The pair event selection efficiencies for the CC, CP, CF, PP, and PF topologies are denoted as  $\epsilon_{cc}$ ,  $\epsilon_{cp}$ ,  $\epsilon_{cf}$ ,  $\epsilon_{pp}$ , and  $\epsilon_{pf}$ , respectively. These are the efficiencies for the  $e^+e^-$  pairs that satisfy the fiducial and kinematic acceptance criteria (see Table 3.1), and also pass the offline selection cuts (see Table 3.2, 3.3).

$\epsilon_{cc}$

The selection criteria for CC pairs is (TCE1.and.LCE2.or.TCE2.and.LCE1). Here 1 and 2 refer to the first and second electron. Thus, the CC sample consists of

events for which both electrons are TCE's, and events for which one electron is a TCE and the other fails the TCE cut but satisfy the LCE requirement. Therefore the overall pair selection efficiency for the CC topology is:

$$\epsilon_{cc} = \epsilon(TCE)^2 + 2\epsilon(TCE)(1 - \epsilon(TCE))\epsilon(\overline{TCE} \cdot LCE)$$

where  $\epsilon(TCE)$  is the efficiency of the TCE cut, and  $\epsilon(\overline{TCE} \cdot LCE)$  is the exclusive LCE efficiency. The efficiencies can be calculated as follows:  $\epsilon(TCE) = \frac{2N_{TT}}{2N_{TT} + N_{T\bar{T}}}$ , and  $\epsilon(\overline{TCE} \cdot LCE) = \frac{N_{T \cdot (\bar{T} \cdot L)}}{N_{T\bar{T}}}$ . Here,  $N_{TT}$  is the number of events with both electrons passing the TCE cut, and  $N_{T\bar{T}}$  is the number of events with one electron passing the TCE cut but the other electron failing the TCE cut. The quantity  $N_{T \cdot (\bar{T} \cdot L)}$  is the number of events with one of the electrons passing the TCE cut and the other electron failing the TCE cut but passing the LCE cut.

However, since no cuts are applied to the second electron in this efficiency sample, the efficiency sample includes background events which must be subtracted from each of the above sub-categories. These backgrounds are mainly from QCD dijets. As was discussed previously, this type of background is expected to be charge symmetric. In order to estimate this background and subtract it from the sample, the  $e^+e^-$  pairs in the efficiency sample are both required to have CTC tracks. This requirement provides the charge information which can be used to estimate the background rate. For the charge symmetric background, we assume that the number of opposite-sign background events is the same as the number of same-sign  $e^+e^-$  pairs. The background subtracted signal is then  $N^{os} - N^{ss}$ .

There are  $\gamma^*/Z \rightarrow ee$  events where the second EM shower (the one opposing the TCE) does not have a track associated with it. These “no second track” events originate from:

- offline tracking failures;

- from an electron losing most of its energy from internal QED radiations;
- from an electron losing most of its energy from external bremsstrahlung and from  $e^+e^-$  pair productions in the detector.

Because of the CTC track requirement for the  $e^+e^-$  pairs in the efficiency sample, the inefficiency due to the “no second track” events can not be measured using this sample alone. The full Drell-Yan sample is used to estimate the number of “no second track” events and add them back into the efficiency sample. These “no second track” events are selected from the Drell-Yan sample by selecting events with a TCE and an opposing EM shower with no track. Both EM showers have  $E_T > 25$  GeV and  $\text{Ciso4} < 0.1$ . ( $\text{Ciso4} = \text{Eiso4}/E_T$ ) The invariant mass spectrum is then fitted. We assume that  $Z$ 's form a Gaussian distribution, and that the background events follow an exponential form. The invariant mass plot and the result of the fit are shown in Figure 3.12. The fit function is given by:

$$P1 * e^{(-P2*x)} + P3 * e^{(-0.5*((x-P4)/2.9)^2)}$$

The number of “no second track” events within the invariant mass window of the efficiency sample ( $N_{notrk}$ ) is estimated from the Gaussian fit parameters. This number of events is added back into the efficiency sample, i.e. added to  $N_{T\bar{T}}$ . Therefore, the overall calculated efficiency also includes the CTC tracking efficiency.

Table 3.12 summarizes the results of the efficiency study for the 1A and 1B data.

$\epsilon_{cp}, \epsilon_{cf}$

The efficiencies  $\epsilon_{cp}(p)$  and  $\epsilon_{cf}(f)$  are extracted from the CP and CF efficiency samples. The cuts which are applied on the central leg are the TCE cuts plus tighter isolation ( $\text{Ciso4} < 0.05$ ) and  $\frac{H_{ad}}{E_m} (< 0.05)$  cuts to further reduce the background in



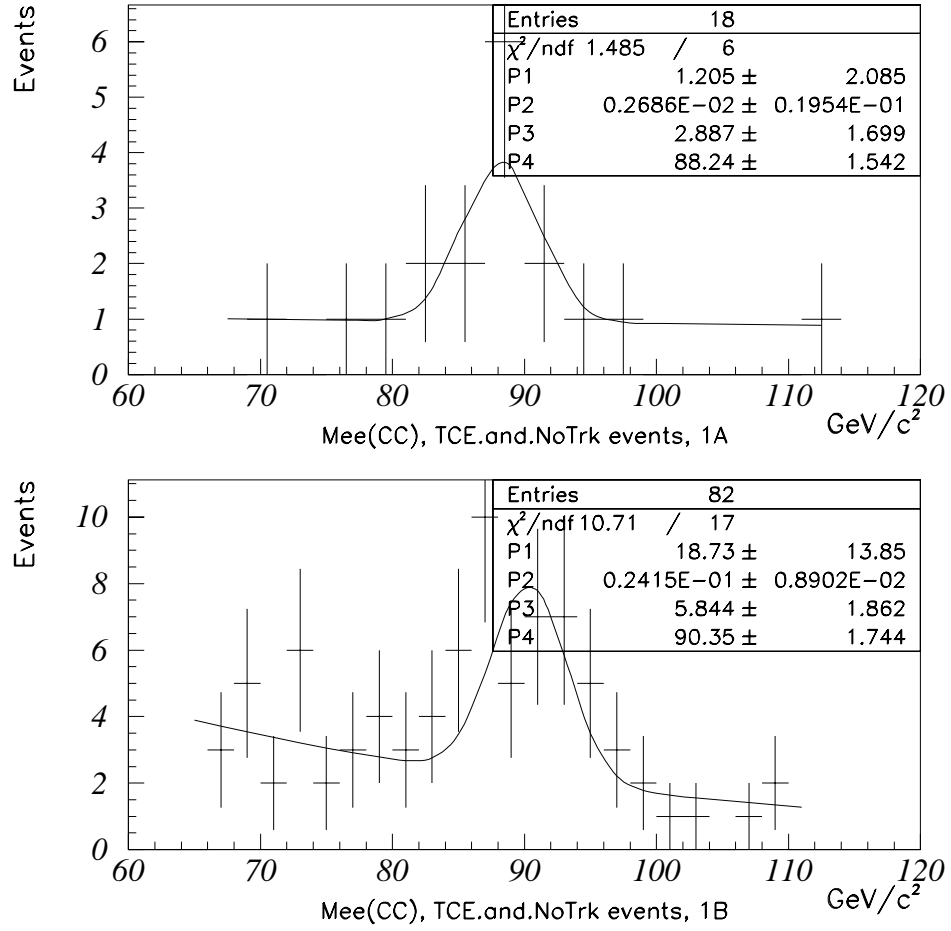


Figure 3.12: Invariant mass distribution of “no second track” events for Run 1A (upper plot) and Run 1B (bottom plot) data.

	Run 1A	Run 1B
$N_{TT}$	457-0	1943-2
$N_{T\bar{T}}$	178-26	781-68
$N_{T\cdot(\bar{T}\cdot L)}$	43-1	206-4
$N_{notrk}$	$7\pm 3.5$	$21.1\pm 7$
$\epsilon(TCE)$	$0.852\pm 0.012$	$0.841\pm 0.006$
$\epsilon(\overline{TCE} \cdot LCE)$	$0.264\pm 0.036$	$0.275\pm 0.015$
$\epsilon_{cc}$	$0.792\pm 0.018$	$0.781\pm 0.009$

Table 3.12: The efficiency for central electrons and for the overall CC sample. The number of same-sign and opposite-sign events is given as  $N^{os} - N^{ss}$ . The number of no track events ( $N_{notrk}$ ) is estimated from the fit to the invariant mass distribution of the “no second track” events.

the sample. In addition, a track isolation cut ( $Tiso < 0.05$ ) is also applied to the central leg. The Tiso is

$$Tiso = \frac{P_T(0.4) - P_T}{P_T},$$

where  $P_T(0.4)$  is the transverse momentum of tracks inside a cone of radius  $R=0.4$  in  $\eta - \phi$  space, and the  $P_T$  is the transverse momentum of the track. The opposing EM shower is required to be in the kinematic and geometric region defined in Table 3.1. A tighter mass window cut of  $82 < M_{ee} < 100$  GeV/ $c^2$  is also applied to the sample.

The isolation extrapolation method is used to estimate the background in the efficiency samples. The estimated background fractions are  $(1.0 \pm 1.0)\%$  and  $(2.0 \pm 2.0)\%$  in the CP and CF efficiency samples, respectively. We consider this to be the level of the systematic error in the measurement of the efficiency. A detailed discussion of all the systematic errors is presented in Chapter 5.

The dielectron event selection efficiencies are:

- $\epsilon_{cp} = \epsilon(TCE)\epsilon_{cp}(p)$

	1A	1B
$\epsilon_{cp}(p)$	$\frac{486}{529} = 0.919 \pm 0.012$	$\frac{2168}{2394} = 0.906 \pm 0.006$
$\epsilon_{cf}(f)$	$\frac{99}{111} = 0.892 \pm 0.029$	$\frac{400}{451} = 0.887 \pm 0.016$
$\epsilon_{cp}$	$0.783 \pm 0.015$	$0.762 \pm 0.007$
$\epsilon_{cf}$	$0.760 \pm 0.027$	$0.746 \pm 0.014$

Table 3.13: Selection efficiencies for plug and forward elections in the CP and CF samples. Here the first two lines are the cut efficiencies of the plug and forward electrons. The last two lines are the dielectron efficiencies of the CP and CF samples.

- $\epsilon_{cf} = \epsilon(TCE)\epsilon_{cf}(f)$

Table 3.13 shows the selection efficiencies for plug and forward electrons,  $\epsilon_{cp}(p)$  and  $\epsilon_{cf}(f)$ , respectively. In addition, the combined dielectron efficiencies for the CP and CF samples,  $\epsilon_{cp}$  and  $\epsilon_{cf}$ , are also presented.

#### $\epsilon_{pp}, \epsilon_{pf}$

The selection efficiencies for plug and forward electrons in the PP and PF samples are determined using the CP and CF efficiency samples. Note that for plug and forward electrons, there is a difference in the acceptance and kinematics between the CP and PP topologies, and between the CF and PF topologies. The PP and PF electrons pairs tends to go to the same side of the detector as compared to CP and CF  $e^+e^-$  pairs, thus resulting in a difference in the average  $E_T$  for the plug and forward electrons in the different samples. The average transverse energy of the plug electron in the PP topology,  $\overline{E_T(p)_{pp}}$ , and PF topology,  $\overline{E_T(f)_{pf}}$ , is higher than the average  $E_T$  of the plug electron in the CP topology,  $\overline{E_T(p)_{cp}}$ . Similarly, the average  $E_T$  of the forward electron in the PF topology,  $\overline{E_T(f)_{pf}}$  is higher than the average  $E_T$  of the forward electron in the CF sample,  $\overline{E_T(f)_{cf}}$ . Therefore, a higher  $E_T$  cut is made on the plug and forward legs in the CP and CF efficiency samples

so that the means of the plug and forward electron  $E_T$  in the CP and CF efficiency samples are the same as in the PP and PF data samples: i.e.  $\overline{E_T(p)_{cp}} = \overline{E_T(p)_{pp}}$ ,  $\overline{E_T(p)_{cp}} = \overline{E_T(p)_{pf}}$  and  $\overline{E_T(f)_{cf}} = \overline{E_T(f)_{pf}}$ .

Using the isolation energy extrapolation method, we find no background in the CP and CF efficiency samples with the higher  $E_T$  cuts.

Finally, we discuss the  $|\Delta(z_{vertex})| < 5.0$  cm efficiency. Unlike other cuts, the  $|\Delta(z_{vertex})| < 5.0$  cm is a global event-wide cut. It requires that the  $e^+e^-$  pair originate from the same vertex, within a 5 cm uncertainty. The efficiency of this cut is measured using the PP and PF samples. Table 3.14 shows the selection cuts applied to the PP and PF samples to measure this efficiency. The efficiencies, denoted as  $\epsilon_{pp}(|\Delta(z_{vertex})|)$  and  $\epsilon_{pf}(|\Delta(z_{vertex})|)$  for the PP and PF samples, respectively, are given in Table 3.15.

The overall dielectron selection efficiencies for the PP and PF samples are:

- $\epsilon_{pp} = \epsilon_{pp}(p)^2 \epsilon_{pp}(|\Delta z_{vertex}|)$
- $\epsilon_{pf} = \epsilon_{pf}(p) \epsilon_{pf}(f) \epsilon_{pf}(|\Delta z_{vertex}|)$

A summary of all the measurements of the selection efficiencies for the plug and forward electrons in the PP and PF samples in given Table 3.15.

### 3.4.3 Primary $z$ Vertex Correction

In this analysis, the event  $z_{vertex}$  is required to fall within  $\pm 60$  cm of the center of the detector. This cut reduces the effective integrated luminosity of the data set. The efficiency of this cut,  $\epsilon_{vertex}$ , depends on the Tevatron beam parameters. It is obtained from minimum bias data [23, 24]. The results are given below:

- Run 1A:  $\epsilon_{vertex} = 0.9552 \pm 0.0105$ ;
- Run 1B:  $\epsilon_{vertex} = 0.937 \pm 0.011$ .

In the good run list	
Event passes electron trigger	
$82 < M_{ee} < 100 \text{ GeV}/c^2$	
<b>Plug electron:</b>	
$E_T$	$> 20 \text{ GeV}$
in Fiducial region	
$\frac{Had}{Em}$	$< 0.05$
Ciso4	$< 0.05$
$\chi^2_{3x3}$	$< 3.0$
VTXOCC	$> 0.8$
$ Z_{vertex}  < 60.0 \text{ cm}$	
Second electron found in plug or forward:	
<b>Plug:</b>	<b>Forward:</b>
in Fiducial region	
$E_T > 20 \text{ GeV}$	$E_T > 15 \text{ GeV}$
$\frac{Had}{Em} < 0.05$	$\frac{Had}{Em} < 0.05$
Ciso4 $< 0.05$	Ciso4 $< 0.05$
$\chi^2_{3x3} < 3.0$	
VTXOCC $> 0.8$	VTXOCC $> 0.7$

Table 3.14: The selection criteria for the samples to measure  $\epsilon_{pp}(|\Delta(z_{vertex})|)$  and  $\epsilon_{pf}(|\Delta(z_{vertex})|)$

	1A	1B
$\epsilon_{pp}(p)$	$\frac{211}{227} = 0.930 \pm 0.017$	$\frac{905}{994} = 0.910 \pm 0.009$
$\epsilon_{pp}( \Delta(z_{vertex}) )$	$\frac{107}{108} = 0.991 \pm 0.008$	$\frac{519}{521} = 0.996 \pm 0.003$
$\epsilon_{pp}$	$0.857 \pm 0.032$	$0.826 \pm 0.017$
$\epsilon_{pf}(p)$	$\frac{403}{447} = 0.902 \pm 0.014$	$\frac{1831}{2063} = 0.888 \pm 0.007$
$\epsilon_{pf}(f)$	$\frac{71}{78} = 0.910 \pm 0.032$	$\frac{282}{312} = 0.904 \pm 0.017$
$\epsilon_{pf}( \Delta(z_{vertex}) )$	$\frac{58}{58} = 1.0$	$\frac{252}{262} = 0.962 \pm 0.01$
$\epsilon_{pf}$	$0.821 \pm 0.032$	$0.772 \pm 0.017$

Table 3.15: Summary of the selection efficiencies (for plug and forward electrons) in the PP, PF samples.

### 3.4.4 Luminosity

In order to determine the luminosity, the total inelastic cross section must be known. The total inelastic cross section at  $\sqrt{s} = 1.8$  TeV has been measured by three groups, CDF [15], E710 [25], and E811 [26]. CDF uses its own measurement [27]. Using the two telescopes of the BBC, CDF has measured the luminosity to an accuracy of 3.6% (4.1%) The integrated luminosities for the data set used in this analysis are  $18.70 \text{ pb}^{-1}$  and  $89.14 \text{ pb}^{-1}$  for Run 1A and Run 1B, respectively.

# Chapter 4

## Monte Carlo

Of all the  $Z$  bosons that decay within the CDF detector, only a fraction of events satisfy the geometric and kinematic requirements imposed on the electrons. These requirements are defined in Section 3.1.3. In this chapter, we describe correction factors, or acceptance, that account for losses incurred by the geometric and kinematic cuts. The kinematic portion of the acceptance is the efficiency of  $Z$  events that pass the  $E_T$  cuts. The geometric portion is the fraction of  $e^+e^-$  pairs that fall within the fiducial part of the detector. The combined geometric and kinematic acceptance yields the overall acceptance for  $\gamma^*/Z \rightarrow e^+e^-$  events.

### 4.1 The Monte Carlo Program

We measure the  $\gamma^*/Z \rightarrow e^+e^-$  acceptance by simulating the production and decay of  $\gamma^*/Z$  boson in the  $p\bar{p}$  collision using a Monte Carlo program. The Monte Carlo program consists an event generator, PYTHIA [28], and a CDF detector simulation programs, QFL [29].

PYTHIA generates a LO QCD interaction, simulates initial and final state QCD radiation, and generates the decay,  $\gamma^*/Z \rightarrow e^+e^-$ . The LO QCD interaction is the  $2 \rightarrow 1$  parton-parton process:  $q\bar{q} \rightarrow \gamma^*/Z$ . The higher order QCD radiation is simulated via the default initial and final state parton shower algorithms of PYTHIA. The initial state parton showers provide the  $\gamma^*/Z$  with additional transverse momentum. The  $\gamma^*/Z$  transverse momentum distribution is fine tuned in the  $Z$   $P_T$  analysis [21] using PYTHIA's  $K_t$  machinery: `MSTJ(41)=1`, `MSTP(91)=2`, and `PARP(92,93)=1.25,10.0` GeV. The CTEQ3L PDFs [30] are used in the calculations. The reasons that we use this old PDFs are (i) the newer PDFs are not available in PDFLIB 6.06, the PDFs library we use in this analysis; (ii) CTEQ3L happens to describe the shape of the  $y$  distribution well (see later Chapter 6).

Two corrections to this lowest order model are important to describe  $\gamma^*/Z$  events at the level required by this measurement. The first is to account for higher order QCD corrections to the LO model. The following  $K$ -factor [9] is calculated and used as an event weight:

$$K = 1 + \frac{4}{3} \left(1 + \frac{4}{3} \pi^2\right) \frac{\alpha_s(M^2)}{2\pi}, \quad (4.1)$$

where  $M$  is  $\gamma^*/Z$  invariant mass and  $\alpha_s$  is the second order (two loop) strong coupling. This K-factor brings the LO cross section,  $d\sigma/dMdy$  (with CTEQ3L PDF's), to within 5% of a NLO QCD calculation [31] using the MRSA' nucleon parton distribution functions for  $M > 50$  GeV.

The second is to account for QED radiation. The process can be written as:

$$q + \bar{q} \rightarrow \gamma^*/Z \rightarrow l^+l^- + n\gamma.$$

The " $n\gamma$ " are photons radiated from any of the charged particles. The effects of QED radiation reduce the observed electron energies when photons and electrons end up in different calorimeter cells. Since the radiating dileptons end up



at lower masses in the invariant mass spectrum, QED radiative corrections alter the final state dilepton invariant mass spectrum. It is found that the second order ( $O(\alpha_{em}^2)$ ) QED correction is small, and the first order ( $O(\alpha_{em})$ ) appears to be adequate for Drell-Yan acceptance calculations [31]. In our Monte Carlo program, a QED dresser, PHOTOS 2.0 [32], adds QED final state radiation to the resonant  $\gamma^*/Z$  decay. Initial state QED radiation is not simulated. Since PHOTOS is used to generate QED radiation, PYTHIA's final state QED bremsstrahlung flag is set off: `MSTJ(41)=1`. Direct calculations indicate that the contribution of initial state QED radiation to the total cross section about the  $Z$  pole is small. [33]

The generated events are processed by the CDF detector simulation programs, QFL, and are reconstructed as data. The QFL program is a widely used simulation used to model the response of the CDF detector to particles. This program assigns a  $z$  vertex to each generated event, simulates tracks in the tracking chambers for charged particles, and calculates the energy deposition in the calorimeters. Subsequently, QFL prepares output banks with a structure that is identical to that of data. This allows us to analyze the Monte Carlo events with the same analysis code that we use to select the  $\gamma^*/Z \rightarrow e^+e^-$  data sample. A few modifications to the QFL have been made. They are discussed in detail in reference [21]. The detector simulation convolutes the geometric and kinematic acceptance with the  $E_T$  and  $\eta_{det}$  dependent Level 2 trigger efficiencies discussed in Section 3.4.1. Therefore, the measured acceptance discussed in the following paragraphs also includes the Level 2 trigger efficiency.

Finally, the simulated events are subject to the detector fiducial, kinematic ( $E_T$ ), and  $M_{ee}$  cuts as discussed in Section 3.1.3. The fraction of events that pass these cuts is the acceptance for  $\gamma^*/Z \rightarrow e^+e^-$  events.

## 4.2 Monte Carlo versus Data

In this section, various distributions for data and Monte Carlo samples are compared for each  $e^+e^-$  pair topology and for all topologies combined. The goal is to see whether the Monte Carlo program can reproduce data, so that we can use the Monte Carlo events to calculate the acceptance. The data are the Run 1A and Run 1B sample passing all the selection requirements discussed in Chapter 3. The Monte Carlo events are required to be in the kinematic and fiducial region defined in Table 3.1. The Monte Carlo events are weighted by a multiplicative factor which includes all the efficiencies of the L1 and L3 triggers and offline selection cuts. The measured Level 2 trigger efficiencies are simulated during the event reconstruction, and therefore are included in the acceptance. To compare the kinematics of the Monte Carlo events with the data samples, the number of Monte Carlo events is normalized to the data.

Figures 4.1 and 4.2 compare the  $E_T$  distributions of Monte Carlo and data samples for Run 1A and Run 1B, respectively. The  $E_T$  of the data is energy corrected and is used in the kinematic cut. Figures 4.3 and 4.4 compare the invariant mass distributions of Monte Carlo and data samples for Run 1A and Run 1B, respectively. The last plots of Figures 4.3 and 4.4 show the  $e^+e^-$  pair mass distributions for all the  $e^+e^-$  categories combined.

In Figure 4.5, we compare Monte Carlo and Run 1A data for the following distributions: the  $\eta_{det}$ , the  $Z$  rapidity, the polar angle  $\theta$  of the  $e^-$  ( $\cos(\theta_{cs})$ ) in the Collins-Soper frame, [34] and the  $Z$   $P_T$ . The  $\cos(\theta_{cs})$  is defined as

$$\cos(\theta_{cs}) = 2 \frac{p^+(e^-)p^-(e^+) - p^-(e^-)p^+(e^+)}{M_{ee}\sqrt{M_{ee}^2 + P_t^2}} \quad (4.2)$$

where  $p^\pm = (E \pm P_z)/\sqrt{2}$ . Note that electron charge information is not available

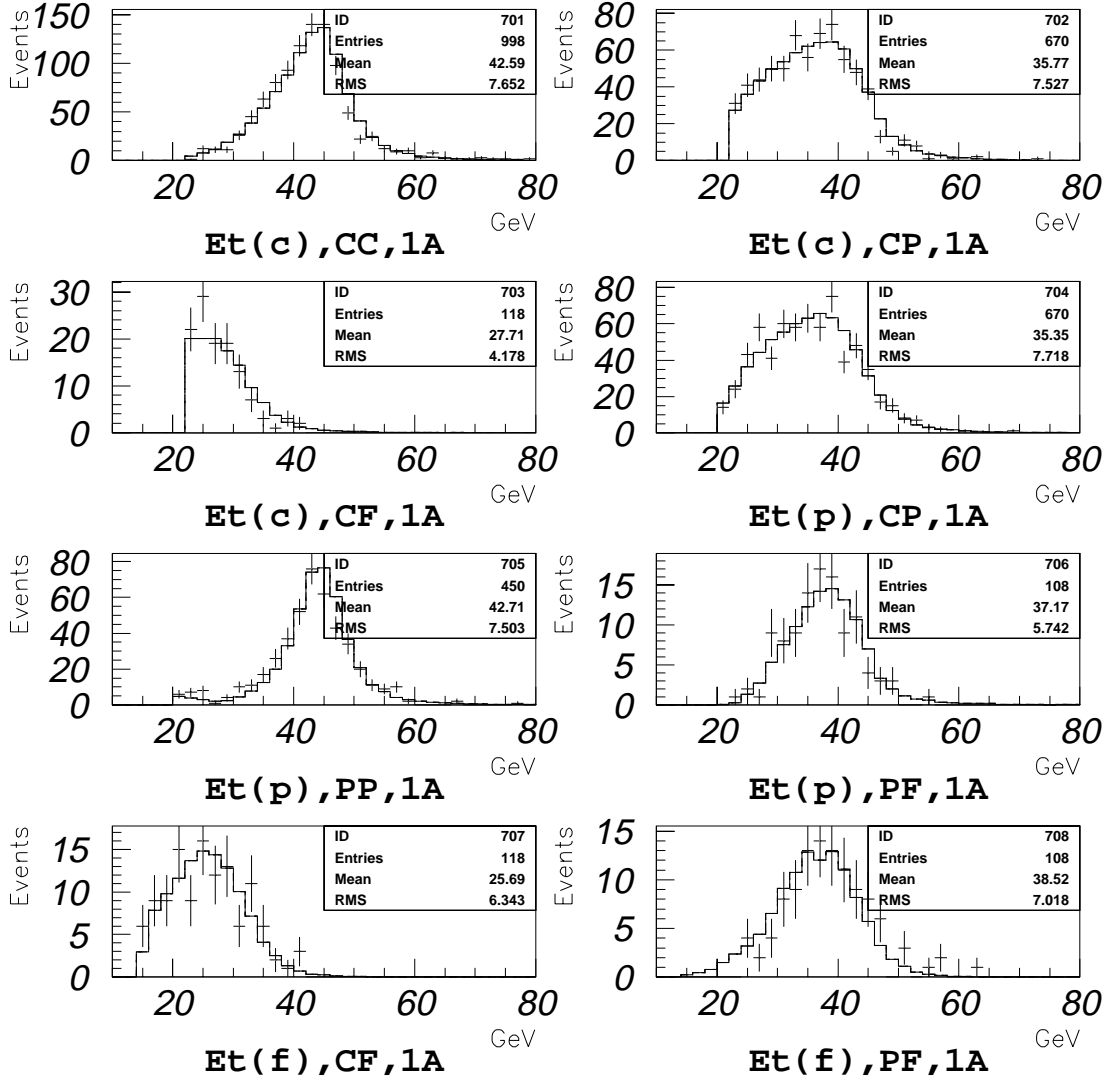


Figure 4.1: Run 1A  $E_T$  distribution for the CC, CP, CF, PP, and PF event topologies. The crosses are data, and the histograms are the Monte Carlo with event counts normalized to the data.

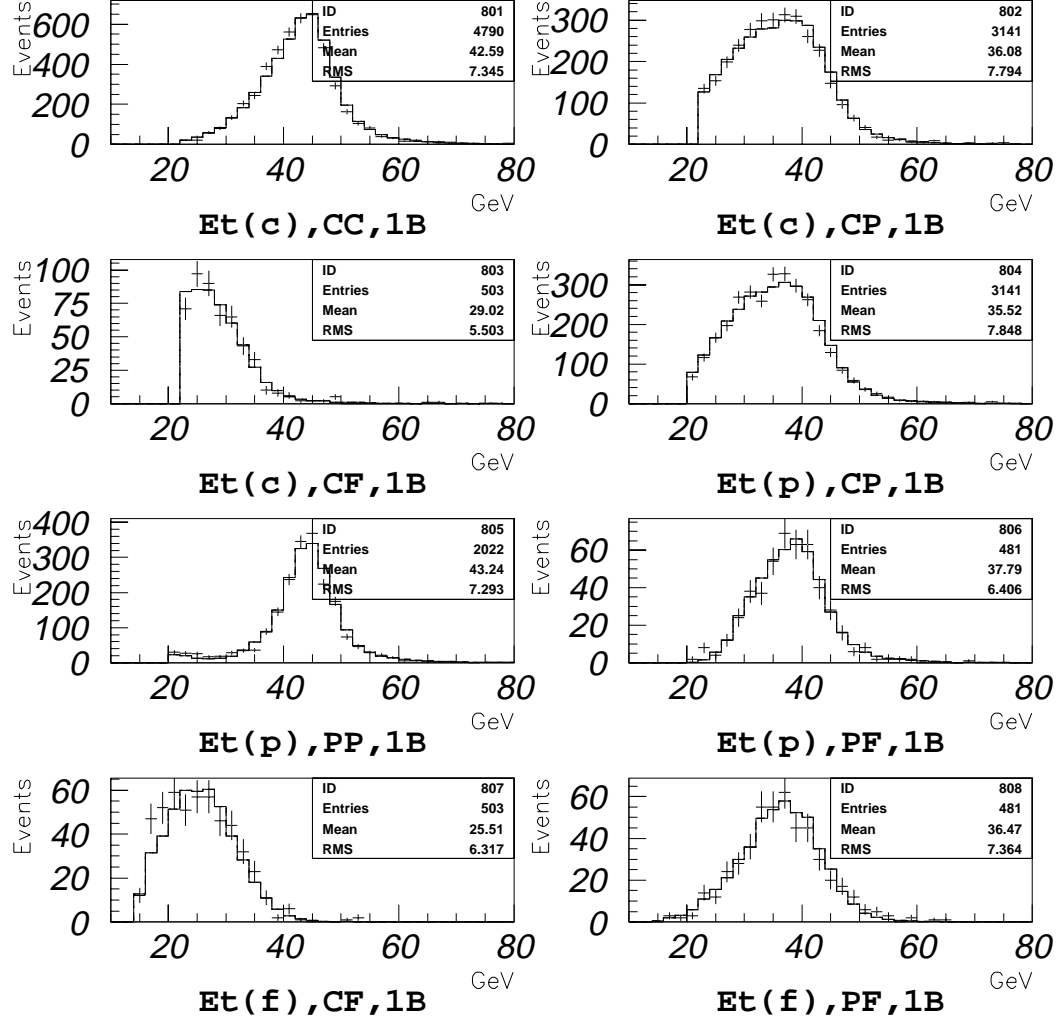


Figure 4.2: Run 1B  $E_T$  distribution for the CC, CP, CF, PP, and PF event topologies. The crosses are data, and the histograms are the Monte Carlo with event counts normalized to the data.

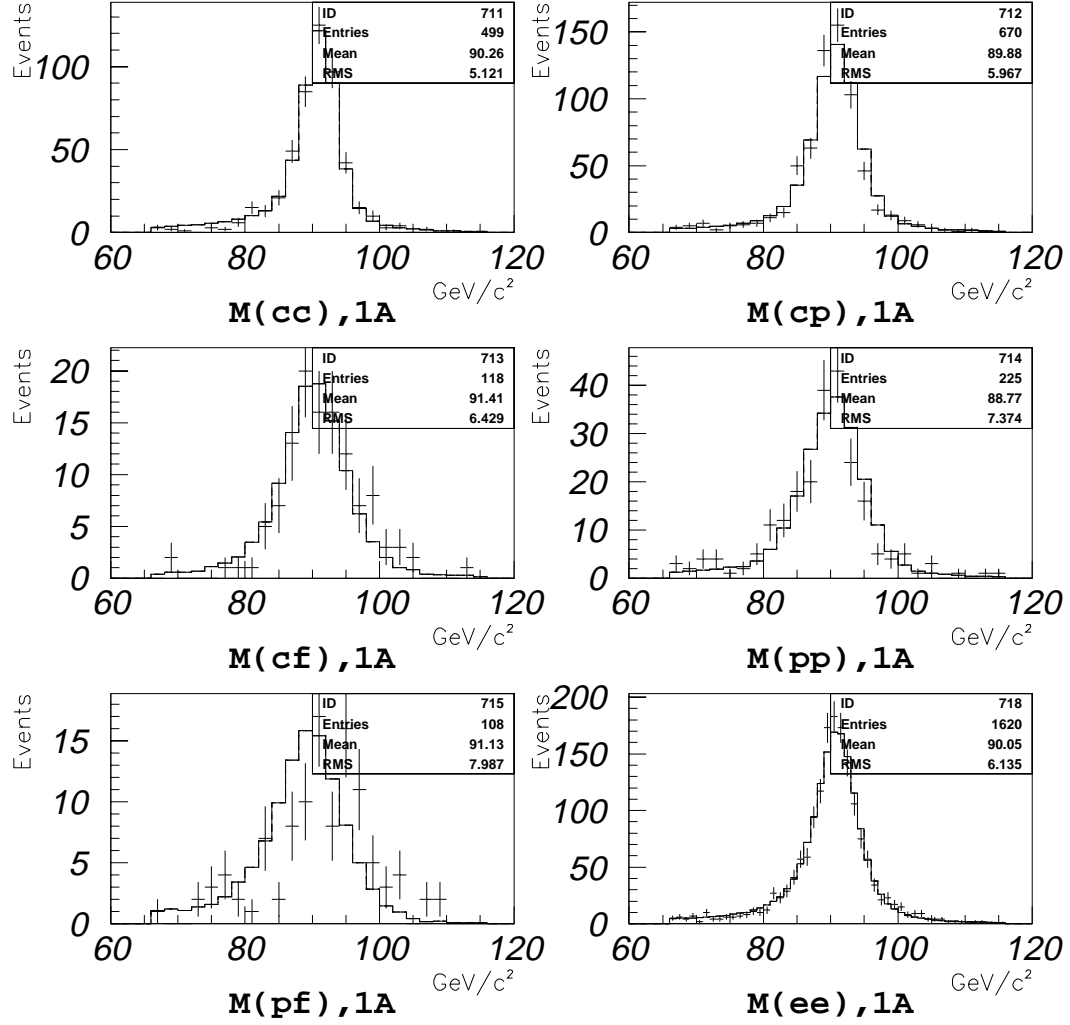


Figure 4.3: Run 1A  $e^+e^-$  pair invariant mass distribution for the CC, CP, CF, PP, and PF event topologies. The last plot (the bottom right) is the mass distribution for events from all  $e^+e^-$  pair topologies. The crosses are data, and the histograms are the Monte Carlo with event counts normalized to the data.

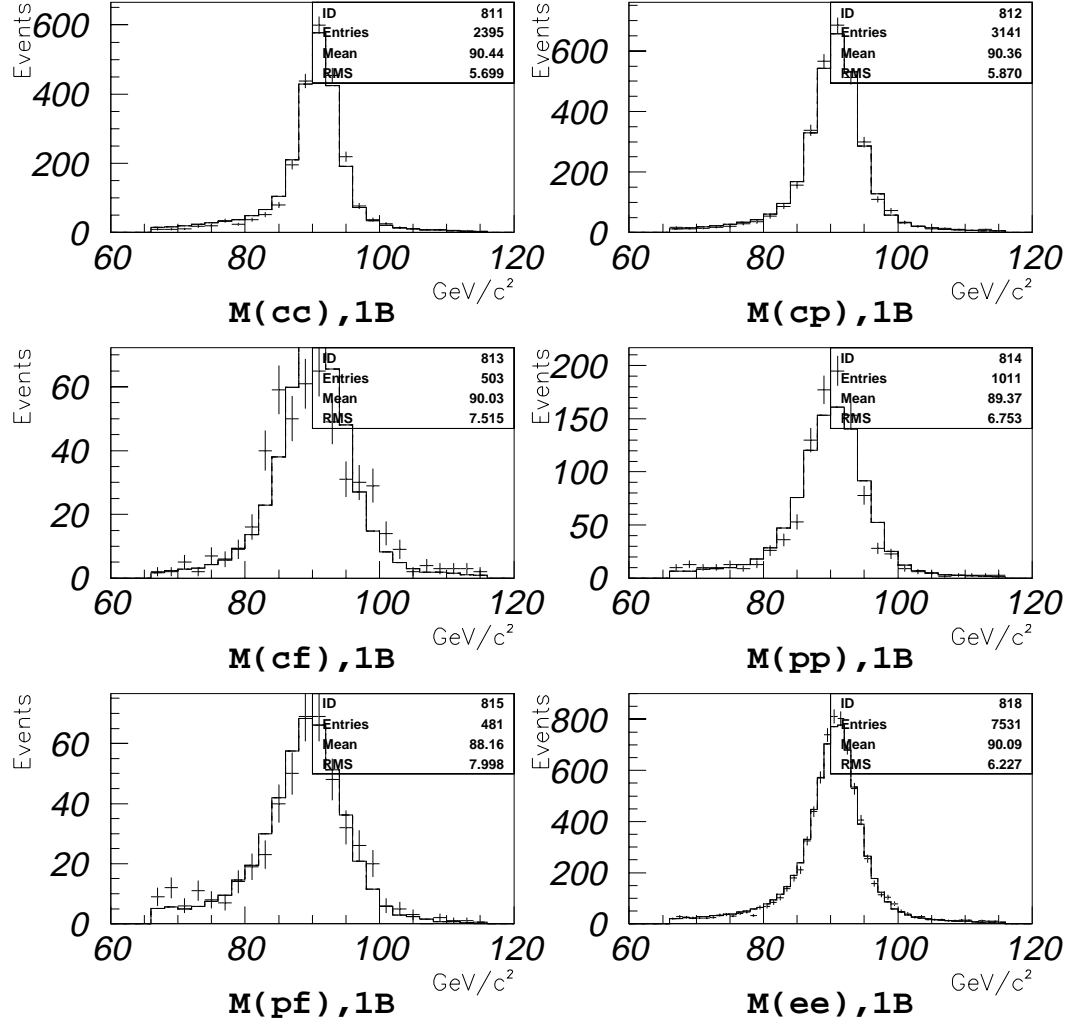


Figure 4.4: Run 1B  $e^+e^-$  pair invariant mass distribution for the CC, CP, CF, PP, and PF event topologies. The last plot (the bottom right) is the mass distribution for events from all  $e^+e^-$  pair topologies. The crosses are data, and the histograms are the Monte Carlo with event counts normalized to the data.

	Run 1A	Run 1B
$A_{cc}$	$0.14633 \pm 0.00057$	$0.14684 \pm 0.00057$
$A_{cp}$	$0.19456 \pm 0.00063$	$0.19384 \pm 0.00063$
$A_{cf}$	$0.03273 \pm 0.00029$	$0.03265 \pm 0.00028$
$A_{pp}$	$0.05262 \pm 0.00036$	$0.05297 \pm 0.00036$
$A_{pf}$	$0.02757 \pm 0.00026$	$0.02780 \pm 0.00026$

Table 4.1: The acceptances for the CC, CP, CF, PP, and PF  $e^+e^-$  topologies. The uncertainties of the acceptances shown here are only from Monte Carlo sample statistics.

for PP and PF events. Therefore, the  $\cos(\theta_{cs})$  distribution plot includes only the events from the CC, CP, and CF samples. Figure 4.6 shows the same distributions as in Figure 4.5 for the Run 1B data. As can be seen in the Figures, the Monte Carlo program used in this analysis does a good job of reproducing the kinematics of the  $p\bar{p} \rightarrow ee(\gamma^*/Z) + X$  process.

### 4.3 Acceptance

The acceptance for each of the  $e^+e^-$  pair topologies is given in Table 4.1. The uncertainties of the acceptances that are shown in Table 4.1 are from Monte Carlo events statistics only. The systematic error on the acceptance is discussed in Section 5.

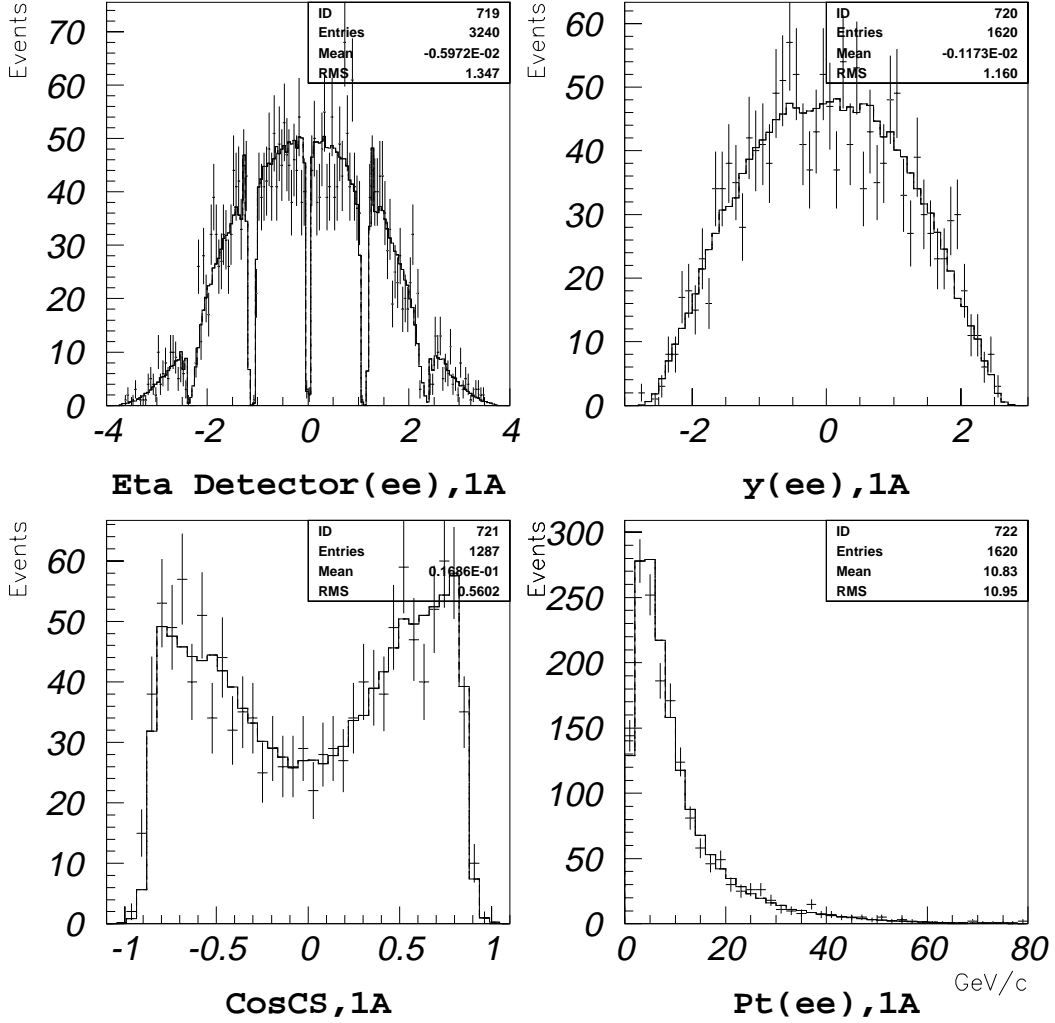


Figure 4.5: Run 1A  $\eta_{det}$ , Z rapidity,  $\cos(\theta_{CS})$  and Z  $P_T$  distributions. The crosses are the data from all  $e^+e^-$  pair topologies, and the histograms are the Monte Carlo with the Monte Carlo weighted by the selection efficiencies. The Monte Carlo event counts are normalized to the data.



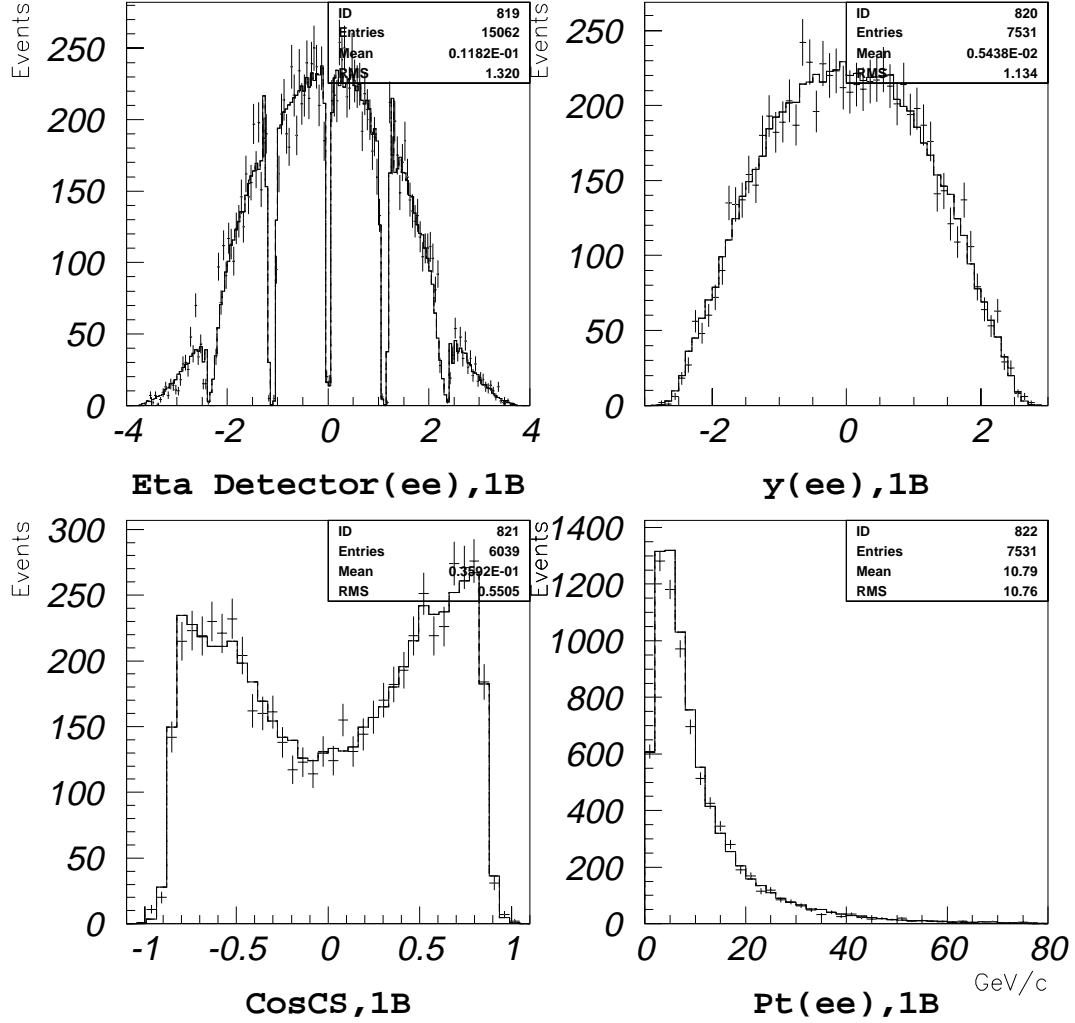


Figure 4.6: Run 1B  $\eta_{det}$ ,  $Z$  rapidity,  $\cos(\theta_{CS})$  and  $Z P_T$  distributions. The crosses are the data from all  $e^+e^-$  pair topologies. The histograms are Monte Carlo events with the Monte Carlo weighted by the selection efficiencies. The Monte Carlo event counts are normalized to the data.

## Chapter 5

# Systematic Errors

This chapter discusses the potential sources of systematic uncertainties. These uncertainties affect the event counts, the efficiency, and the acceptances, which are necessary pieces of information to calculate the cross section. Therefore, the systematic errors on the cross section have to be estimated. In the following paragraphs, we list all the possible sources of systematic uncertainties and estimate them one by one.

We consider the following sources of systematic uncertainties:

1. background subtraction;
2. the background in the efficiency sample;
3. the choice of PDFs;
4. the  $Z$   $P_T$  distribution;
5. the energy resolution of the calorimeter.

## 5.1 Systematic uncertainty from the background subtraction

The background estimate affects the event count. Therefore, the systematic error in the background estimate introduces a systematic uncertainty in the measurement of  $\sigma(\gamma^*/Z)$  and  $d\sigma(\gamma^*/Z)/dy$ . For the CC sample, the background rate is very low (0.1%). Therefore, we set the systematic error for the CC sample to zero. For the other samples, there are three different methods to estimate the background (see Section 3.2). The difference between the results from the different methods can be used as an estimate of the systematic uncertainty in determining the background. Table 5.1 lists differences in background obtained using different methods. It is calculated from Table 3.8. As can be seen, the average difference between the estimates from the two legs using Eiso distribution is  $0.22 \pm 0.20\%$ , which is very small. This means the two outcomes from the Eiso extrapolation method applied on each of the two legs are consistent. The SVX-PEM and Eiso extrapolation are two independent methods to estimate the backgrounds. The Eiso method uses the calorimetry information, while the SVX-PEM method uses tracking information in addition. The difference between the outcomes from these two methods is a reasonable estimate of the systematic uncertainty on the background rate in the samples. Hence, we assign the difference between the background estimates extracted from the SVX-PEM method and from the Eiso method (combined) as the systematic error. As can be seen in Table 5.1, the systematic error in the background fraction is estimated to be 0.5%. This results in a 0.9 pb uncertainty in total  $Z$  cross section measurement.

For the  $d\sigma/dy$  measurement, the systematic error in the  $i$ th  $y$  bin is  $0.5\% \times (1 - Rcc(i))$  of the cross section in that bin. Here  $Rcc(i)$  is the fraction of events

	Eiso <sub>1</sub> -Eiso <sub>2</sub> (%)	mean(Eiso <sub>1</sub> , Eiso <sub>2</sub> )(%)	(SVX-PEM)-mean(Eiso <sub>1</sub> , Eiso <sub>2</sub> )(%)
CP	$0.2 \pm 0.2$	$0.8 \pm 0.1$	$0.4 \pm 0.4$
CF	$0.8 \pm 1.8$	$1.8 \pm 0.3$	N/A
PP	$0.0 \pm 0.4$	$2.0 \pm 0.2$	$0.9 \pm 1.1$
PF	$1.3 \pm 1.3$	$3.9 \pm 0.6$	$0.7 \pm 2.1$
All	$0.22 \pm 0.20$		$0.5 \pm 0.4$

Table 5.1: The quantity (Eiso<sub>1</sub>-Eiso<sub>2</sub>) is the difference between the  $f^{background}$  using one leg's (Eiso<sub>1</sub>) and the other leg's (Eiso<sub>2</sub>) values. The quantity (mean(Eiso<sub>1</sub>, Eiso<sub>2</sub>)) is the mean of the values of Eiso<sub>1</sub> and Eiso<sub>2</sub>. The quantity (SVX-PEM-mean(Eiso<sub>1</sub>, Eiso<sub>2</sub>)) is the difference between the  $f^{background}$  from (SVX-PEM) method and the Eiso method.

from the CC category in the *i*th bin ( $R_{cc}(i)=N_{cc}(i)/N_{tot}(i)$ ).

## 5.2 Systematic uncertainty from the background in the efficiency sample

The CP and CF efficiency sample are used to measure the efficiencies of the cuts for plug and forward electrons, respectively. This measurement is discussed in Section 3.4.2. The CP and CF efficiency samples are selected by requiring the central electron to pass very tight cuts and the opposing EM shower to be in the kinematic and geometric region. In addition, a tighter mass window cut  $82 < M_{ee} < 100$  GeV is applied to the samples.

Using the isolation extrapolation method, we estimate the background fractions to be  $(1.0 \pm 1.0)\%$  and  $(2.0 \pm 2.0)\%$  in the CP and CF efficiency samples, respectively. The background estimate in the CP efficiency sample given by isolation extrapolation method is consistent with the background estimate using SVX-PEM tracking technique. This technique is discussed in Section 3.8, and it estimates

the background to be  $(0.5 \pm 0.5)\%$ . Since the backgrounds in the efficiency sample affects the measurement of the efficiency, it consequently affects the cross section measurement. We consider it to be a source of systematic error. Therefore, the relative systematic errors on  $\epsilon_{cp}$  and  $\epsilon_{cf}$  are taken to be 1.0% and 2.0%, respectively.

As stated in Section 3.4.2, the cut efficiencies for plug and forward electrons in the PP and PF sample are measured using the CP and CF efficiency samples, with higher  $E_T$  cuts on the plug and forward legs. The higher  $E_T$  cuts account for the difference in the mean  $E_T$  between the different samples. We estimate that the CP and CF efficiency samples with the higher  $E_T$  cuts are background free. Therefore, the systematic errors from the background in the efficiency sample for the  $\epsilon_{pp}$  and  $\epsilon_{pf}$  are assigned to be 0%.

### 5.3 Systematic error from modeling the $P_T$ distribution of $Z$ bosons

We vary the  $Z$   $P_T$  distribution by changing the  $K_t$  smearing parameter in Pythia. The effect is estimated with a “Toy” Monte Carlo. In the “Toy” Monte Carlo, the event generator is the same as discussed in Section 4. However, the detector simulation is simplified. For example, the cracks in the calorimeters are not simulated, the EM shower energies are simply smeared with a Gaussian energy resolution function, and the Level 2 trigger efficiency is also not included in the simulation. The input value is  $K_t = 2.05 \pm 0.15$ . We vary the  $K_t$  input parameter by  $\pm\sigma$  about the baseline,  $K_t = 2.05$ , to estimate the effect of the  $Z$   $P_T$  distribution on the acceptance. The relative systematic error on the total acceptance is 0.2%. The relative systematic error on  $\epsilon A$  ( $\frac{|\Delta(\epsilon A)|}{\epsilon A}$ ) versus  $y$  is shown in Figure 5.1 as a dotted line.

## 5.4 Systematic error from the choice of PDFs

The theoretical prediction for the differential cross section  $d^2\sigma/dy dP_T$  change depending on the choice of input PDFs. Therefore, the total acceptance and the acceptance in  $y$  bins integrated over  $P_T$  depend on the choice of PDFs.

The “Toy” Monte Carlo program is used to measure the variation in acceptance versus different PDFs. The CTEQ3L PDF is chosen to be the baseline PDF. The systematic error is estimated by using other recent PDFs available through PDFLIB 6.06: CTEQ3M, CTEQ3D, and MRSA'. Note that the calculation of the  $y$  distributions with this input PDFs are done to leading order. Therefore, although next to leading order PDFs such as CTEQ3M and MRSA' should not be used in a leading order calculation, they provide sufficiently different predictions (when used within the leading order calculation), which are useful in estimating a systematic error in the acceptance. We allow a  $\pm\sigma$  smearing of the  $d^2\sigma/dy dP_T$  shape. Therefore, only the PDFs which describe the measured  $y$  distribution within the  $\pm\sigma$  are used. First, the predicted  $y$  distributions for the various PDFs are compared to the data. The  $\chi^2/ndf$  between the data and the CTEQ3L, CTEQ3M, CTEQ3D, and MRSA' PDFs are 4.7/7, 27.7/7, 4.1/7, and 15.0/7, respectively (for simplicity we use only 8 bins in  $y$ ). These  $\chi^2/ndf$  correspond to about 50%, 0%, 50%, and 5% in the confidence level. Based on the  $\chi^2/ndf$ , the PDFs CTEQ3M and MRSA' do not satisfy the  $\pm\sigma$  requirement. Therefore, the systematic error from the choice of PDFs is estimated using the CTEQ3D PDFs only. The systematic uncertainty is taken to be the deviation from the baseline PDFs (CTEQ3L) to the CTEQ3D PDFs. The solid line in Figure 5.1 shows the relative systematic error on  $\epsilon A$  versus  $y$  from the choices of PDFs. Because there are no data above  $|y| = 2.8$ , the systematic error estimate is given only up to  $|y| = 2.8$ . From  $|y| = 1.0$  to 1.7, the acceptance is not affected by changing from CTEQ3L to CTEQ3D PDFs. The

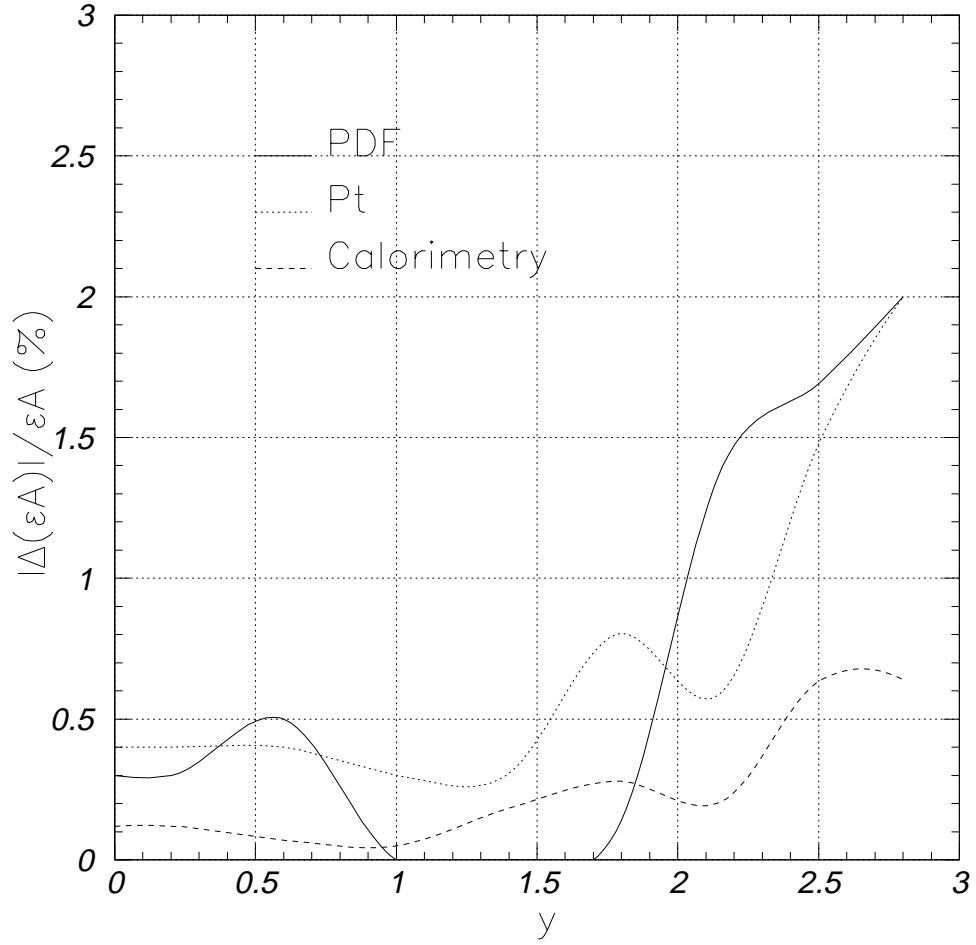


Figure 5.1: The relative systematic error on  $\epsilon A$  ( $\frac{|\Delta(\epsilon A)|}{\epsilon A}$ ) versus  $y$  from difference systematic uncertainty sources. Because there are no data above 2.8, the systematic error estimate is given only up to  $|y| = 2.8$ .

relative systematic error from PDFs on the total  $\epsilon A$  (for the total cross section measurement) is 0.2%.

Region	$c_1$	$c_2$
CEM	0.135	0.017
PEM	0.22	0.037
FEM	0.28	0.105

Table 5.2: The resolution parameters used in the Monte Carlo detector simulation.

## 5.5 Systematic error from the energy resolution of the calorimeter

The calorimeter energy resolution is

$$\frac{\sigma_E}{E} = \frac{c_1}{\sqrt{E}} \oplus c_2$$

where  $c_1$  is the stochastic constant, and  $c_2$  is the constant term which is tuned such that the  $M_{ee}$  distribution of the Monte Carlo simulation events matches the data. The resolution parameters are shown in Table 5.2. The “Toy” Monte Carlo program is used to simulate the effect of the uncertainty in the constant terms on the acceptance. The constant terms in the resolution of the CEM, PEM, and FEM are varied at the same time by  $\pm 20\%$  about the baseline to determine the effects on the acceptance. The relative systematic error on the total acceptance from a  $\pm 20\%$  change in the constant term is 0.1%. The relative systematic error on  $\epsilon A$  versus  $y$  is shown as the dashed line in Figure 5.1.

The combined relative systematic error on the total cross section measurement from all sources is 0.63%.



# Chapter 6

## The Results

Chapter 3 describes the study of backgrounds and efficiencies for the collected sample of  $\gamma^*/Z$  bosons. Chapter 4 describes the acceptance calculation using Monte Carlo event sample. These two chapters give the necessary information for determining the differential cross section,  $d\sigma(\gamma^*/Z)/dy$ . Chapter 5 summarizes the potential sources of systematic errors on the  $d\sigma(\gamma^*/Z)/dy$ . The relation used to calculate the differential cross section values is given in the following sections. Here we present the result and compare our measurement to various theoretical calculations. We also presents the total cross section measurement of  $\gamma^*/Z$  production and compares the measurement to other measurements and theoretical predictions.

### 6.1 The Differential Cross Section, $d\sigma(\gamma^*/Z)/dy$

The differential cross section  $d\sigma(\gamma^*/Z)/dy$  is calculated using

$$\frac{d\sigma_i}{dy_i} = \frac{\sum_j (N^{candidates} - N^{backgrounds})_{ij}}{c_i \Delta y_i \sum_j (\mathcal{L} \epsilon A_i)_j} \quad (6.1)$$

where  $i$  represents  $i$ -th  $y$  bin,  $j$ =Run 1A, Run 1B,  $N^{candidates}$  and  $N^{backgrounds}$  are the number of candidate  $e^+e^-$  pair events and background estimates, respectively,  $\Delta y_i$  is the  $i$ -th  $y$  bin size,  $\mathcal{L}$  is the integrated luminosity, and  $\epsilon$  is the combined efficiency of the  $Z$  vertex, Level 1, Level 3 and offline selection cuts. The quantity  $A_i$  is the acceptance in the  $i$ -th bin. It is calculated using the Monte Carlo sample discussed in Chapter 4. This acceptance includes geometric acceptance, kinematic acceptance, and Level 2 trigger efficiency. The variable  $c_i$  is the bin centering correction. The bin centering correction corrects the average value of  $d\sigma(\gamma^*/Z)/dy$  in the  $y$  bin to the value at the center of the  $y$  bin. It is calculated using the theory  $d\sigma(\gamma^*/Z)/dy$  curve from the next-to-leading-order (NLO) calculation with the CTEQ4M [36] PDFs.

Figure 6.1 shows the acceptance times efficiency,  $\epsilon A$ , as a function of  $Z$  rapidity. It shows that by including the PP and PF events, we extend the measurement of rapidity up to 2.8, with a significant increase in statistics in the  $|y| > 1.2$  region.

The differential cross section  $d\sigma(\gamma^*/Z)/dy$  for the process,  $p\bar{p} \rightarrow ee(\gamma^*/Z) + X$ , measured over the mass range  $66 < M_{\gamma^*/Z} < 116$  GeV/c<sup>2</sup>, is given in Table 6.1. The results for positive and negative rapidity have been averaged because the distribution is expected to be symmetric with respect to  $y=0$ . The first error on  $d\sigma(\gamma^*/Z)/dy$  is the statistical error, and the second error is the systematic error. The systematic error listed does not include the error from the integrated luminosity, which is discussed in Chapter 5.

The differential cross sections in Table 6.1 are also compared to various theory calculations. The calculations performed in this analysis are:

- LO(CTEQ3L): leading-order (LO) calculation with CTEQ3L [30] PDFs.  $\sigma(\gamma^*/Z)=162.2$  pb.
- LO(CTEQ4L): LO calculation with CTEQ4L [36] PDFs.  $\sigma(\gamma^*/Z)=165.6$  pb.

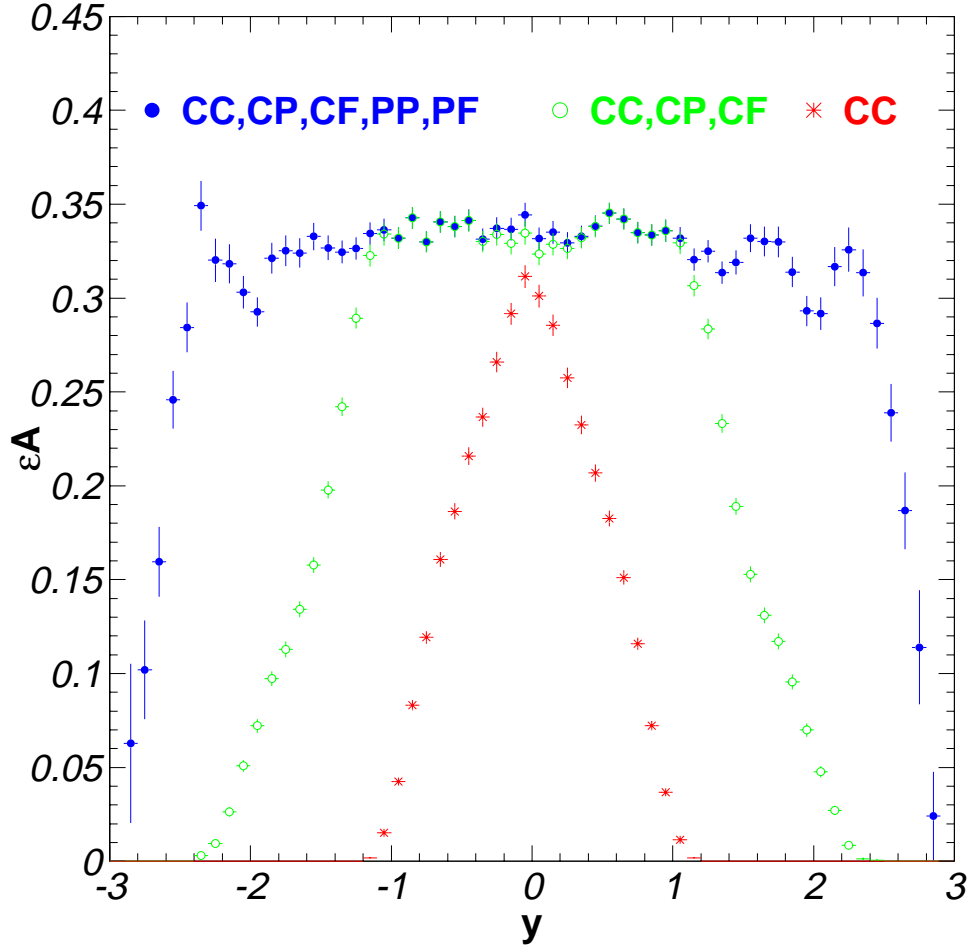


Figure 6.1: Acceptance times efficiency as a function of dilepton rapidity for the various categories of  $e^+e^-$  pairs. By including PP and PF events, the measurement is extended in rapidity up to  $y$  of 2.8, with a significant increase in statistics in the  $|y| > 1.2$  region.

$y$	C	$d\sigma/dy$ (pb)
0.05	1.000	$70.78 \pm 3.27 \pm 0.37$
0.15	1.000	$70.19 \pm 3.26 \pm 0.37$
0.25	1.000	$72.03 \pm 3.30 \pm 0.41$
0.35	1.000	$72.18 \pm 3.30 \pm 0.45$
0.45	1.000	$69.90 \pm 3.20 \pm 0.50$
0.55	1.000	$72.86 \pm 3.25 \pm 0.59$
0.65	1.000	$73.68 \pm 3.27 \pm 0.64$
0.75	1.000	$64.64 \pm 3.09 \pm 0.58$
0.85	1.000	$66.59 \pm 3.13 \pm 0.63$
0.95	1.000	$64.59 \pm 3.10 \pm 0.67$
1.05	1.000	$64.04 \pm 3.09 \pm 0.70$
1.15	1.000	$63.11 \pm 3.10 \pm 0.67$
1.25	0.999	$56.26 \pm 2.92 \pm 0.55$
1.35	1.000	$51.57 \pm 2.82 \pm 0.45$
1.45	0.999	$51.56 \pm 2.82 \pm 0.45$
1.55	1.000	$43.51 \pm 2.56 \pm 0.39$
1.65	0.999	$41.62 \pm 2.54 \pm 0.45$
1.75	1.000	$41.24 \pm 2.53 \pm 0.46$
1.85	0.999	$35.15 \pm 2.35 \pm 0.40$
1.95	1.000	$29.72 \pm 2.23 \pm 0.36$
2.05	1.000	$23.80 \pm 1.98 \pm 0.33$
2.15	1.000	$18.04 \pm 1.68 \pm 0.29$
2.25	1.002	$18.47 \pm 1.70 \pm 0.33$
2.35	1.003	$9.35 \pm 1.17 \pm 0.19$
2.45	1.006	$8.20 \pm 1.17 \pm 0.19$
2.55	1.010	$3.24 \pm 0.80 \pm 0.08$
2.65	1.023	$2.15 \pm 0.85 \pm 0.06$
2.75	1.043	$2.14 \pm 1.02 \pm 0.06$
2.85	1.104	$0.00 \pm 0.00 \pm 0.00$
2.95	1.067	$0.00 \pm 0.00 \pm 0.00$

Table 6.1:  $d\sigma/dy$  distribution of  $e^+e^-$  pairs in the mass range  $66 < M_{ee} < 116$  GeV/ $c^2$ . The  $y$  is the bin center value. C is the bin centering correction.  $d\sigma/dy$  is the differential cross section from the Run 1A and Run 1B data. The first error on  $d\sigma/dy$  is statistical error, and the second is the systematic error except for the 3.9% integrated luminosity error.

- LO(CTEQ5L): LO calculation with CTEQ5L [35] PDFs.  $\sigma(\gamma^*/Z)=167.0$  pb.
- NLO(CTEQ4M): NLO calculation with CTEQ4M [36] PDFs.  $\sigma(\gamma^*/Z)=225.5$  pb.
- NLO(CTEQ4M-d): NLO calculation with  $d$  quark enhanced modified CTEQ4M PDFs [37]. The CTEQ4M PDFs with the enhanced  $d$  quark distribution is in better agreement with the CDF  $W$  asymmetry [38] data than the CTEQ4M PDFs.  $\sigma(\gamma^*/Z)=228.8$  pb.
- VBP(CTEQ4M): gluon resummation calculation [39] with CTEQ4M PDFs.  $\sigma(\gamma^*/Z)=231$  pb.
- NLO(CTEQ5M-1): NLO calculation with CTEQ5M-1 PDFs [35, 40]. This PDF is in better agreement with the CDF  $W$  asymmetry data [38] than the CTEQ4M PDF. In addition, CTEQ5M-1 is the latest version of the CTEQ5M PDF which has the correct QCD evolution and agrees with MRST99 [41, 40]) PDFs.  $\sigma(\gamma^*/Z)=222.7$  pb.
- NLO(MRST99): NLO calculation with MRST99 PDFs. It is in agreement with the NLO(CTEQ5M-1).  $\sigma(\gamma^*/Z)=222.0$  pb.
- NLO(MRST99 $\uparrow$ ): NLO calculation with MRST99 PDFs with higher (+2.3% with respect to MRST99) quark distribution corresponding to one sigma up in quark normalization.  $\sigma(\gamma^*/Z)=227.2$  pb.
- NLO(MRST99 $\downarrow$ ): NLO calculation with MRST99 PDFs with lower (-1.8% with respect to MRST99) quark distribution corresponding to one sigma down in quark normalization.  $\sigma(\gamma^*/Z)=216.6$  pb.

To compare the theory predications for the  $y$  distribution with the data, the total cross section from the theory calculations are normalized to the total cross

section from the measurement. Figures 6.2 and 6.3 compare the data with various theoretical calculations. The solid dots are the data, and the curves represent theoretical calculations.

The  $\chi^2/ndf$  between the data and various calculations are 21.2/27 (LO(CTEQ3L)), 29.1/27 (LO(CTEQ4L)), 33.3/27 (LO(CTEQ5L)), 23.5/27 (NLO(CTEQ4M)), 24.0/27 (NLO(CTEQ5M)), 24.3/27 (NLO(CTEQ5M-1)), 23.1/27 (NLO(MRST99)), 23.6/27 (VBP(CTEQ4M)), 21.3/27 (NLO(CTEQ4M-d)), 22.3/27 (NLO(MRST99 $\uparrow$ )), and 23.7/27 (NLO(MRST99 $\downarrow$ )). The uncertainty used in the  $\chi^2$  calculation include statistic error only. Among the various calculations performed in this analysis, the LO calculation using the recent PDFs LO CTEQ4L and CTEQ5L PDF do not describe the data as well as the predictions using the NLO calculations with the recent NLO PDFs. This can be seen clearly in Figure 6.4 which gives the ratio of data over theory as a function of  $y$  for various calculations.

## 6.2 The Total Cross Section of $\gamma^*/Z$ Production

A numerical integration over the  $y$  bins gives a model independent measurement of the total cross section for the  $e^+e^-$  pairs. Because there are no data for  $|y| > 2.8$ , we use a NLO calculation with the CTEQ5M-1 PDFs to calculate  $\gamma^*/Z$  production in the region of  $|y| > 2.8$ . the cross section in this region is about 0.02% of the predicated total cross section. The extracted model independent measurement of the total cross section is

$$\sigma(\gamma^*/Z) = \sum_i c_i \times \frac{d\sigma_i}{dy_i} \times dy_i = 252.1 \pm 3.4(stat.) \pm 1.6(syst.) \pm 9.9(lum.syst.) \text{ pb.}$$

The  $\frac{d\sigma_i}{dy_i}$  values are multiplied by  $c_i$  to remove the bin centering correction in order to do the integration.

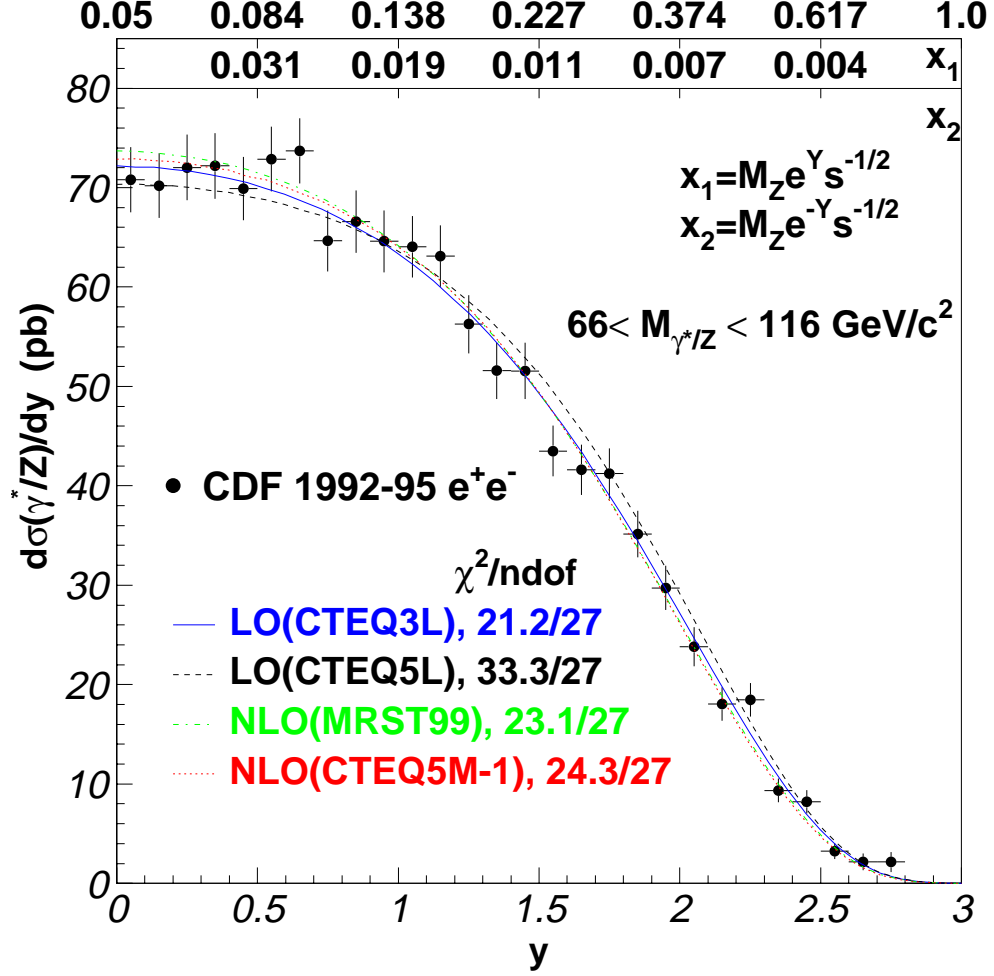


Figure 6.2:  $d\sigma(\gamma^*/Z)/dy$  distribution of  $e^+e^-$  pairs in the mass range  $66 < M_{ee} < 116 \text{ GeV}/c^2$ . The dots are Run 1A and 1B combined data and the curves are the LO(CTEQ3L), LO(CTEQ5L), NLO(MRST99) and NLO(CTEQ5M-1) calculations, respectively. The total cross section of the theory curves are normalized to the data. They are scaled up to compare to the data by factors of 1.55, 1.51, 1.14, and 1.13 for LO(CTEQ3L), LO(CTEQ5L), NLO(MRST99), and NLO(CTEQ5M-1), respectively.

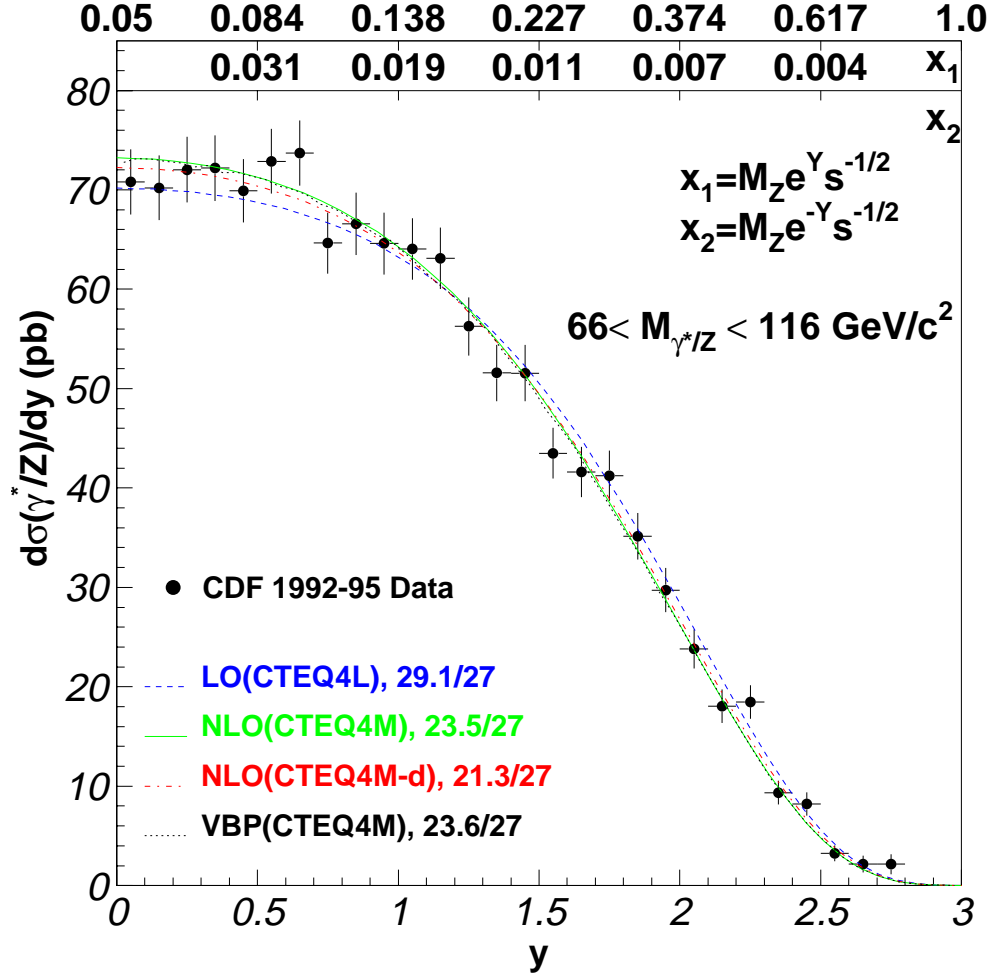


Figure 6.3:  $d\sigma(\gamma^*/Z)/dy$  distribution of  $e^+e^-$  pairs in the mass range  $66 < M_{ee} < 116 \text{ GeV}/c^2$ . The dots are Run 1A and 1B combined data and the curves are the NLO(CTEQ4M), VBP(CTEQ4M), and NLO(CTEQ4M-d) calculations, respectively. The total cross section of the theory curves are normalized to the data. They are scaled up to compare to the data by factors of 1.12, 1.09, and 1.10 for NLO(CTEQ4M), VBP(CTEQ4M), and NLO(CTEQ4M-d), respectively



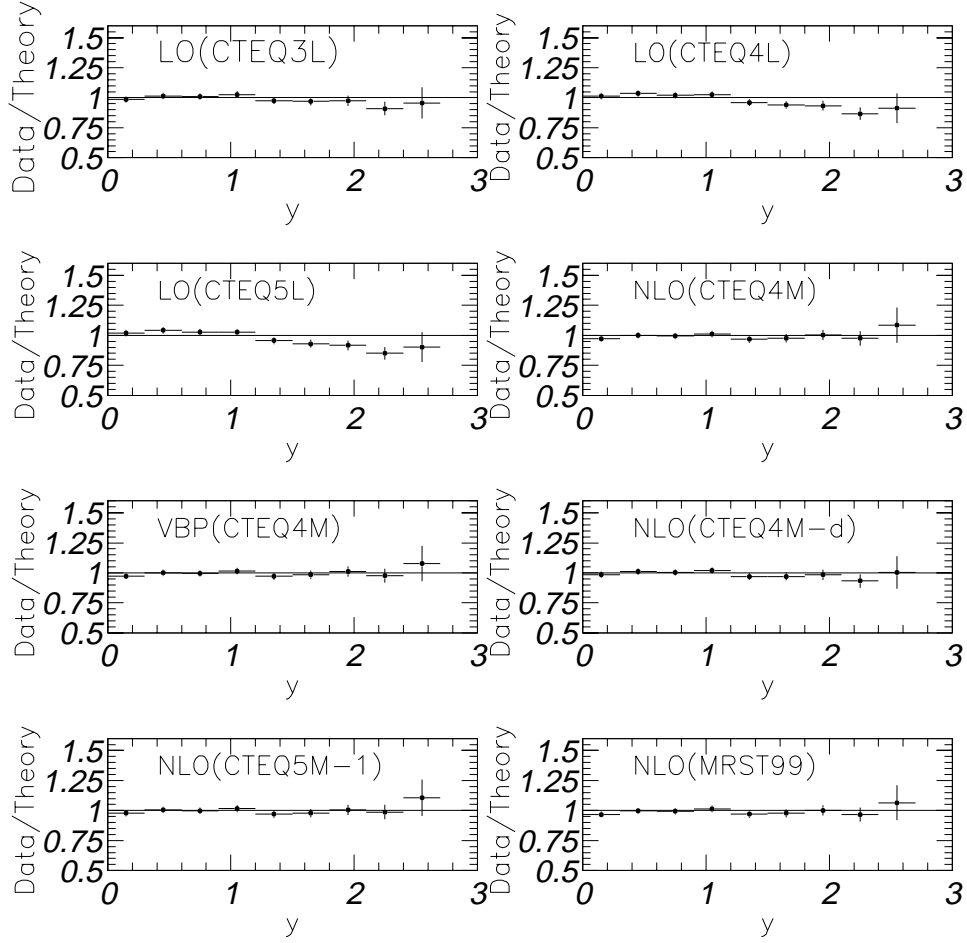


Figure 6.4: Data/Theory of  $d\sigma(\gamma^*/Z)/dy$  of  $e^+e^-$  pairs in the mass range  $66 < M_{ee} < 116 \text{ GeV}/c^2$ . The data are Run 1A and 1B combined. The total cross section of the calculations for LO(CTEQ3L), LO(CTEQ4L), LO(CTEQ5L), NLO(CTEQ4M), VBP(CTEQ4M), NLO(CTEQ4M-d), NLO(CTEQ5M-1), and NLO(MRST99) are scaled up to compare to the data by factors of 1.55, 1.52, 1.51, 1.12, 1.09, 1.10, 1.13, and 1.14, respectively.

The corresponding  $\sigma(p\bar{p} \rightarrow Z) \cdot Br(Z \rightarrow ee)$  of  $\sigma(\gamma^*/Z)$  is  $253 \pm 4(\text{stat.} + \text{syst.}) \pm 10(\text{lum})$  pb. This is in agreement with other analysis of the CDF production data in the dielectron [21] ( $248 \pm 5(\text{stat.} + \text{syst.}) \pm 10(\text{lum.})$  pb, using only the CC+CP+CF  $e^+e^-$  sample), and dimuon [13] ( $237 \pm 9(\text{stat.} + \text{syst.}) \pm 9(\text{lum.})$  pb using a CC sample) channels. These previous measurements use a QCD model to correct for the missing events at high rapidity.

As we discussed in Section 3.4.4, there are three measurements of total inelastic cross section (CDF, E710, and E811). CDF uses it's own measurement. However, DØ uses the average of three measurements. This results in a 5.9% [42] difference in the luminosity conversion between CDF and DØ. The recent DØ measurement of  $\sigma(p\bar{p} \rightarrow Z) \cdot Br(Z \rightarrow ee)$  is  $221 \pm 11$  pb [43]. This result, when increased by 5.9% to account for the difference in the CDF and DØ luminosity calculations, is  $234 \pm 12$  pb. It is consistent with our measurement of  $253 \pm 4(\text{stat.} + \text{syst.}) \pm 10(\text{lum})$  pb.

The total cross section measurement can also be compared to QCD calculations. Table 6.2 summarizes the results from various theoretical predictions for the production of  $e^+e^-$  pairs in the mass range of 66-116 GeV/ $c^2$ . In Table 6.2, NNLO(MRST99) represents next-to-next-leading-order (NNLO) [44] calculation with MRST99 PDFs. It is calculated by MRST group and the details can be found in reference [40]. NNLO(MRST<sub>NNLO</sub>) represents NNLO calculation with MRST<sub>NNLO</sub> PDFs set. The MRST<sub>NNLO</sub> is a NNLO PDF set. It is a result of NNLO global fits to the experimental data. the detail discussion of the analysis can be found in reference [45].

The LO calculation using the CTEQ3L, CTEQ4L, and CTEQ5L PDFs yield cross sections of 162.2 pb, 165.6 pb, and 225.5 pb, while the NLO calculation using the CTEQ4M and CTEQ5M-1 give 225.5 pb and 222.7 pb. This indicates that the NLO corrections to the total cross section are significant. In Chapter 4,

	$\sigma(\gamma^*/Z)$ pb
LO(CTEQ3L)	162.2
LO(CTEQ4L)	165.6
LO(CTEQ5L)	167.0
NLO(CTEQ4M)	225.5
NLO(CTEQ4M-d)	228.8
VBP(CTEQ4M)	230.9
NLO(CTEQ5M-1)	222.7
NLO(MRST99)	222.0
NLO(MRST99 $\uparrow$ )	227.2
NLO(MRST99 $\downarrow$ )	216.6
NNLO(MRST99)	227
NNLO(MRST <sub>NNLO</sub> )	230

Table 6.2: Various theoretical calculations of the total cross section for  $66 < M_{\gamma^*/Z} < 116$  GeV/ $c^2$ . The measurement using CDF Run 1 data is 252.1 pb. Note that except for the CTEQ5M-1, MRST99 and MRST99 $\uparrow$ , MRST99 $\downarrow$ , and MRST<sub>NNLO</sub>, the other PDFs have some mistakes in the QCD evolution to the  $Z$  mass.

we introduce the K-factor which can be used as a NLO-to-LO correction. The NLO-to-LO K-factor is about 1.4. In contrast, the NLO total cross section is lower than NNLO prediction by only 2.3%, given the results from NLO(MRST99) and NNLO(MRST99). Fixed order QCD calculations have uncertainties from PDF measurements. The NNLO prediction with the latest MRST99 PDFs is  $227 \pm 9$  pb, where the 4% error is mostly from uncertainties in the NLO PDFs [40]. Although a full set of NNLO PDFs is not available, recent estimates [46, 45] of NNLO PDFs indicate that the NNLO PDFs will increase the theoretical cross sections by 1–4%. The recent estimate of the NNLO calculation of cross section using NNLO MRST PDFs set gives a theoretical prediction of  $230 \pm 9$  [45] (see Table 6.2). Given these uncertainties, the theoretical expectation is consistent with our measurement.

## Chapter 7

# The Conclusions

The rapidity distributions of  $e^+e^-$  pairs in the  $Z$  boson mass region have been measured for the first time over nearly the entire kinematic region at a center of mass energy 1.8 TeV. This measurement uses a new tracking technique in the high rapidity region to reduce the background and associated uncertainties. In addition, unlike the previous measurement of the total cross section, this measurement is model independent. The comparison between our measurement and the theoretical calculations of the rapidity distributions indicates that LO calculation using recent LO PDFs does not fit the shape as well as the NLO calculation with the most recent NLO PDFs. With the increased statistics of Run II and newly upgraded tracking devices and endplug calorimeters, the measurement of the  $Z$  rapidity distribution could make a significant contribution in improving our knowledge of PDFs.

# Bibliography

- [1] J. J. Thomson, Phil. Mag. **44** 269 (1897).
- [2] S. L. Glashow, Nucl. Phys. **22**, 579 (1961).
- [3] S. Weinberg, Phys. Rev. Lett. **19**, 1264 (1967).
- [4] A. Salam, in proc. of the 8th Nobel Symposium, edited by N. Svartholm, Almqvist, and Wiksell, Stockholm (1968).
- [5] P. W. Higgs, Phys. Rev. Lett. **13** 508 (1964).
- [6] J. I. Breidenbach *et al.*, Phys. Rev. Lett. **23** 935 (1969). E. D. Bloom *et al.*, Phys. Rev. Lett. **23** 930 (1969).
- [7] V.N. Gribov, L.N. Lipatov, Sov. J. Nucl. Phys. **15** 438 (1972). G. Altarelli, G. Parisi, Nucl. Phys. B**126** 298 (1977). Yu. Dokshitzer, Sov. Phys. JETP **46** 641 (1977).
- [8] S.D. Drell and T.-M. Yan, Phys. Rev. Lett. **25**, 316 (1970).
- [9] G. Altarelli, R. E. Ellis, and G. Martinelli, Nucl. Phys. B**157**, 461 (1979).
- [10] J. Kubar, M. le Bellac, J.L. Meunier and G. Plaut, Nucl. Phys. B**175**, 251 (1980).

- [11] P. Aurenche and P. Chiappetta, Z. Phys. **C34**, 201 (1987).
- [12] P.J. Sutton, A.D.Martin, R.G. Roberts, W.J. Stirling, Phys. Rev. **D45**, 2349 (1992).
- [13] F. Abe *et al.*, “Measurement of  $Z^0$  and Drell-Yan Production cross sections using dimuons in  $\bar{p}p$  collisions at  $\sqrt{s} = 1.8$  TeV”, Phys. Rev. D **59**, 052002 (1999).
- [14] F. Abe *et al.*, Nucl. Instrum. Methods Phys. Res. Sect. **A271**, 387 (1988).
- [15] F. Abe *et al.*, Phys. Rev. Lett. **76**, 3070 (1996).
- [16] G.W. Foster *et al.*, Nucl. Instrum. Methods Phys. Res. Sect. A **269**, 93 (1988).
- [17] Larry Nodulman, ”*A Further Tweak to CEM Response for Incidence Angle*”, CDF note 3896, Sep. 1996.
- [18] Young-Kee Kim, ”*PEM Energy Scale Corrections for Run 1B*”, CDF note 3424, Dec. 1995.
- [19] Qun Fan, ”*Run 1B PEM Energy Correction for the W Asymmetry Analysis*”, CDF note 4396, Nov. 1997.
- [20] Qun Fan, Arie Bodek, ”*A Stand-alone SVX Track-Finding Routine For High Pt Tracks Originating From The Beam Position*”, CDF note 3585, Mar. 1996; Also UR-1485. It is published in Proceedings of VIth International Conference on Calorimetry in High Energy Physics, June 8-14, 1996, Frascati (Rome), Italy. Page 553. (FERMILAB-CONF-96/411-E)
- [21] W.K. Sakumoto *et al.*, ”*The  $P_t$  Cross Section of Massive  $e^+e^-$  Pairs in the Z boson Region from  $p\bar{p}$  Collisions at  $\sqrt{s} = 1.8$  TeV using Run 1A and 1B data*”, CDF note 4561, 26 Apr. 1998. Phys. Rev. Lett. **84**, 845 (2000).

- [22] K. Byrum, A.B. Wicklund, “*The Level-2 Trigger Efficiency for 9 GeV Electrons in Run 1A.*”, CDF note 3120, Apr. 1995; “*The Level-2 Trigger Efficiency for 9 GeV Electrons in Run 1A, Part II*”, CDF note 3665, Apr. 1996.
- [23] W. Badgett, P. Derwent, “*Event Z Vertex Efficiency as a Luminosity Correction for Run 1A*”. CDF note 2703, July, 1994.
- [24] A. Beretvas *et al*, “*Event Z Vertex Efficiency as a Luminosity Correction for Run 1B*”. CDF note 5066, Aug. 1999.
- [25] N. Amos *et al.*, Phys. Rev. Lett. **68**, 2433 (1992).
- [26] C. Avila *et al.*, Phys. Lett. B **445**, 419 (1999).
- [27] M. Albrow *et al.*, “*Comparison of the Total Cross Sections Measurements of CDF and E811*”, FERMILAB-TM-2071.
- [28] T. Sjöstrand, Comput. Phys. Commun. **82**, 74 (1994).  
<http://www.thep.lu.se/~torbjorn/Pythia.html>.
- [29] M. Shapiro *et al.* “*A User’s Guide to QFL*”, CDF note 1810, 1992.
- [30] H. L. Lai *et al.*, Phys. Rev. D **51**, 4763 (1995).
- [31] W.K.Sakumoto, *et al.*, “*Drell-Yan Radiative Corrections.*”, CDF note 3497, Jan. 1996.
- [32] E. Barberio and Z. Was, Comput. Phys. Commun. **79**, 291 (1994); E. Barberio, B. van Eijk, and Z. Was, *ibid.* **66**, 115 (1991).
- [33] U. Baur, S. Keller, and W. K. Sakumoto, Phys. Rev. D **57**, 199 (1998).
- [34] J.C. Collins and D.E. Soper, Phys. Rev. D **16**, 2219(1997).

- [35] CTEQ5: H. L. Lai *et al.*, Eur.Phys.J. C**12** 375 (2000)
- [36] CTEQ4: H. L. Lai *et al.*, Phys. Rev. D **55**, 1280 (1997)
- [37] U. K. Yang and A. Bodek, Phys. Rev. Lett. **82**, 2467 (1999).
- [38] F. Abe *et al.*, Phys. Rev. Lett. **81**, 5754 (1998).
- [39] R. K. Ellis and S. Veseli, Nucl. Phys. B **511**, 649 (1998); C. Balàzs and C.-P. Yuan, Phys. Rev. D **56**, 5558(1997).
- [40] A. D. Martin, R.G. Roberts, W.J. Stirling, and R.S. Thorne, Eur. Phys. J. C**14**, 133 (2000), or hep-ph/9907231.
- [41] A. D. Martin, R.G. Roberts, W.J. Stirling, and R.S. Thorne, Eur. Phys. J. C **4**, 463 (1998), hep-ph/9803445.
- [42] D. Cronin-Hennessy *et al.*, Nucl. Instrum. Methods Phys. Res., Sect. A **443/1**, 37-50 (2000)
- [43] B. Abbott *et al.*, Phys. Rev. D. **61**, 072001 (2000).
- [44] DIS :W. L. Van Neerven and E. B. Zijlstra, Nucl. Phys. B **382**, 11 (1992).  $\overline{\text{MS}}$ : R. Hamberg, W.L. van Neerven, and T. Matsuura, Nucl. Phys. B **359**, 343 (1991).
- [45] A.D. Martin, R.G. Roberts, W.J. Stirling, and R.S. Thorne, hep-ph/0007099.
- [46] U.K. Yang and A. Bodek, Euro. Phys. Jour. C **13**, 241 (2000); W.L. van Neerven and A. Vogt, Nucl. Phys. B **568**, 263 (2000), hep-ph/9907472.
- [47] J.B. Liu *et al.*, CDF note 4898, June, 2000.
- [48] T. Affolder *et al.*, to be published.



- [49] T. Affolder *et al.*, <http://xxx.lanl.gov>, hep-ex/0006025
- [50] HERWIG 6.1, hep-ph/9912396; G. Marchesini, B.R. Webber, G. Abbiendi, I.G. Knowles, M.H. Seymour and L. Stanco, Computer Phys. Commun. 67 (1992) 465. <http://hepwww.rl.ac.uk/theory/seymour/herwig/>
- [51] CTEQ1: James Botts, *et al.*, Phys. Lett. B**304**, 159 (1993), hep-ph/9303255. CTEQ2 and CTEQ3: H. L. Lai, *et al.*, Phys. Rev. D**51**, 4763(1995), hep-ph/9410404.
- [52] ZEUS collaboration: J. Breitweg, *et al.*, Eur. Phys. J. C**7**, 609 (1999).
- [53] Y.S. Chung *et al.*, CDF note 5207, Mar. 2000.

# Appendix A

## Monte Carlo Programs in Particle Physics

In particle physics, a commonly used method to calculate the observables that can be directly compared to experimental data is to simulate the experiment by means of computers. Since random numbers are used, the simulation programs are called *Monte Carlo* programs. A Monte Carlo program is an important tool for experimental particle physics. It attempts to include all theoretical and phenomenological knowledge in particle physics. The programs generate events of the processes studied in the experiment and pass them through a computer simulation of the detector.

There exist several event generators for the simulation of hadron collisions, such as PYTHIA [28] and HERWIG [50]. PYTHIA is a general purpose generator for  $e^+e^-$ ,  $p\bar{p}$  and  $ep$  interactions, based on a number of physics aspects, such as hard and soft interactions, parton distributions, initial and final state parton showers, multiple interactions, fragmentation and decay. HERWIG is a Monte Carlo package for simulating Hadron Emission Reactions With Interfering Gluons.

The generator used in this analysis is PYTHIA version 6.125. A CDF detector simulation, QFL [29], was used to simulate the detector response.

# Appendix B

## Parton Distribution Functions

As we discussed in Chapter 1, in order to simulate the physics of hadron collisions, it is necessary to know the probability of finding a parton within a hadron which carries a fraction  $x$  of the parton momentum. The functions which give this probability are called Parton Distribution Functions (PDFs).

In the following paragraphs, we give a brief summary of the two collaboration groups who perform regular global fits to world experimental data. We will focus on the recent sets of PDFs from these two groups.

**CTEQ:** It stands for Coordinated Theoretical-Experimental Project on QCD [51].

The name convention for CTEQ distributions is described as follows:

CTEQ $n$ S where

- $n$  : version number (currently  $n = 5$ )
- $S$  : Normally a factorization scheme label:  $= [L\ M\ D]$  for [Lowest Order,  $\overline{MS}$ , DIS] respectively. Sometimes  $S$  denotes some special characteristic of the set.

CTEQ5 [35] is the latest set which was released in 1999. It used the newly

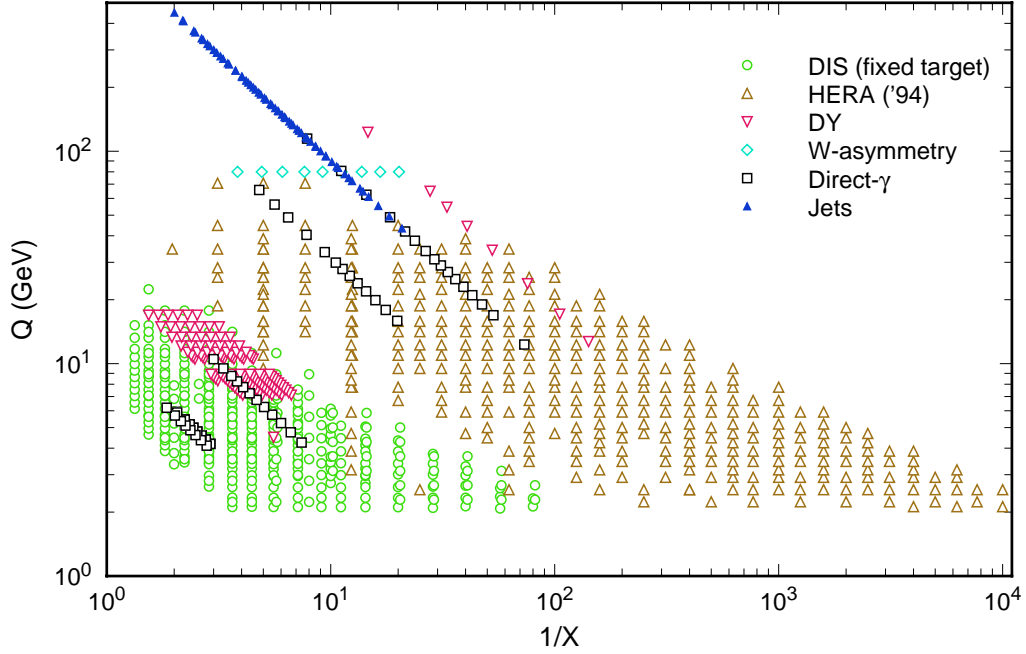


Figure B.1: The kinematic map in the  $(x, Q)$  plane of data points used in the CTEQ5 analysis.

available experimental data. The data from DIS, DY, direct photon and jet processes utilized in the PDFs fits cover a wide range in  $x$  and  $Q$ . The kinematic “map” in the  $(x, Q)$  plane of the data points used in the CTEQ5 analysis is shown in Figure B.1.

Since CTEQ5’s first release, two updated CTEQ5 distribution sets have been added to the table version: CTEQ5M-1/CTEQ5HQ-1 updates CTEQ5M/CTEQ5HQ. The improvement is in the QCD evolution which is now more accurate.

**MRS** (A.D.Martin, R.G.Robers, W.J.Stirling, and R.S. Thorne.) The new global analysis from MRS group results a new set of PDFs, labeled MRST [41]. This set resulted from a NLO analysis in the  $\overline{\text{MS}}$  scheme was released in

1998. A new feature of this analysis is the particular attention to the degree of latitude that relevant parameters can range over while the set can still maintain an acceptable description of all the data. Two degrees of freedom were explored in Ref. [41]:

1. The variation of the average transverse momentum ( $k_T$ ) in prompt photon production, which resulted in a range of gluon distributions at large  $x$ . The corresponding PDFs are MRST(g  $\uparrow$ ), MRST(g  $\downarrow$ ).
2. The variation in the value of  $\alpha_s(M_Z^2)$ . The uncertainties were reflected in alternative sets of PDFs MRST( $\alpha_s$   $\downarrow\downarrow$ ), MRST( $\alpha_s$   $\downarrow$ ), MRST( $\alpha_s$   $\uparrow$ ), MRST( $\alpha_s$   $\uparrow\uparrow$ ). These PDFs correspond to  $\alpha_s(M_Z^2)=0.1125, 0.1150, 0.1200$ , and  $0.1225$  respectively.

MRST is the main PDFs with the nominal  $\alpha_s(M_Z)=0.1175$  and values for the prompt photon data.

Since the release, two small errors were found in the MRST evolution code [40]. The correction of the evolution code plus ZEUS 1999 SVX data [52] data result a new set of PDFs, labeled as MRST99. The  $W$  and  $Z$  Tevatron total cross section predictions using the MRST99 sets are consistent with the predictions given by CTEQ5M-1.

## Appendix C

# Rapidity Distribution in High Mass Region

In this appendix, we discuss the measurement of the dielectron rapidity distribution from  $\gamma^*/Z$  decays in the high mass region, i.e.  $M_{ee} > 116 \text{ GeV}/c^2$ . The data set in this measurement is the same as the one used in the  $Z$  mass region rapidity measurement. The event selection criteria for the two measurements are the same except for differences in a few cuts. In this appendix, we focus on the differences between these two measurement and summarize results at the end.

The differences in the event selection are listed below:

- Mass cut:  $M_{ee} > 116 \text{ GeV}/c^2$
- Isolation cut:  $\text{Ciso4} < 0.1$ . The isolation energy fraction ( $\text{Ciso4}$ ) is used in order to keep the efficiency of the isolation cut uniform in the high mass region.
- Require CF, PP, and PF  $e^+e^-$  pairs to be on the same side of the detector, i.e. west-west or east-east.

	$N^{candidates}$	$N^{background}$	$f_b(\%)$
CC	61	$0.5 \pm 0.3$	$0.8 \pm 0.5$
CP	59	$1.1 \pm 0.6$	$1.9 \pm 1.0$
CF	9	$0.7 \pm 0.3$	$7.8 \pm 3.3$
PP	18	$1.0 \pm 0.7$	$5.6 \pm 3.9$
PF	5	$0.5 \pm 0.5$	$10.0 \pm 10.0$
Total	152	$3.8 \pm 2.4$	$2.5 \pm 1.6$

Table C.1: Number of events passing selection cuts and background estimates.

The number of candidates from Run 1 after the event selection are listed in Table C.1.

The backgrounds are estimated using the same methods discussed in section 3.2. For the CC topology, 0.5 background events are expected in the  $e^+e^-$  channel from the one event in the high mass central  $e\mu$  sample. For the CP, CF, PP, and PF samples, since Ciso4 is used in the event selection, the Ciso4 distribution is used in estimating the background from the isolation extrapolation method. The formula which describes the Ciso4 distribution is chosen to be the same as that for the Eiso4 distribution. The background fractions estimated using the isolation extrapolation method are listed in Table C.1. As discussed in Section 3.2, the SVX-PEM tracking event sample provides an independent method for the background estimates. The background determined using the SVX-PEM tracking is found to be consistent with the estimate from the isolation extrapolation method.

We find that the selection efficiencies in the high mass region are the same as the efficiencies in the  $Z$  mass region (within statistic errors). Therefore, the selection efficiencies measured in the  $Z$  mass region are used to correct the high mass region data.

The acceptance in the high mass region is calculated using the Monte Carlo discussed in Chapter 4. The results are listed in Table C.2.



	Run 1A	Run 1B
A(cc)	0.18239 $\pm$ 0.00517	0.17662 $\pm$ 0.00358
A(cp)	0.23745 $\pm$ 0.00570	0.23631 $\pm$ 0.00399
A(cf)	0.02331 $\pm$ 0.00202	0.02190 $\pm$ 0.00138
A(pp)	0.02798 $\pm$ 0.00221	0.03011 $\pm$ 0.00161
A(pf)	0.00681 $\pm$ 0.00110	0.00680 $\pm$ 0.00077

Table C.2: The acceptances for the CC, CP, CF, PP, and PF  $e^+e^-$  topologies in high mass region. The uncertainties shown here only include the Monte Carlo statistical errors.

$y$	$d\sigma/dy$ (pb)
0.15	1.30 $\pm$ 0.25
0.45	1.32 $\pm$ 0.24
0.75	1.11 $\pm$ 0.22
1.05	1.25 $\pm$ 0.24
1.35	0.74 $\pm$ 0.19
1.65	0.37 $\pm$ 0.13
1.95	0.31 $\pm$ 0.12
2.25	0.07 $\pm$ 0.05
2.55	0.00 $\pm$ 0.00
2.85	0.00 $\pm$ 0.00

Table C.3:  $d\sigma/dy$  distribution of  $e^+e^-$  pairs in the mass range  $M_{ee} > 116$  GeV/ $c^2$ . Here  $y$  is the bin center value, and  $d\sigma/dy$  is the differential cross section from the combined Run 1A and Run 1B data. The errors shown for  $d\sigma/dy$  include statistical errors only.

The differential cross section  $d\sigma(\gamma^*/Z)/dy$  in the high mass region is calculated using Equation 6.1. Table C.3 gives the measurement result. Figure C.1 compares the measured  $d\sigma/dy$ 's to theoretical predictions in the high mass region. The predictions are normalized to the data using the normalization factors from the  $Z$  mass region, i.e. 1.51, 1.14, and 1.13 for the LO(CTEQ5L), NLO(MRST99), and NLO(CTEQ5M-1) calculations, respectively.

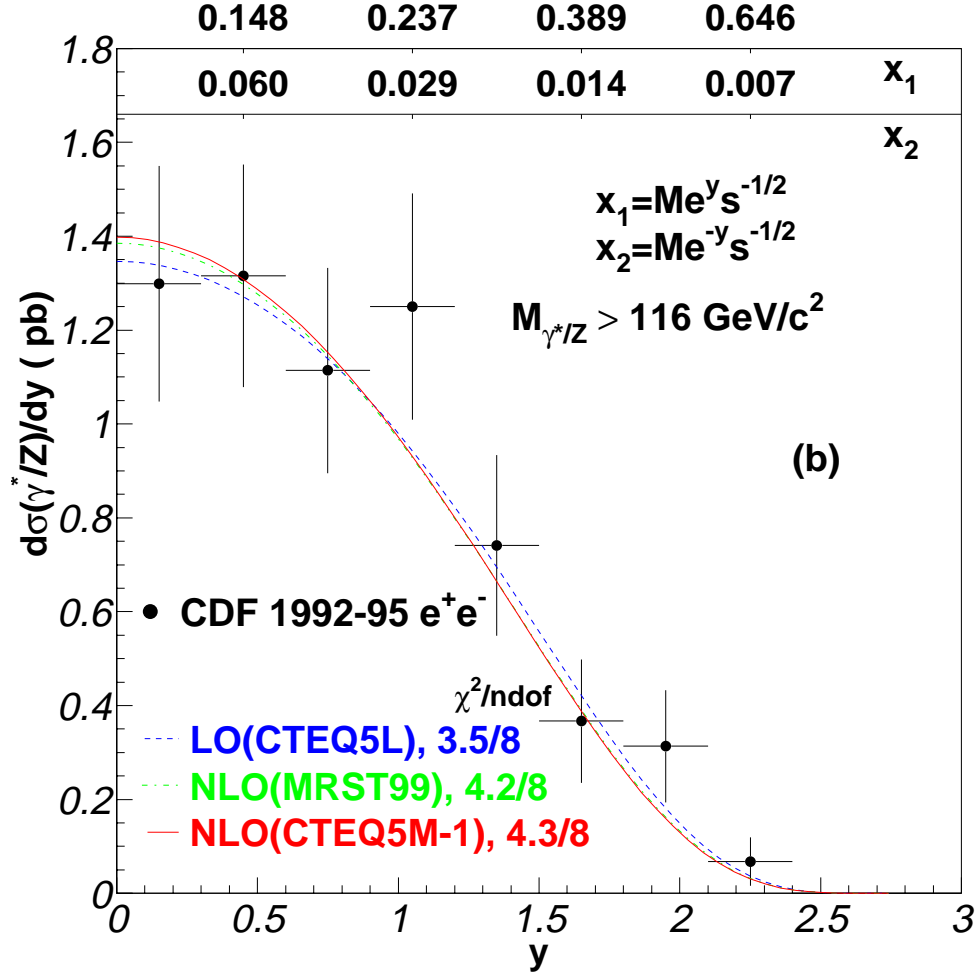


Figure C.1:  $d\sigma(\gamma^*/Z)/dy$  distribution of  $e^+e^-$  pairs in the mass range  $M_{ee} > 116 \text{ GeV}/c^2$ . The dots are the combined Run 1A and 1B data. The curves are the leading order and next to leading order theoretical predictions using LO(CTEQ5L), NLO(MRST99) and NLO(CTEQ5M-1) PDFs, respectively. The predictions are normalized to the data using the normalization factors from the  $Z$  mass region, i.e. 1.51, 1.14, and 1.13 for LO(CTEQ5L), NLO(MRST99), and NLO(CTEQ5M-1) calculations, respectively.

A model independent measurement of the total production cross section for  $e^+e^-$  pairs by integrating the measured values of  $d\sigma/dy$  gives

$$\sigma(\gamma^*/Z) = 4.0 \pm 0.4 \text{ (stat. + syst.)} \pm 0.2 \text{ (lum.) pb}$$

in the high mass region. The corresponding prediction of the total cross section from the NNLO QCD theory using MRST99 NLO PDFs is 3.3 pb.

A detailed discussion of the measurement at high mass can be found in CDF note 5207 [53].